Università degli studi di Parma

Dottorato di ricerca in scienza e tecnologia dei materiali innovativi

XXV Ciclo

Magnetocaloric effect across first order transformations of energy conversion materials

Coordinatore:
Prof. Enrico Dalcanale

Tutor:
Prof. Massimo Solzi

Correlatore:
Dott. Simone Fabbrici

Dottorando: Giacomo Porcari

Contents

CHAPTER 1

Aim

The Magnetocaloric Effect (MCE) is a phenomenon typical of all the magnetic materials: in these systems the action of an applied magnetic field implies, under adiabatic or isothermal conditions, a variation of their temperature or of their entropy. The relation between these two quantities is ruled by the specific heat, which approaching phase transitions shows a sensible magnetic field dependence. The MCE was discovered by Warburg on pure iron in 1881,[1] and it is mainly known as the effect that firstly allowed to reach temperatures lower than 1K by means of adiabatic demagnetization of paramagnetic salts.[2, 3] The MCE is the consequence of the coupling of the spin moments with the external applied magnetic field. In systems with localized magnetism, the electronic, lattice and magnetic contributions to the total entropy can well be distinguished and it can be considered that only the magnetic term is affected by the applied external field. In itinerant electron magnets the magnetic field dependence of the effect is more difficult to describe. The magnetic field induced temperature variations are well detectable just across the critical points of the magnetic phase transitions. For example across the Curie transition the action of the magnetic field favors the ferromagnetic interaction of the low temperature phase: in this way it is induced a deep change of the free energy of the system that implies high entropy and

temperature variations (typical example is pure Gadolinium). First order magnetic transformations often involve magneto-structural or magneto-elastic effects. It has been noted that the concurrent loss of the magnetic ordering together with the occurrence of one of these phenomena can lead to a giant magnetocaloric effect (GMCE - as reported in Gd-Si-Ge alloys) higher than the classical one typical of the second order Curie transitions. Systems showing first order magnetic processes can show direct MCE if they warm on increasing the external field (as observed across the Curie transition) or they can be characterized by inverse MCE if their temperature increases when the external magnetic field is removed. This behavior depends whether the external field favors the low or the high temperature magnetic phase. The presence of latent heat and hysteresis are two typical aspects of first order transformations.

The aim of this thesis is the study of the thermal features of first order magneto-structural transformations temperature and magnetic field dependent. The investigated systems are *Ni-Mn-Ga*-based Heusler alloys. The interest around this material is justified by the presence of its characteristic martensitic transformation, whose magneto-thermal properties can be suitably "tuned" depending on composition and since it is rare earth free. In particular materials showing inverse MCE due to the substitution of some fraction of Nickel with Cobalt are analyzed in this work. It has been shown that these alloys are marked by high magnetization differences between martensite and austenite, which are the two phases involved by the martensitic magneto-structural transformation. Such feature generally contributes to enhance the MCE peculiar of the critical process. A deep experimental study of such transformations is fundamental to understand the real applicative potential of these materials. Three different approaches which characterize the system magneto-thermal behavior are compared.

Magnetometry is used to build the magnetic phase diagram from which the isothermal entropy change can be deduced.

Adiabatic magnetic calorimetry has been carried out to directly measure the material temperature variation.

A Differential Scanning Calorimeter in magnetic field has also been realized to measure the transformation latent heat and the specific heat discontinuity. This setup allows to construct the entropy phase diagram as a function of temperature and magnetic field, thus giving an estimation of the variation both of material

entropy and temperature induced by the magnetic field.

This cross characterization offers multiple perspectives. The measurement of the same sample with the three techniques helps to uncover possible intrinsic inaccuracies, due to the presence of irreversible effects, while characterizing first order processes. The different sensibility of the setups allows to measure samples of different mass and thus compare their magneto-thermal properties.

Moreover a new experimental setup has been realized to study the MCE of the material while it is stressed by magnetization and demagnetization cycles in nearly operative conditions. It is expected that fatigue effects on the structure induced by magnetic field should behave differently depending on the solid solid martensitic transformation properties. This experimental setup would help to investigate such behavior and could encourage the development of innovative energy conversion systems.

CHAPTER 2

Introduction

2.1 Thermodynamics of magnetic materials

2.1.1 Basic phenomenology

The perturbation of the state of a material induced by the application of a magnetic field is the Magnetocaloric Effect (MCE). This phenomenon is intrinsic of all magnetic materials. In these systems the action of a magnetic field implies, under adiabatic or isothermal conditions, a variation of temperature (ΔT_{ad}) or of entropy (Δs_T).

The effect of an applied magnetic field on the thermal properties of a material can be easily deduced from figure 2.1. The example shown represents the behavior of the relative entropy of Gadolinium across its Curie transition ($T_c \sim 292$K) as function of temperature at two different magnetic fields ($H_i < H_f$). The effect of a variable magnetic field on the system is clear in isoentropic conditions:

$$\Delta T_{ad}(T, \mu_0(H_f - H_i)) = T(S, \mu_0 H_f) - T(S, \mu_0 H_i) \tag{2.1}$$

where $T(S, \mu_0 H_i)$ is the initial temperature of the system in the $\mu_0 H_i$ field and S is its entropy value which is constant. Isothermally the MCE becomes:

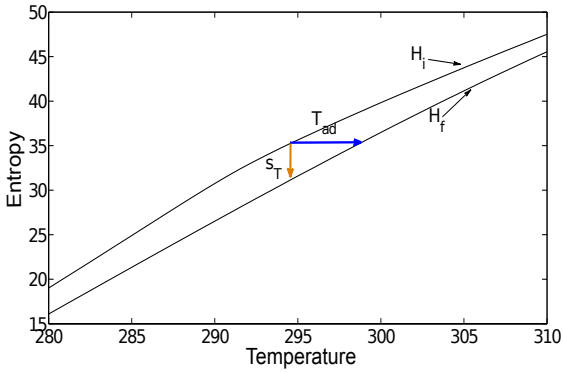

Figure 2.1: Example of s-T entropy diagram at two different applied fields: $H_i < H_f$

$$\Delta S_T(T, \mu_0(H_f - H_i)) = S(T, \mu_0 H_f) - S(T, \mu_0 H_i) \tag{2.2}$$

$S(T, \mu_0 H_i)$ is the initial entropy of the system in the $\mu_0 H_i$ field and T is the isotherm temperature. The example shown in Fig. 2.1 represents the ordinary situation where the magnetic field (at T constant) acts to saturate the magnetic structure lowering the material entropy. The same effect in adiabatic conditions induces a rise of the temperature: as it will be discussed in the following these two manifestations of the same phenomenon represent the "direct MCE".

To better understand how these quantities are linked a review of the thermodynamic potentials is needed.

The first law of thermodynamics shows how heat (δQ) and external work (dW) contribute to modify the system internal energy (dU). The internal energy defined as function of the extensive system parameters (P_j) is:

$$dU(S, P_j) = \delta Q + dW = TdS + \sum_j P_j dX_j = TdS - pdV - \mu_0 HdM \tag{2.3}$$

where Q is positive when flows from the system to the ambient, while the external work is negative if it is made on the system. This expression is restricted to the magnetic (-$\mu_0 HdM$) and mechanical (-pdV) contributions to the total work

while other terms are left out: for example the chemical work (-μdN), the electric work (-EdP), the one linked with the surface energy (-γdS),... The Legendre transformations allow to build up complementary relations for the description of the system energy. The strength of these representations lies in the possibility to express the same system state using, for every equation, different independent variables. The transformation of U that replaces the entropy by the temperature as independent variable leads to the Helmholtz potential F. Here below are reported the thermodynamic potentials in their differential form.

$$dF(T, P_j) = dU - d(ST) = -SdT + \sum_j P_j dX_j = -SdT - pdV - \mu_0 H dM \quad (2.4)$$

Considering a system in thermal contact with a thermostat (T=constant) F represents the work delivered in a reversible process. Enthalpy (E) is deduced replacing the volume dependency of U by the pressure. This potential represents the heat exchanged by the system when all the external fields (p, H, E, ...) are kept constant.

$$dE(S, X_j) = dU - \sum_j d(P_j X_j) = TdS + Vdp + M\mu_0 dH \quad (2.5)$$

The Gibbs free energy is obtained replacing both the X_j and S dependence of U with P_j and T.

$$dG(T, X_j) = dU - SdT - \sum_j d(P_j X_j) = -SdT + Vdp + M\mu_0 dH \quad (2.6)$$

The latter equation is conveniently exploited when are analyzed isobaric and isothermal transformations.[4] The system internal parameters can then be determined from these equations in proper external conditions.

Through the thermodynamic potentials it is possible to understand how the variables that describe our system (S, T, M, B, V, p) are in relation. Using the Gibbs free energy the Maxwell relations describe how locally behaves the system phase diagram in equilibrium conditions (dG=0).

These relations describe the interplay between the different parameters:[4, 5]

$$\frac{1}{\mu_0}\Big(\frac{\partial S}{\partial H}\Big)_{p,T} = \Big(\frac{\partial M}{\partial T}\Big)_{p,H} \tag{2.7}$$

$$\Big(\frac{\partial S}{\partial p}\Big)_{H,T} = -\Big(\frac{\partial V}{\partial T}\Big)_{p,H} \tag{2.8}$$

$$\Big(\frac{\partial S}{\partial M}\Big)_{p,T} = -\mu_0\Big(\frac{\partial H}{\partial T}\Big)_{p,M} \tag{2.9}$$

Among these the most important relation is equation 2.7. In isobaric and isothermal conditions the integral form of eq. 2.7 returns the expression that correlates the magnetization behavior temperature and magnetic field dependent to entropy changes, thus allowing to deduce from magnetometry an estimation of the magnetocaloric effect.

$$\Delta S_T(T,H) = \mu_0 \int_{H_i}^{H_f} \left(\frac{dM}{dT}\right)_H dH \tag{2.10}$$

The expression of the adiabatic temperature change can be obtained starting from the total differential form of entropy:

$$dS = \left(\frac{\partial S}{\partial T}\right)_{H,p} dT + \left(\frac{\partial S}{\partial H}\right)_{H,p} dH + \left(\frac{\partial S}{\partial p}\right)_{H,p} dp \tag{2.11}$$

From the definition of heat capacity and thermal expansion coefficient:

$$C_p = \left(\frac{\delta Q}{dT}\right)_p = T\left(\frac{dS}{dT}\right)_p, \qquad \alpha_T = -\frac{1}{V}\left(\frac{dS}{dp}\right)_T \tag{2.12}$$

Equation 2.11 can then be expressed in adiabatic conditions (dS=0):

$$\left(\frac{C_p}{T}\right)_{H,p} dT + \left(\frac{\partial M}{\partial T}\right)_{H,p} \mu_0 dH - \alpha_T V dp = 0 \tag{2.13}$$

For isobaric processes the last term vanishes giving the simpler form of the adiabatic temperature change induced by a sweeping magnetic field from $\mu_0 H_i$ to $\mu_0 H_f$.

$$\Delta T_{ad}(T,H) = -\mu_0 \int_{H_i}^{H_f} \frac{T}{C_p(T,H)} \left(\frac{\partial M}{\partial T}\right)_{H,p} \mu_0 dH \tag{2.14}$$

These relations constitute the basic description of the thermal properties behavior for systems stressed by the action of an external magnetic field.[6, 5, 7] As it will be better described in the following, it can be noticed that both ΔT_{ad} and Δs_T depend on the first order derivative of magnetization in temperature, which is large across the magnetic phase transitions. While discussing the results of this work I will refer to specific entropy per unit mass to better compare the studied material with different alloys: in this case the small character is to be used.[8] The slope in the magnetic phase diagram of the magnetization as function of temperature determines if the magnetocaloric effect is positive or negative.

For localized magnetic systems the total entropy can be approximated as

$$S(T,H) = S_l(T) + S_e(T) + S_M(T,H) \tag{2.15}$$

where $S_l(T)$ is the term describing the lattice entropy variation, $S_e(T)$ and $S_M(T,H)$ represent the electronic and magnetic contributions. For these materials it is considered that just the entropy change linked to the spin lattice contributes to the total isothermal entropy change induced by the external field: $\Delta S_T(H)_{tot} = \Delta S_T(H)_M$. The first term of the right side of eq. 2.15 is described by the Debye theory which gives an expression of the phononic contribution to the total entropy:

$$S_l(T) = n_a R \left[-3\ln(1 - e^{T_D/T}) + 12 \left(\frac{T}{T_D} \right)^3 \int_0^{T_D/T} \frac{x^3 dx}{e^x - 1} \right] \tag{2.16}$$

where n_a is the number of atoms per molecule, T_D is the Debye temperature and R the gas constant. The term related to the electronic degrees of freedom shows a linear dependence with temperature:

$$S_e = a_e T \tag{2.17}$$

with a_e as the electronic heat capacity coefficient.[5] The entropy contribution due to N magnetic noninteractig sites with total angular momentum J is deduced from the first order derivative of their Free energy on temperature (see eq. 2.4). The statistical expression of Free energy ($F = -kT \ln Z$) follows from their Canonic partition function:[5, 9]

$$Z = \left[\frac{\sinh\left(\frac{2J+1}{2J}x\right)}{\sinh\left(\frac{x}{2J}\right)} \right]^N \tag{2.18}$$

where x represents the ${}^{gJ\mu_b H}/_{kT}$ ratio with μ_b as the Bohr magneton, k is the Boltzmann constant and g the Lande's factor. The entropy contribution due to the configurations of the magnetic system has then the following form:

$$S_M(T,H) = Nk \left[\ln\sinh\left(\frac{2J+1}{2J}x\right) - \ln\sinh\left(\frac{x}{2J}\right) - xB_J(x) \right] \tag{2.19}$$

$B_J(x) = \frac{2J+1}{2J}\coth(\frac{2J+1}{2J}x) - \frac{1}{2J}\coth(\frac{1}{2J}x)$ is the Brillouin function which for J=1/2 reduces to the hyperbolic tangent: $B_J(x) = \tanh(x)$.

At high temperatures and low applied fields $x << 1$: in this case equation 2.18 can be approximated through a power series of x and the expression of magnetic entropy becomes:

$$S_M(T,H) = Nk \left[\ln(2J+1) - \frac{1}{2}\frac{CH^2}{T^2} \right] \tag{2.20}$$

where C is the Curie constant. For $T \to \infty$ the last term in the bracket vanishes and it can be estimated the maximum value of entropy that a magnetic system with total angular momentum J can achieve.

$$S_M^{max}(T,H) = Nk\left[\ln(2J+1)\right] \tag{2.21}$$

This value is the maximum limit of magnetic entropy change for the system. This expression has been fruitful to demonstrate the inconsistency of some MCE "ghost" data reported in literature.[10] While studying first order processes these $\Delta S_T(H)$ values even larger than $S_M^{max}(T,H)$ were presented due to incorrect measurement protocols which didn't take properly into account hysteresis effects.

Clausius-Clapeyron relation

The thermodynamics previously described is applicable when are analyzed states in equilibrium conditions.[5] The thermodynamic processes are considered as constituted by a sequence of reversible points. This constraint allows thus to

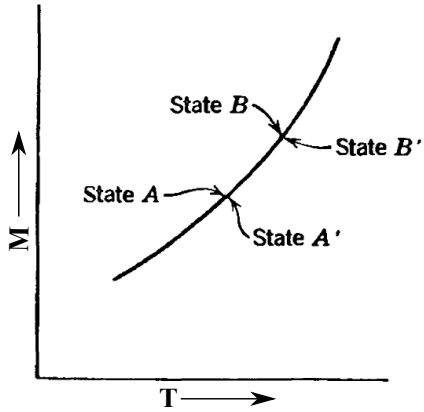

Figure 2.2: Clausius - Clapeyron equation

describe states where the magnetization derivative on temperature does not diverge: $\frac{dM}{dT} \neq \infty$. Second order transitions and states far away from critical points generally satisfy the previous requirement.

There has been a long debate which still lasts about the suitability of the Maxwell relations to describe the magnetic phase diagram across first order phase transitions.[10] Some authors assert that real first order transformations do not show discontinuity on their first order derivative of the free energy. This implies that in these systems the Maxwell relations turn out to be analytically allowed. On the other hand it was also suggested the use of the Clausius - Clapeyron equation for this kind of processes.[11]

Clausius - Clapeyron relation describes the system behavior near first order transformations, regarding that the chemical potentials of the two phases (μ and $\mu^{'}$) equal on the transition coexistence line.[4] Considering a Magnetization vs. Temperature phase diagram, the infinitesimal difference between two points A and B ($d\mu = \mu_B - \mu_A$) on the coexistence curve have to be the same for the two states (see fig. 2.2).

$$\mu = \mu^{'}; \qquad d\mu = M\mu_0 dH - SdT \tag{2.22}$$

$$M\mu_0 dH - SdT = M^{'}\mu_0 dH - S^{'}dT; \qquad \mu_0 \frac{dH}{dT} = \frac{S^{'} - S}{M' - M} \tag{2.23}$$

Thus the form of the isothermal entropy variation becomes:

$$\Delta S_T = \mu_0 \frac{dH}{dT} \Delta M \tag{2.24}$$

This quantity is related to the fully induced process, which is described as a step in the phase diagram. In this way an estimation also of the total enthalpy difference between the phases can be deduced since $\Delta E = T\Delta S_T$.

$$\Delta E = T\mu_0 \frac{dH}{dT} \Delta M \tag{2.25}$$

2.2 Materials

The MCE is directly linked with the first order derivative of magnetization on temperature (see eqs. 2.10 and 2.14). Magnetic phase changes are processes where large $\frac{dM}{dT}$ values and thus large MCE are reported. The most promising materials for applications show then near room temperature second order Curie transitions or first order processes where the changing magnetic system is coupled with a structural rearrangement. In some cases this structural transformations involve a symmetry change of the lattice while other materials can show a volume discontinuity between the two phases keeping however the symmetry.[12, 9, 13]

The most studied systems so far are Gadolinium based compounds (in particular *Gd-Si-Ge*), *La-Fe-Si* and *Fe-P*-based alloys. The $Gd_5Si_2Ge_2$ systems showing the larger MCE values are characterized by a first order magneto-structural transformation between a ferromagnetic and a paramagnetic phase.[9, 14, 13] This process can be induced both by pressure (since the two phases have different volumes) and magnetic field. The purity of the parent elements influences the transformation MCE as well as its hysteresis thus lowering the efficiency of such alloys. Another drawback of such materials is the availability of Gadolinium and Germanium.[9] The MCE in *La-Fe-Si*-based materials is due to the presence a first order itinerant metamagnetic transition above the Curie temperature. This process, which occurs in Fe rich alloys between 200K and 260K, can be shifted to higher temperatures properly adding interstitial elements as hydrogen or cobalt. The hydrogenation process furthermore increases the magnetization and the volume of the system. These changes of the lattice parameters can lead

to enhanced material brittleness on subsequent magnetization and demagnetization cycles.[12, 9] A first order volume change transformation distinguishes the Fe_2P alloys. Across this process the MCE is direct and a discontinuous change in the c/a ratio takes place. The structure is hexagonal both for the low and the high temperature phases and allows a large number of substitutions which are functional to tune the properties of the process. The small hysteresis in these systems makes the MCE of these transitions almost reversible in magnetic field.[12, 9, 15]

In the following are described a little more in detail the materials that have been mainly studied in this work.

2.2.1 Gadolinium

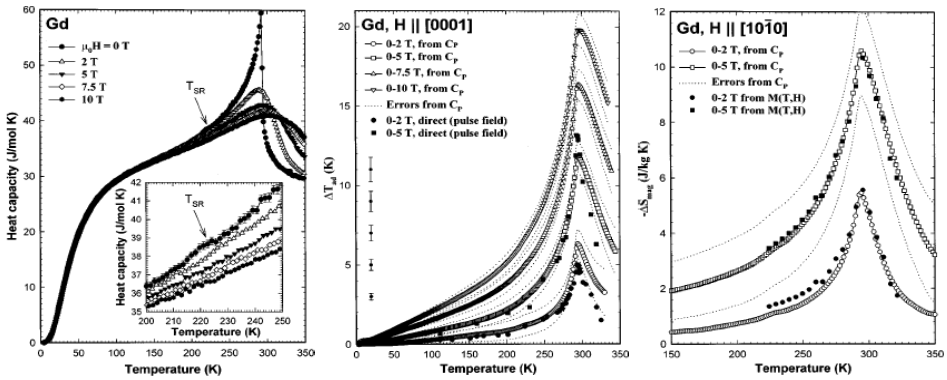

Figure 2.3: Gadolinium specific heat, ΔT_{ad} and Δs_T both temperature and magnetic field dependent.[16]

Gadolinium is a rare earth element which crystallizes in an hexagonal close packed structure. It is the only ferromagnetic element showing the Curie transition near room temperature. It is considered as a classical ferromagnet since it can be described through a spin lattice with total spin moment $S = \frac{7}{2}$ on every site. The magnetic moment comes from the electronic state: the f-shell is half filled and the electronic spins are aligned. Gadolinium specific heat is quite low: $c_p \sim 300 Jkg^{-1}K^{-1}$ near room temperature in zero magnetic field. Its thermal conductivity is $k \sim 10 Wm^{-1}K^{-1}$. Concerning its magnetothermal behavior gadolinium is the most studied system so far. It is characterized by a high MCE

in a large region of its phase diagram across its Curie temperature ($T_c \sim 292K$). The entropy change across its Curie temperature can reach values of $5Jkg^{-1}K^{-1}$ and $10Jkg^{-1}K^{-1}$ for field spans of 2T and 5T. At the same fields the adiabatic temperature change can be also 5K and 11K.[16] The low specific heat allows quite large magnetic field induced ΔT_{ad}. It is considered as the best MCE performing material, since almost all the working magnetic refrigerators so far exploit the magnetothermal properties of such system.[17, 18] The drawbacks concerning the use of this element are its cost, the its purity degree which strictly affects its thermal behavior together with its tendency to tarnish in moist air.[19, 16]

2.2.2 Ni-Mn-X alloys

The martensitic transformation is the fingerprint of these systems. This structural transformation is among the most common diffusionless solid-solid transitions. It induces a change of the symmetry of the lattice while the cell parameters variations are small since the atomic movements are short range. The interface motion is a coordinated phenomenon.[20, 21] It was estimated (studying *Fe-Ni* alloys) that its propagation rate ($\sim 10^3$ ms^{-1}) approaches the speed of sound and is temperature independent.[21] The displacive nature of the transformation implies that the parent and the product phase have the same composition.

A simple representation of the system Free energy is drawn in fig. 2.4. T_0 is the temperature where the chemical potentials of austenite and martensite are equal. Martensite is stable when the system temperature falls below T_0 while we observe the transition to austenite when the system temperature rises above T_0. In this sketch A_s and A_f represent the points where starts and finishes the transformation process while the system is heated over the "equilibrium point" (T_0). If the system is cooled from austenite to martensite the transition takes place between M_s and M_f. The transformation widths are then $A_f - A_s$ and $M_s - M_f$ on heating and on cooling, respectively.

Sometimes the phase change can be characterized by local irreversibility and thus in such cases hysteresis is observed. The term "local irreversibility" means that the heating and the cooling states are not coincident and to transform to the lower or to the higher phase a system overcooling or overheating is required below and above T_0. The transformation hysteresis can then be expressed as: $\Delta T_{hyst} = \frac{A_f + A_s}{2} - \frac{M_s + M_f}{2}$. The solid state phase change involves a volume vari-

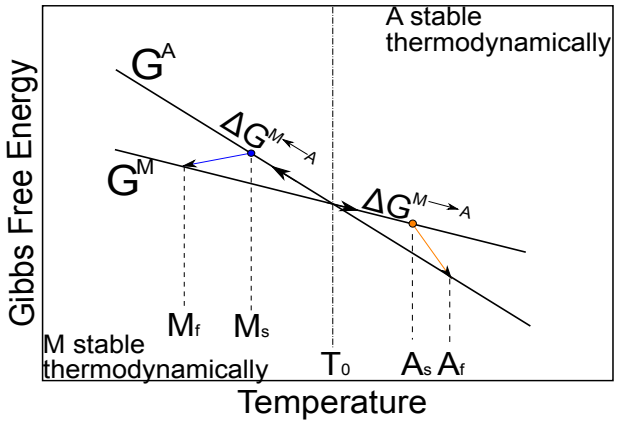

Figure 2.4: Representation of the martensitic phase diagram

ation between the two phases. The thermal hysteresis, which is peculiar of this kind of processes together with latent heat, is a marker of their first order nature. The process hysteresis can increase if high volume cell variations characterize the transition between the two phases. Pronounced lattice distortions induced by the nucleation of the new phase in the parent one cause the onset of large elastic energies which promote irreversible effects.[20] The hysteresis of the process depends whether or not the accommodation of the new phase is accompanied by an irreversible plastic strain. More pronounced are the plastic strains that the new phase induces on the parent lattice, higher is the irreversibility of the process. Thermal treatments can help the structure to relax thus lowering the internal mechanical stresses: this can modify the type of transformation and the size of hysteresis.[20]

The possibility, by suitably varying the composition, to change both the structural and the magnetic properties,[22] together with the critical temperature of the transformation, makes these materials very attractive for a variety of applications: previous studies highlighted their magnetoelastic behavior[23, 24] which could be exploitable in innovative sensors and actuators[25, 26]. Concerning the magnetocaloric properties, viable experimental routes for enhancing both the direct[27] and the inverse martensitic MCE have been developed[28] involving the merging of the structural and the magnetic critical temperatures.[29]

The particular alloy studied in this work is characterized by a $Ni_{2+x}Mn_{1+y}Ga_{1+z}$

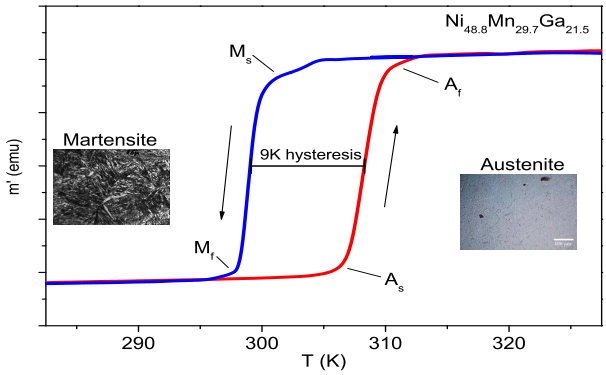

Figure 2.5: Thermal behavior of the martensitic transformation

stoichiometry with $x+y+z=0$. The intermetallic compounds with A_2BC formula belong to the Heusler alloys. In the previous formula A corresponds to a transition metal, B to manganese, while C can be a semimetal such as germanium, gallium, tin, antimony, aluminum, indium. In fig. 2.6 c the $L2_1$ austenitic structure is reported: manganese and gallium atoms occupy the positions at the apexes (4a and 4b sites in Wyckoff notation), while nickel occupy the positions at the center of the cube (8c sites).[20, 30] The structure can be described as four different interpenetrating sublattices with origins in: $(0,0,0)$, $\left(\frac{1}{2},\frac{1}{2},\frac{1}{2}\right)$, $\left(\frac{1}{4},\frac{1}{4},\frac{1}{4}\right)$, $\left(\frac{3}{4},\frac{3}{4},\frac{3}{4}\right)$. In figure 2.6 a, the symmetry of the product phase is described with a I-centered unit cell having the fundamental axes coincident with the [1 0 $\overline{1}$], [1 0 1] and [0 1 0] directions of the $L2_1$ superstructure.[31] The structure of the low temperature martensitic phase is a result of the spontaneous uniform lattice distortion of the parent cubic austenitic phase. The distorted lattice can be tetragonal, orthorhombic or monoclinic, depending on the composition of Ni-Mn-Ga alloy and the temperature.[32]

Especially for higher contents of the "C" element modulated crystal arrangements (nM structures) have been reported, deduced by the presence of multiple weak reflections recorded in diffraction patterns which cannot be indexed by the conventional unit cell.[30, 31, 32, 33] This feature is due to the instability of the parent cubic structure which induces, besides the shear deformation of the lattice, shuffling of atomic layers along selected crystallographic directions. The modu-

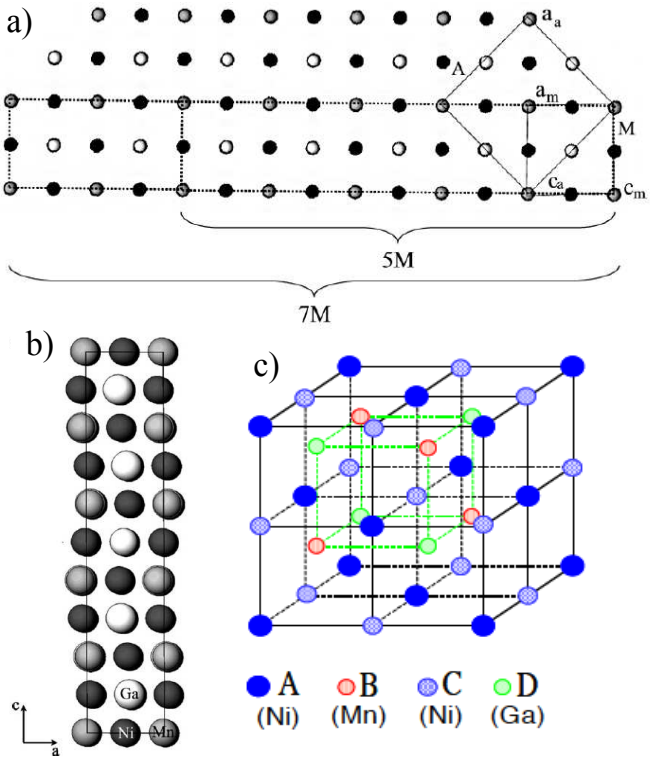

Figure 2.6: Austenite conventional cubic cell.[20]

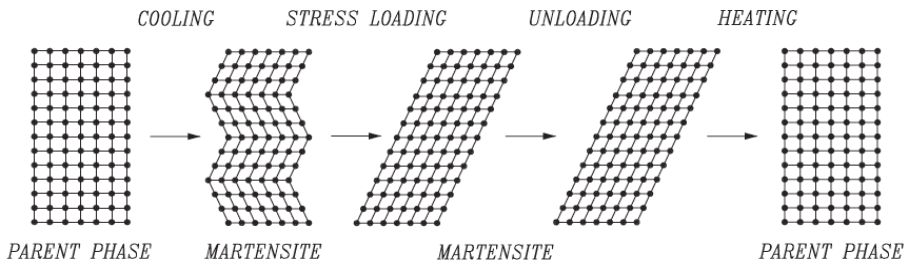

Figure 2.7: Shape memory behavior.[30]

lated superstructure involves n consecutive unit cells along the [1 $\overline{1}$ 0] direction of the $L2_1$ lattice.The most common are the 5M and the 7M modulated structures (fig. 2.6 b)[33]. 'M' refers to the monoclinicity resulting from the distortion associated with the modulation, while n=s+1 where "s" represents the number of satellite reflections detectable between the main ones. This classification does not describe the occurrence of incommensurate modulations.[31]

Martensite can show also intramartensitic lattice rearrangements. Such processes appear only for some compositions and sometimes can be difficult to be detected with magnetic characterization, since they involve slight atomic displacements whose entity is much weaker than the austenite-martensite phase change.

Shape memory materials

The martensitic transformation is the basis of the shape memory behavior. Such materials are able to recover their initial macroscopic shape after being stressed above their elastic limit. This feature makes them attractive as mechanical devices in medicine and as temperature controlled detachable and nondetachable joints.[20] In single crystals moreover the stress induced deformations can reach $\sim 10\%$.[30] The shape memory behavior is reported in figure 2.7.

Cooling the material from the austenitic cubic lattice the system transforms to the martensite while keeping its macroscopic shape. This phase, characterized by lower volume and lower symmetry, is organized in different variants. These configurations are energetically equivalent and are the effect of the low symmetry of the martensitic phase. In perfect crystals without any external load the shape of the mechanical pattern in which the lattice stabilizes has no constraints while for

real materials dislocations can favor some particular configurations. The effect of a stress applied to the martensitic structure can then induce the orientation of the lattice cells in a precise direction due to the variants twin boundary motion. The deformation induced can be of several percentage points. At this stage heating the sample it occurs the reverse martensitic transformation and the material, coming back to the cubic austenite, recovers its first shape.[30] This feature allows then to force the system to recover also very particular geometries (as is also shown by many videos on internet).[34, 35] The forced induction of favoured centers of heterogeneous nucleation makes it possible to control the process of martensitic transformation under cyclic variations in the temperature.[20] One of the ways to do this is a system thermal treatment under applied mechanical load.

Magnetic Heusler alloys are characterized by high saturation moments. The interplay between the magnetic system and the structure for these materials can lead to non negligible deformations induced by the external magnetic field.[30] The martensitic phase of Ni-Mn-Ga alloys in particular is characterized by high magnetic anisotropy. This feature implies that the effect of magnetic field is the same as the one of previously described for mechanical stress. When a magnetic field is applied to the martensitic phase (well below the martensitic transformation) the energy of two of the three variants is increased and the system organizes along the direction of the preferred one.

If the external action (stress or magnetic field) on the system is strong enough to overcome the hysteresis, thus it stabilizes (as an example) the higher temperature phase at below the "zero field" M_f point, superelasticity is observed. This effect does not involve any rearrangement of the martensitic structure but is due to the complete and reversible occurrence of the martensitic transformation. "Conventional" superelasticity is induced mechanically by the application of an external stress, when the magnetic field is responsible of this effect it is named magnetic superelasticity.[30]

MCE of Ni-Mn-X alloys

Across the transformation the action of the magnetic field favors the phase where stronger are the magnetic interactions. Depending on the magnetic nature of the two phases an external field favors the low or the high temperature one. The classical MCE (the action of the external field lowers the entropy and shifts the

Table 2.1: $\Delta T_{ad}(T)$ values directly measured across the martensitic first order transformation (on heating) for different Ni-Mn based Heusler alloys in a $\mu_0 H = 1.9$T field span. $\Delta T_{ad}(T)$ values related to other transformations (T_M on cooling and T_c) are also listed.

Sample stoichiometry	Ref.	T_M	ΔT_{ad}^{heat}	ΔT_{ad}^{others}
$Ni_{47}Mn_{33}Ga_{20}$	[37]	355K	1K	–
$Ni_{48.3}Mn_{37.5}Sn_{14.2}$	[38]	314K	−0.3K[1]	–
$Ni_{54.5}Mn_{20.5}Ga_{25}$	[39]	335K	0.8K	1.8K (T_M^{cool})
$Ni_{54.75}Mn_{20.25}Ga_{25}$	[40]	335K	0.8K	1.2K (T_M^{cool})
$Ni_{50}Mn_{34}In_{16}$	[41]	225K	−1.15K	1.6K (T_c)
$Ni_{50}Mn_{34}In_{14}Ga_2$	[41]	225K	−0.75K	1.1K (T_c)
$Ni_{50}Co_1Mn_{36}Sn_{13}$	[42]	295K	−1.1K	1.15K (T_c)
$Ni_{50}Mn_{35}In_{15}$	[43]	295K	−1.65K	1.9K (T_c)
$Ni_{50}Mn_{35}In_{14}Ge$	[43]	308K	−1.54K	1.4K (T_c)
$Ni_{50}Mn_{35}In_{14}Al$	[43]	303K	−1.8K	1.75K (T_c)
$Ni_{55.25}Mn_{19.25}Sn_{25.5}$	[44]	335K	1.5K	–
$Ni_{45.2}Mn_{36.7}In_{13}Co_{5.1}$	[36]	317K	−6.2K	2K (T_c)
$Ni_{49.8}Mn_{35}In_{15.2}$	[36]	235K	−5.2K	2K (T_c)
$Ni_{50.4}Mn_{34.8}In_{15.8}$	[36]	192K	−3.6K	2K (T_c)

transformation to higher temperatures) can be observed when martensite is the high magnetic moment system, while inverse MCE (the action of the external field increases the entropy and shifts the transformation to lower temperatures) occurs if the austenite shows the strongest magnetic interactions. The occurrence of magnetic superelasticity involves interesting magnetocaloric properties: a material characterized by a fully reversible martensitic transformation in magnetic field will show also a reversible magnetocaloric effect being thus suitable for applications. In table 2.1 are listed most of the up to now reported direct MCE measurements on *Ni-Mn* like systems. The last three values are the last reported data from the work of Liu et al.[36] All the data summarized across the martensitic transformation correspond to irreversible effects which do not take into account the effect of hysteresis on the subsequent action of the external field.

Data from reference [36], which were published at the end of this work, concerning the study of the magnetocaloric effect on Heuslers could contribute to move almost all the attention on *Ni-Mn-In* based materials. As it was already shown *Ni-Mn-In* alloys are characterized by higher ΔM and ${}^{\Delta T_M}/_{\mu_0 \Delta H}$ values across the martensitic transformation which usually are markers of large MCE.[23, 42] Similar values have never been observed in *Ni-Mn-Ga*, *Ni-Mn-Sn*, *Ni-Mn-Al* based materials. However the reduction of the hysteresis is still a critical issue which up to now prevents the use of such systems (also the best up to now reported one: $Ni_{45.2}Mn_{36.7}In_{13}Co_{5.1}$) as active magnetic refrigerants in real magnetothermal cycles.

Co substituted Ni-Mn-X alloys

The partial substitution of Ni by Co in Mn-rich alloys was found to lower the martensite magnetic interactions while enhancing those of austenite[45, 46]. The magnetic field thus favors the austenitic phase while the martensitic transformation temperature is shifted to lower temperatures (see as an example fig. 2.9). This behavior reflects an inverse MCE and the action of the magnetic field increases the system entropy. The transformation from martensite to austenite leads to a reduction of the temperature of the material in adiabatic conditions. Some compositions show a paramagnetic martensitic region before the occurrence of a ferromagnetic austenite. Since such feature enables high values both of ΔM at the T_M and of ${}^{\Delta T_M}/_{\mu_0 \Delta H}$, the magnetothermal behavior of such systems turns out then to be very intriguing as it will be described in chapters 3 and 4. The phase diagram resulting from this substitution on the structural and the magnetic critical temperatures as well as on the magnetic properties has recently been traced and is reported in fig. 2.8.[46, 47, 48] Remarkable ΔV of about 1% between the cell volumes of martensite and austenite have been reported for samples with higher Co and Mn concentrations.

To deepen the magneto-thermal behavior of martensite and austenite five different regimes are shown in figure 2.8 depending on composition (for 5<Co<9 and 30<Mn<32). They are characterized by a different number of first and/or second order transitions evidenced by the temperature dependence of the magnetic susceptibility. Panel a) reports the parent Co-free sample (i.e. Co=0, Mn=30) where the martensite Curie transition and the martensitic transformation coincide.[49]

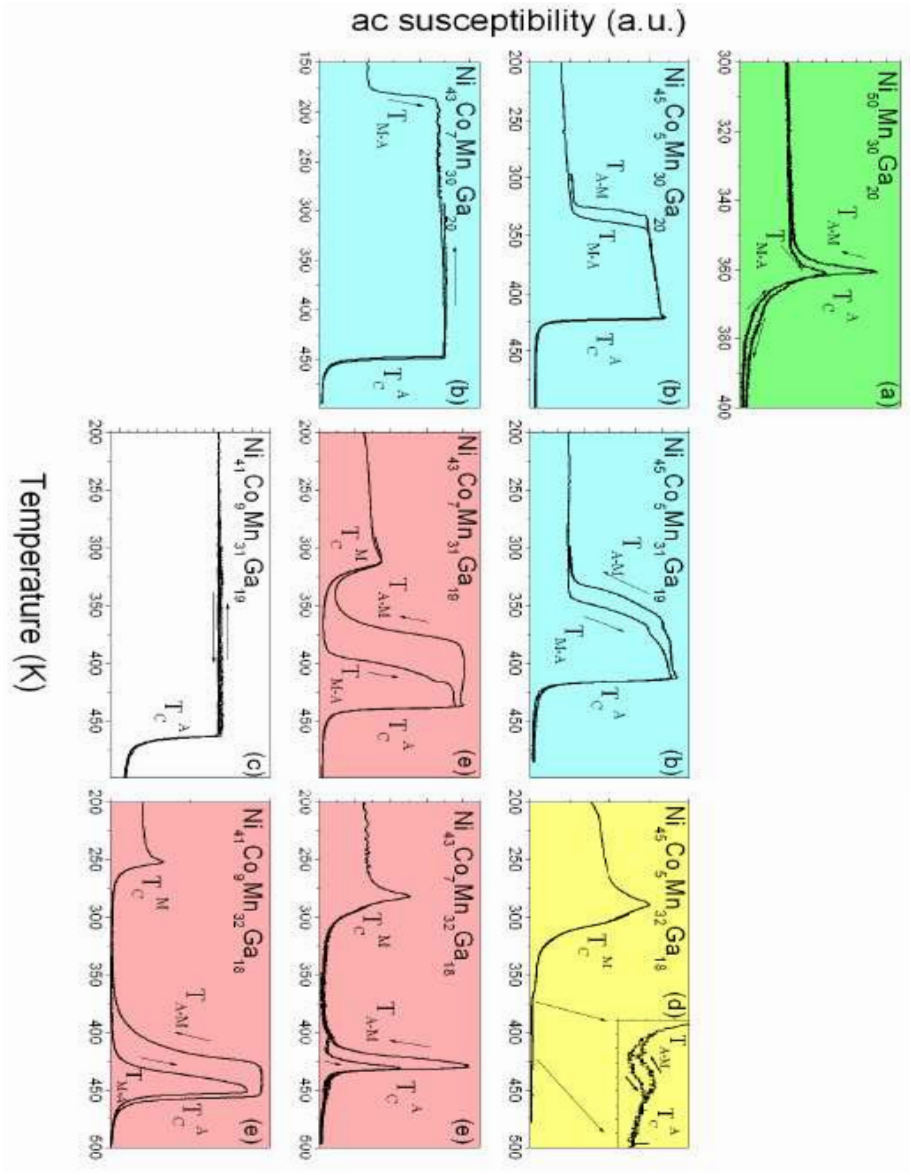

Figure 2.8: Composition dependence of martensitic transformation temperature and magnetic behavior of martensite and austenite.

For low Co and Mn content (fig. 2.8 b) the martensitic transformation occurs at a much lower temperature than the austenitic Curie transition, while for high Co and low Mn content the martensitic transformation is suppressed and the sample is cubic at all temperatures (fig. 2.8 c). Figure 2.8 d shows a system where ferromagnetism is present only in martensite. For Co$\geq$ 7 and Mn$\geq$ 31 the first order martensitic transformation occurs between the second order Curie transitions of martensite and austenite (Fig. 2.8 e). It can be observed that the a.c. susceptibility is nearly zero in the region right before the magneto-structural process, i.e. the material is paramagnetic. The presence at higher temperatures of the austenitic Curie point however induces by heating the reoccurrence of the ferromagnetism after crossing the martensitic transformation. This reverse magnetic transition shows inverse MCE and high jumps of magnetization which can be induced by temperature, magnetic field and pressure.[48, 47]

The origin of the strengthening of austenite magnetic interactions compared to martensite can be partially explained taking into account the site occupancy by the atomic species. In an ideal configuration, Co should replace Ni atoms. In a localized description of Ni-Mn-X alloys the magnetic moment is mostly confined on Mn atoms and the ferromagnetic interactions between Mn sites can be inferred to be positive for $Ni_{50}Mn_{25}Ga_{25}$. Increasing the Mn concentration (Mn$\geq$ 25) the off stoichiometric atoms occupy Ga sites. The Mn of a 4b site induces antiferromagnetic interactions with the Mn of the 4a sites. For Mn=31 content a statistical distribution is realized for which every cell contains one Mn atom on a 4b site. Above that amount Co was found to induce an abrupt decrease of martensitic saturation magnetization.[48, 47] On the other hand Cobalt, differently from manganese, increases the austenite magnetic interactions.[48, 47]

When the system transforms from martensite to austenite the volume change is always positive. In this compositional range it is observed a proportional increase of the relative cell volume ($\frac{\Delta V}{V}$) depending on the Co content (from $\frac{\Delta V}{V} \sim 0.45\%$ in $Ni_{45}Co_5Mn_{30}Ga_{20}$ alloy to $\frac{\Delta V}{V} \sim 0.8\%$ in $Ni_{41}Co_9Mn_{32}Ga_{18}$). This behavior is very similar to the composition dependence of saturation magnetization jump at the transformation (ΔM) which increases for high Co and Mn due to the presence of the martensitic paramagnetic gap.

It was also verified[48] that the lowering of the T_M while preserving the magnetic properties can be obtained by homovalent partial substitution of the *sp*

element, as shown by Aksoy and co-workers in Ni-Mn-(Ga,In) samples.[41] This peculiarity (the substitution of Ga with In) turns out to be convenient if some promising compositions, which are discriminated by high $|\Delta M|$ and $\frac{|\Delta T_M|}{\mu_0 \Delta H}$ of the martensitic transformation, show the phase change at temperatures higher than the ambient. These are peculiar features of materials showing high MCE.

2.3 Characterization techniques

2.3.1 Magnetometry

Magnetic characterization allows to map the magnetic phase diagram of the material. Small sized fragments (few milligrams or less) are generally used while performing magnetic characterization. This is justified by the soft ferromagnetic behavior of all the materials studied for magnetic refrigeration applications. It has been shown that the magnetocaloric potentials (ΔT_{ad} and Δs_T) maximize near their critical points. The identification of such points in the material phase diagram is then the first step while analyzing its magnetothermal behavior. The most common characterization for this purpose is then magnetometry since it is generally the most simple, available and convenient. Both ac and dc techniques can be firstly used: both susceptibility and magnetization are quantities which discriminate the peculiar phase of the material. Once the material transition temperatures are identified, an important issue is the investigation of the effect of an applied magnetic field on this processes. The proper way to do this is measuring magnetization isotherms and isofields curves, which in case of first order magnetostructural transformations allow to directly deduce some key magnetocaloric parameters. The entity of the magnetization jump across the process (ΔM_s) is one of these.[42] It is expected that large magnetization differences between the phases could lead to high sensitivities of the transformation temperature to the applied field ($^{\Delta T_M}/_{\mu_0 \Delta H}$). This is justified since the action of the magnetic field stabilizes the phase characterized by stronger magnetic interactions, widening it in temperature. It has been shown that both high ΔM_s and $^{\Delta T_M}/_{\mu_0 \Delta H}$ are marker of large MCE.[23]

The transformation temperature shift induced by the external field ($^{\Delta T_M}/_{\mu_0 \Delta H}$) determines the sign of the first order derivative of magnetization on temperature which appears in the Maxwell relation. While the magnetic field is turned on

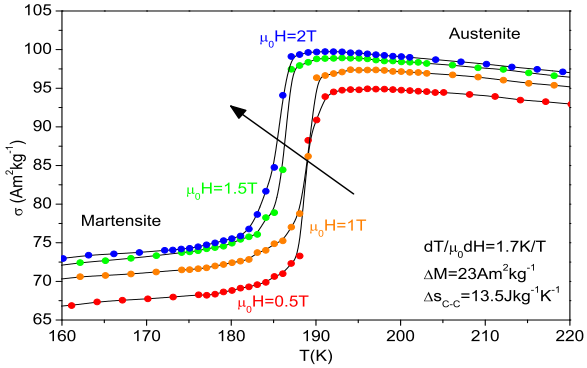

Figure 2.9: Isofield magnetization curves on heating across the inverse martensitic transformation of $Ni_{43}Co_7Mn_{30}Ga_{20}$

the esothermic or endothermic behavior of the process is discriminated by the positivity or negativity of this term. From isofield magnetization curves, collecting the first order derivative peaks, it can be constructed the H_c vs. T_c phase diagram (H_c and T_c are the field and temperature critical points of the transition). The presence of hysteresis is described both in temperature and magnetic field. This phase diagram is the simpler and faster way to find out which is the minimum field span, depending on temperature, necessary to cycle between the two phases. A martensitic transformation characterized by a fully reversible MCE shows also magnetosuperelasticity for the same magnetic field span.

Both isofield and isotherm magnetic characterization can be used to calculate (see eq. 2.10) the material entropy change on the basis of Maxwell relations.[50, 5] The most common approach to estimate the Δs_T is to perform a numerical integration, using the trapezoidal method,[51] of the M(H) curves across the transition. The correct application of the Maxwell relations has been under debate in the last years.[52, 50, 53, 54] It is unquestionable for reversible transitions where the process can be considered as a sequence of equilibrium states. Real first order transformations, besides they should show a discontinuity in the first order derivative of Free Energy,[4] on the other hand occur in finite temperature or magnetic field intervals, being far from purely step-like. This implies that the $(\partial M/\partial T)_H$ parameter does not diverge. The integration of the isothermal curves, also in this

case, if properly probed, turns out to be analytically allowed.[10] In case of hysteresis the specification "if properly probed" means to take care to follow exactly the magnetic state to be characterized, avoiding the occurrence of minor transformation loops.[55] In case of reversible processes this issue does not exist since only one system state exists independently of the experimental conditions (magnetic field increasing or decreasing). It has been shown that the integration of isofield curves could avoid some experimental problems while studying irreversible transformations.[50] This can be explained since while performing a isofield measurement the temperature scan always fully induces the transformation. Moreover before starting the subsequent acquisition the system state is fully brought back to the parent phase. The elaboration from M(T) data should imply a sufficient number of curves for different fields and a high number of data in temperature to have a good estimation of the Δs_T. The use of Clausius-Clapeyron equation is justified for first order transformations.[11] The parameters required to estimate the Δs_T of the fully induced process ($^{\Delta T_M}/_{\mu_0 \Delta H}$, ΔM) can be obtained both form M(H) and M(T) curves. Casanova et al. (Ref. [56]) showed that a good convergence can be observed between the entropy change values obtained from Clausius-Clapeyron and Maxwell relations, provided that in the latter case the minimum magnetic field necessary to fully induce the transformation is applied.

Magnetometry is a convenient technique since it gives quickly, without the necessity to develop a dedicated setup, an effective description of the magnetothermal behavior of the system. On the contrary it is the "most indirect" way to deduce the magnetocaloric properties of the materials: this implies large errors linked with the calculated values. The easiness of this technique can constitute also a drawback. The effect of demagnetizing fields is generally not taken into account while its influence on the MCE is quite never negligible.[57] Moreover it has been shown how the analysis of irreversible processes can lead to huge overestimations of the effect if a proper measurement protocol is not adopted.[10]

2.3.2 Calorimetry

The measurement of the magnetic field dependent thermal properties of the system gives the entity of the MCE. Isothermal and adiabatic techniques are the most direct experiments since $\Delta s_T(\Delta H, T)$ and $\Delta T_{ad}(\Delta H, T)$ are deduced straightforwardly. Differential Scanning Calorimetry (DSC) and relaxation calorimetry in

magnetic field allows the estimation of the material specific heat ($c_p(T,H)$). In this way the entropy diagram of the system both temperature and magnetic field dependent can be built after integration of c_p curves (from eq. 2.12):

$$s(T,H) - s_0 = \int_{T_i}^{T_f} \frac{c_p(T,H)}{T} dT \tag{2.26}$$

The calculation of s(T,H) curves offers at the same time an estimation of both $\Delta s_T(T,\Delta H)$ and $\Delta T_{ad}(T,\Delta H)$. A detailed analysis of the errors and of the main issues involved in this characterization has been reported in Ref. [51, 58]. The high versatility of instruments which measure the system specific heat justifies their wider spread if compared to purely adiabatic or isothermal techniques which allow the study of just one of the two quantities.

Adiabatic temperature change experiments

The development of ΔT_{ad} experimental setups however turns out to be fundamental if the requirement is a precise and quick measurement of the material temperature change and the observation of the effective behavior of the studied systems in adiabatic conditions. As an example, planning to perform thermomagnetic cycles characterized by adiabatic branches. The specification of "precise measurements" means that this technique, if a proper operation of the instrument is adopted, allows the reduction of experimental errors as compared to indirect techniques, for which the error propagation enhances the uncertainty of the final value. The magnetic field can be varied in different ways while performing direct ΔT_{ad} measurements. Faster field sweeps (10^{-2}s - 10^{-1}s) can be achieved with pulsed fields,[59] while slower ones (10^{-1}s - 10^{0}s) are induced by mechanically moving the probe or the magnet (see figure 2.10),[60, 61, 62] or by switching on and off an electromagnet[59, 36, 63, 64, 65]. Setups where the sample is kept always in the same position are more convenient since the quasi-adiabatic conditions are easier to reproduce, while if the material is moved in the cryostat in and out of the field problems with the temperature control could arise in the region far from the standard sample position. The typical used sensors are: thermocouples[59, 65, 61, 36, 63, 64, 66], high precision thermoresistances with low magnetic field dependence,[60, 62] and in some cases IR cameras or microphones.[67, 68] Samples of quite high masses ($m > 20$mg) are necessary to

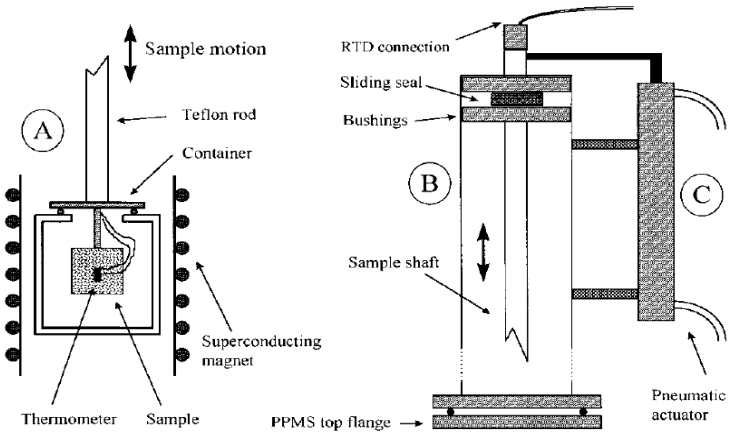

Figure 2.10: Experimental setup for the measurement of the ΔT_{ad}. A pneumatic actuator induces the field change. A) Vacuum chamber and sample+sensor, B) and C) Experimental pneumatic setup[60]

get reliable results with this technique.

In the case of electric conductive sample the effect of magnetic field induced eddy currents on the directly measured temperature change is generally not discussed in literature. It can be estimated however that a field sweep of $\sim 2\mathrm{Ts}^{-1}$ on a gadolinium sample of 3mmx3mmx3mm (electric resistivity $\sim 1.3 \cdot 10^{-6}\Omega\mathrm{m}$) should induce by eddy currents a temperature increase of the order of $10^{-2}\mathrm{K}$. This effect is generally hardly detectable in low fields ($\mu_0 \Delta H = 2\mathrm{T}$) when comparing "heating" and "cooling" $\Delta T_{ad}(T)$ curves (as suggested in Ref. [60]).

There are two main advantages of this technique: it is in principle easy to realize and it gives a direct estimation of the temperature change: this is the most important parameter when treating applications of MCE in energy conversion devices. On the other hand great attention should be adopted on using this technique. It can be uncomfortable since particular care is necessary while mounting the samples to avoid damages of the temperature sensor and to do a stable and optimized thermal contact. In some cases a special care is required to avoid the detection of voltage peaks induced by the varying magnetic field in the wiring conductors used to measure the sensor resistance.

Differential Scanning Calorimetry (DSC)

The measurement of temperature and magnetic field dependent specific heat ($c_p(H,T)$) can be performed using Differential Scanning Calorimetry (DSC) and relaxation calorimetry. A large number of commercial DSC are available for the estimation of specific heat and latent heat of first order processes, however these instruments are not suitable for working in magnetic field and several problems arise when carrying out such experiments (mechanical effects on ferromagnetic parts and on the sample itself and magnetic field dependence of the sensors). Both in-field relaxation and DSC techniques have to be properly built up. The higher accuracy of differential scanning calorimeters if compared to relaxation setups supported their recent spread.[17] The DSC technique, measuring directly the heat flux flowing between sample and calorimeter once defined a temperature sweep rate, is particularly suitable for the detection of latent heat. This feature is specially important when studying the MCE of first order processes.[69] The idea to use Peltier elements as heat flow sensors was firstly proposed by Plackovski.[70] Other experimental setups were then developed based on the same technology.[71, 72, 73, 74]

Differential scanning calorimeters work forcing the sample to follow a constant temperature sweep. The finite thermal conductance of the sensor, put between sample and the calorimeter structure, is the origin of a temperature difference. Through Seebeck effect the Peltier elements convert this temperature difference in a voltage drop. Since the cells thermal conductance can be considered quite independent of the magnetic field and not characterized by abrupt variations in temperature, the temperature difference between the plates multiplied by the cell thermal conductance (K_{cell}), gives the heat flux ($\dot{Q}$) which flows between sample and calorimeter:

$$\dot{Q} = \frac{\Delta V_{cell}}{S} K_{cell} \tag{2.27}$$

where S is the sensors Seebeck coefficient and ΔV_{cell} is the voltage drop between the cell plates. This instrument is then calibrated using reference samples of which the specific heat can be found in literature. The most common are: copper, molibdenum and sapphire. Since the specific heat of copper can vary slightly depending on its purity the use of sapphire single crystal is typically preferred.

This technique requires simple measurement preparation and it directly gives,

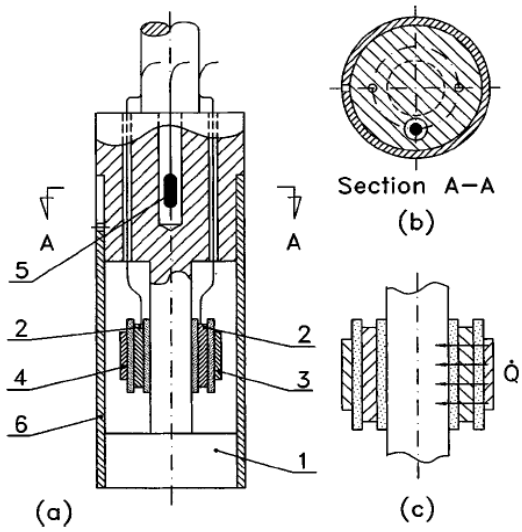

Figure 2.11: In-field Peltier cells differential scanning calorimeter. A) and B) Side and top view of the calorimeter. C) It is shown the heat flux from sample to calorimeter (esothermic process).[71]

after integration of in field specific heat curves, both Δs_T and ΔT_{ad} values. The MCE measured by these setups are characterized by large errors. These instruments are however probably more difficult to be realized if compared to adiabatic probes. The main problems are linked with the temperature sweep regulation and with the precise control of the heat flowing to and from the sample.

Isothermal calorimetry

A few examples are reported in literature of isothermal calorimeters based on the use of thermoelectric devices as heat flow sensors.[75, 74] Together with adiabatic calorimetry this is a further direct method for characterizing the MCE. The isothermal entropy change is measured directly detecting the heat flown between sample and calorimeter induced by the varying magnetic field. The instrument calibration can be performed as for DSC, then the heat exchanged is deduced by integration of the heat flow.

CHAPTER 3

Experimental work

3.1 Magnetometry

3.1.1 Measurement protocol - inverse MCE

Ni-Mn-Ga based Heuslers show inverse MCE at the martensitic transformation when a partial substitution of Ni with Co is performed. High Mn contents contribute to lower the martensite magnetic interactions while enhance the austenitic ones.[47, 48] This effect contributes to increase the saturation magnetization difference between the two phases, thus promoting larger transformation temperature shifts in applied magnetic field ($^{\Delta T_M}/_{\mu_0 \Delta H}$). This parameter is the most important key feature to discriminate processes characterized by large ΔT_{ad} as already described.[7]

An estimation of this quantity can be obtained measuring the temperature dependent magnetization of the material at different applied fields. Isofield magnetization curves at $\mu_0 H = 0 - 2 - 5$T applied fields were measured for a $Ni_{45}Co_5Mn_{30}Ga_{20}$ alloy ($m = 12.8 \pm 0.1$mg) in the temperature range 200K 400K. These M(T) curves reported in figure 3.1 were performed sweeping the cryostat temperature at $0.067 Ks^{-1}$. This material was chosen as a model sys-

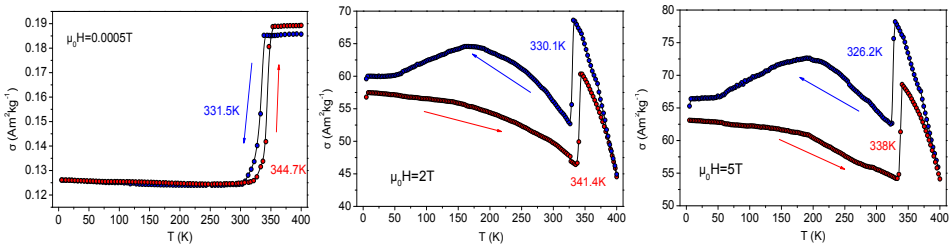

Figure 3.1: Magnetization isofield curves measured heating and cooling the sample between 5K and 400K. The applied fields are $\mu_0 H = 0.0005T$, $\mu_0 H = 2T$, $\mu_0 H = 5T$.

tem since it is characterized by a sharp martensitic transformation near room temperature (see fig. 2.8). Magnetization phase diagrams highlight the magneto-structural martensitic transformation for every applied field (see figure 3.1). This process, occurring in zero field between 330K and 340K, is the main phase change from 5K to 400K. It is characterized by a hysteresis of about 10K which seems not to show a magnetic field dependence at least up to 5T. The temperature width of the heating and cooling transformation is about 6K. Austenite Curie transition is at 425K (see fig. 2.8) and it does not appear in figs. 3.1. The high values of saturation magnetization on both sides of the transformation testify that both austenite and martensite are ferromagnetic. The magnetic field dependence of the martensitic temperatures can be better focused collecting from M(T) curves the transformations inflection points for every field value.

From figure 3.2 the sensitivity of the magneto-structural transition temperature to the applied field ($^{\Delta T_M}/_{\mu_0 \Delta H}$) can be visualized. A mean value of about -1.2KT^{-1} is obtained both for the heating and the cooling transformation. The sign of this parameter discriminates the MCE behavior which in this case is inverse. The dotted lines drew before and after the "critical" temperatures represent the starting and the ending points of the process: here are estimated from the second order derivative peaks of M(T) curves. The phase diagram of fig. 3.2 offers moreover fruitful details which are difficult to be grasped from isofield magnetic characterization. It allows to study the effect of the magnetic field on the structural phase change and thus the system MCE. In this graph stands out in particular the hysteresis dependence on both magnetic field and temperature.

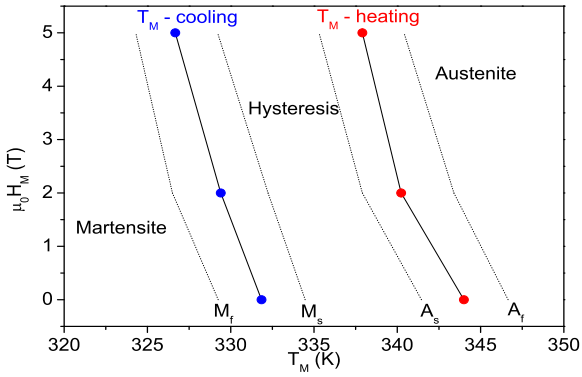

Figure 3.2: Phase diagram of $Ni_{45}Co_5Mn_{30}Ga_{20}$ alloy. Here are reported the critical fields depending on the critical temperatures.

Extrapolating the heating and cooling trends of the transformation it can be observed that the temperature hysteresis of $\sim$ 10K corresponds to a magnetic field irreversibility of $\sim$ 7.5T. Since the effect of temperature and magnetic field on the process can be considered similar if rescaled on $^{\Delta T_M}/_{\mu_0 \Delta H} \sim 1.2\mathrm{KT}^{-1}$, it is expected that $\Delta H_{hyst} = \Delta T_{hyst}{}^{\mu_0 \Delta H}/_{\Delta T_M}$. The previous formula predicts a value of 8.3T. The lower magnetic field necessary to cycle from one phase to the other is then $\sim$ 8T at $\sim$ 332K. The phase diagram of fig. 3.2 explains how the magnetic field can induce the process. The occurrence of austenite is verified if the magnetic field is turned on below the heating T_M. The reverse transformation to martensite appears if the magnetic field is removed at temperatures lower than the cooling T_M.

Magnetization isotherms were performed then around the heating transformation branch while applying the field. The sequence of M(H) curves (up to $\mu_0 H = 5$T) was then collected following two different measurement protocols to investigate the effect of hysteresis. Firstly before approaching every isotherm temperature the material was heated up to austenite (fig. 3.3 a), then the second attempt was performed taking care to cool the material down to martensite before stabilizing the following isotherm temperature (fig. 3.3 b). In figure 3.3 a, the induced $M \rightarrow A$ transformation occurs for T=336K at $\mu_0 H \sim 4.5$T and for T=338K at $\mu_0 H \sim 3$T. The dependence of the martensitic critical field on

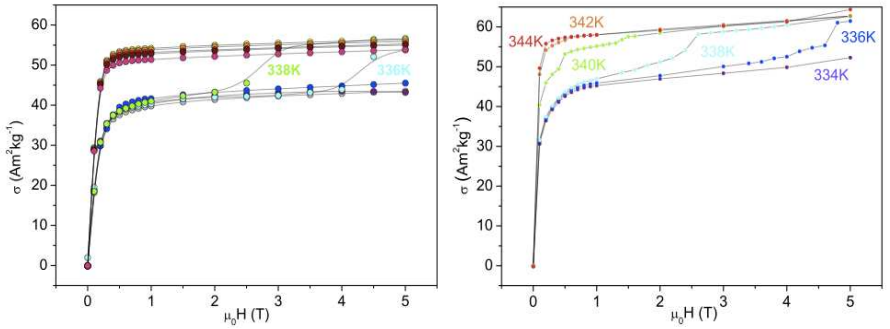

Figure 3.3: Magnetization isothermal curves measured up to $\mu_0 H = 5T$. Before stabilizing every isotherm temperature the system was heated up to austenite in sequence a) and cooled down to martensite in sequence b).

temperature turns out to be $\mu_0 \Delta H / \Delta T_M \sim 0.75 \mathrm{TK}^{-1}$: in reasonable agreement with M(T) curves. It is expected however both from $\mu_0 \Delta H / \Delta T_M \sim 0.75 \mathrm{TK}^{-1}$ and H_M vs. T_M diagram (fig. 3.2) one more field induced transformation for T=340K at $\sim$ 1T which in this set of measurements is lacking. From figure 3.2 it is clear that however coming down in zero field from austenite at 340K the system is not able to transform to martensite, thus this process does not appear on T=340K curve. This measurement sequence is not suitable to correctly reproduce the system behavior. Following the same deduction however it seemed also strange to observe the induced transformations at T=338K and T=336K.

In the second measurement protocol the same sequence of isotherms was repeated (fig. 3.3 b) paying attention to coherently reset the state before every magnetization curve,[10] this has been fully described in Refs. [50, 55]. In this second case the measurement points where increased and the expected field induced transformations appear at T=336K, T=338K, T=340K and again $\mu_0 \Delta H / \Delta T_M \sim 0.75 \mathrm{TK}^{-1}$. M(T) curves on the heating martensitic branch were then repeated stabilizing the system temperature before each measurement to avoid any ghost widening of the hysteresis due to a too high temperature sweep rate. (fig. 3.4 a). The good agreement of the last performed M(T) and M(H) curves is evident in figure 3.4 b), which reports the critical fields deduced from isothermal curves. These two measurement protocols are consistent and well describe the heating martensitic process in the case of inverse MCE.

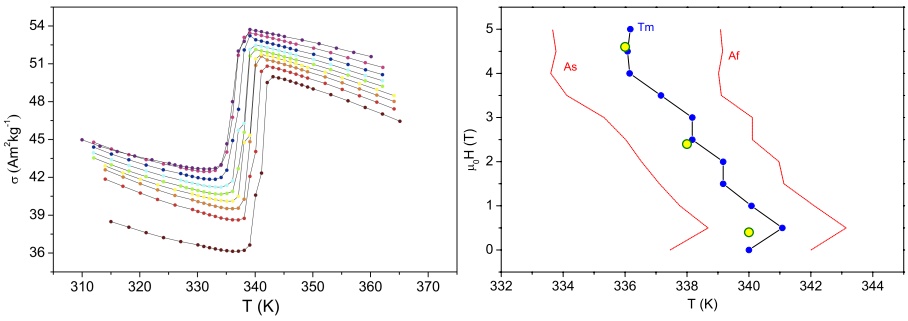

Figure 3.4: Figure a): Magnetization isofield curves up to $\mu_0 H = 5T$ between 315K and 330K. Figure b): Here is superimposed the behavior of the heating martensitic critical fields vs. temperature. These data come from M(H) of fig. 3.3 b (yellow points) and M(T) of fig. 3.4 a (blue points).

These issues are linked with irreversible effects peculiar of magnetic transitions involving a structural phase change. Generally second order processes do not show hysteresis and the MCE is always reversible. In such cases the previous attentions are not required.

Enhanced temperature control

The previous magnetic characterization left however some unclear aspects. The martensitic transformations of the materials studied are more sensible to temperature than to magnetic field (the effect of a field variation of 1T on the free energy minima can be obtained changing the system temperature by only a few degrees). This means that while performing magnetization isotherms, (it can be seen as an example the $Ni_{45}Co_5Mn_{30}Ga_{20}$ alloy shown before) it is useless to perform field steps narrower than 0.05T if the cryostat temperature control does not allow a temperature resolution better than 0.06K. If oscillating magnetic fields could drive the system into irreversible states, more deleterious can be a temperature instability. The magnetic measurements have been performed by using a SQuID MPMSXL5 Quantum Design magnetometer equipped with Enhanced thermometry and temperature sweep mode. In order to verify the temperature profile of the sample space in operative conditions a Cernox temperature sensor

was put in the sample position. In figure 3.5 two examples are reported.

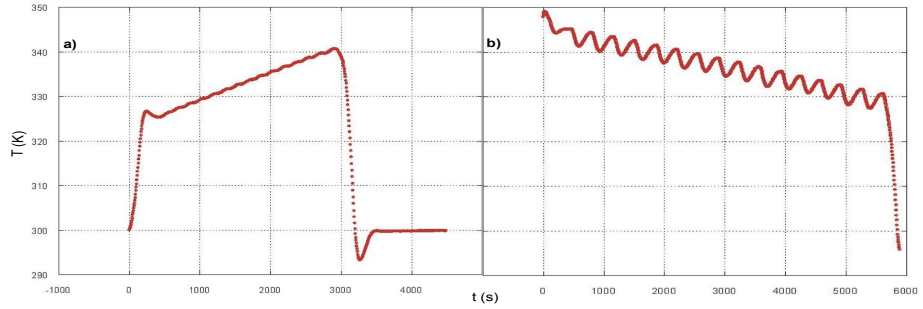

Figure 3.5: Sample space temperature measurement during a heating sequence (panel a) and a cooling sequence (panel b)

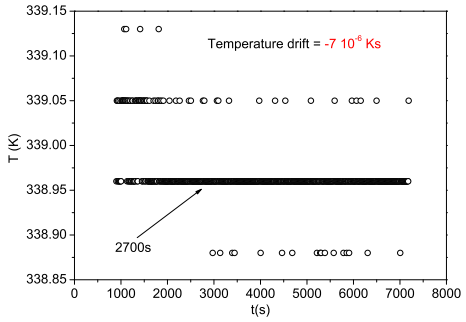

Figure 3.6: default

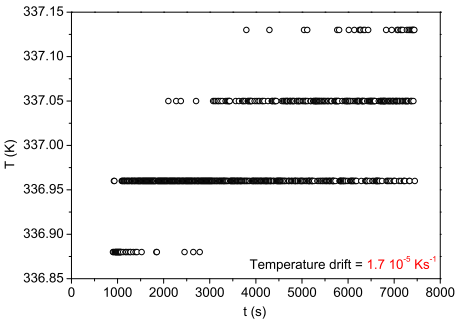

Figure 3.7: default

Both the sequences set the system temperature at intervals of 1K with a temperature sweep of $\sim 0.017 \mathrm{Ks}^{-1}$: panel a) represents a heating path from 328K to 340K, while panel b) shows the case of a cooling settle mode measurement from 350K to 330K. It is evident a difference between the two examples. Pronounced thermal undershoots appear before stabilizing a temperature coming down from a higher initial one. On the other hand approaching a set temperature from below does not show similar problems. Analyzing figure 3.5 b) the thermal undershoots occurring in the sample space are of about 5K. This issue however justifies the presence of the martensitic field induced transformation on the isotherms at T=336K and T=338K in the experiment reported in fig. 3.3 a).

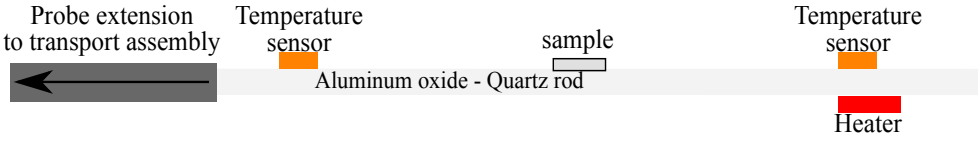

Figure 3.8: Qualitative sketch of a purpose built magnetization probe

In that case after coming down from high temperature the thermal undershoots allowed the system to transform back to martensite before starting the magnetization isotherm. At T=340K the phase change does not appear because the thermal undershoots are not sufficient to cross the cooling martensitic branch. Such problem could heavily affect the cooling M(H) characterization, which, for inverse MCE materials, has to be performed turning off the magnetic field after cooling the system from austenite down to the desired isotherm temperature.

In figure 3.6 and 3.7 two examples are shown of the time dependent cryostat temperature corresponding to two different stating states. The sample space temperature is continuously acquired for about two hours which is the time necessary to complete a magnetization isotherm. In panel a) the cryostat temperature becomes stable after $\sim$ 45 minutes. In panel b) it is reported a case where a constant slight temperature drift occurs during the measurement ($^{dT}/_{dt} \sim 1.710^{-5}$ Ks^{-1}).

These extrinsic effects can lead to incorrect estimations of the MCE of the materials studied. For this reason both M(T) and M(H) curves are necessary to understand the nature of the studied process and in particular care has to be taken when measuring the cooling branch of the first order process.

To solve the above described problem a possible way is the accurate tuning of the control parameters of the cryostat, but this could be in some cases a very tricky task. A convenient alternative way to reduce these effects is the realization of an ad hoc measurement probe. In figure 3.8 the sketch of a similar simple idea is proposed. A quartz sample holder is chosen for his low magnetic moment and high thermal conductivity. In the lower part (right side of the picture) a heater is added to stabilize the probe temperature. Two sensors, put at the two ends of the quartz rod should measure the system temperature, thus controlling the heater power.

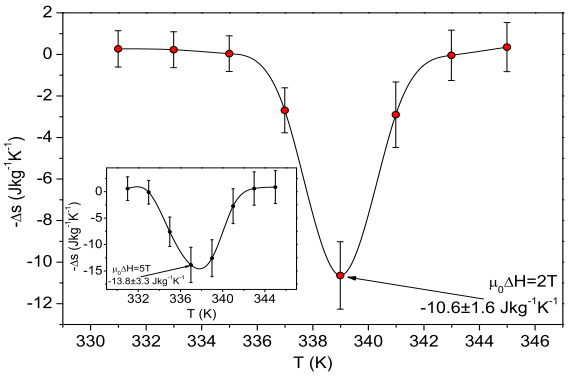

Figure 3.9: Isothermal entropy change induced by a $\mu_0\Delta H = 2$T magnetic field. In inset is shown the entropy change induced by a 5T magnetic field span.

3.1.2 Clausius - Clapeyron vs. Maxwell

The isothermal entropy change on heating corresponding to a magnetic field span $\mu_0\Delta H = 2$T obtained from Maxwell elaboration of M(H) curves is reported in figure 3.9. Before every isotherm the system was cooled down to martensite. The Δs_T peak value is about 10.6 Jkg^{-1}K^{-1} while the width of the peak at half height is about 3K in agreement with the transformation shift induced by magnetic field. The maximum Δs_T value calculated from the M(H) curves collected without using the proper measurement protocol resulted $\sim 30\%$ higher than this one.

The estimation of the entropy change from Clausius-Clapeyron relation results to be $\sim$ 12.5Jkg^{-1}K^{-1}. This value is slightly higher than that deduced by means of the trapezoidal elaboration method performed on M(H) curves. $\Delta M_s \sim 15$Am^{2}kg^{-1} and $\mu_0\Delta H/\Delta T_M \sim 0.9$TK^{-1} values which appear in Clausius Clapeyron relation can be deduced both from M(H) and M(T) curves. Clausius-Clapeyron relation applies to ideal first order processes and allows to estimate the entropy change of the fully field induced transformation. Comparing the values of the two different approaches it appears that in this case a magnetic field of 2T in not sufficient to fully induce the martensitic transformation. The entropy change for a field span of 5T results to be about 13.8Jkg^{-1}K^{-1} in agreement with the result obtained by means of the Clausius-Clapeyron relation within the experimental errors. Higher applied fields then don't increase the entropy change

peak value but contribute to widen the Δs_T curve (inset of fig. 3.9)

3.2 Adiabatic thermal characterization setup

The importance to perform direct adiabatic temperature change measurements in order to properly study the MCE has been often remarked.[13, 17] The search for innovative materials characterized by large MCE has been mainly focused on the development of systems showing magnetic transitions with high isothermal entropy variations Δs_T. This quantity, which is perhaps the more frequently deduced and cited among the parameters characterizing the MCE, it is however not sufficient to fully describe the magnetothermal behavior of a material. The adiabatic temperature change (ΔT_{ad}) is of equal importance because it represents the capability of the system to absorb or reject heat. In order to realize a magnetic refrigerator both high values of ΔT_{ad} and Δs_T are important. However the measurement of the direct temperature change requires ad hoc experimental setups and this is the main reason for which this kind of data often lacks in literature. Therefore the need of measuring this quantity and the necessity to compare it with indirect magnetic measurements and literature data has prompted us to develop an adiabatic temperature change probe in magnetic field: this was the first main experimental technique realized.

The measurement set up is made up of two parts: a multipurpose probe and the sample holder where the sensor is mounted. The idea to build a multipurpose probe able to fit several different cryostats comes from the necessity to reduce the number of connectors, cables and to simplify the procedure of sample replacement, with the same aim of similar adopted solutions.[76] We have proposed a probe equipped with 10 wires and with a vacuum chamber able to work down to 10^{-4}mbar. The wires in the probe have been carefully winded to reduce as much as possible any inductive effect due to the external varying field. The body of the probe (125mm length) is made of brass (external diameter 3mm) while on the top a purpose designed joint has the role to decouple the electric connector (10 pins Fischer DBEU model) from the pumping system (Fig. 3.10). At the bottom a screw allows to connect the vacuum chamber (external diameter 7mm)

Figure 3.10: (Color online) Multipurpose user probe: a) Upper vacuum feedtrough, b) Lower connector and vacuum chamber, c) DN40 cryostat flange feedthrough

to the probe. An epoxy resin for low temperatures fixes the lower connector (a 7 pin Fischer) to the probe (Fig. 3.10 b). In this case just 6 pins of the connector are used for convenience while the remaining 4 wires (helpful for example to verify the calibration of sample holder sensor) come out from the holes where the vacuum in the chamber is performed. This probe turns out then to be versatile for future developments of further experimental setups such as: electrical and thermal transport characterizations and calorimetry techniques. The magnetic background of this multipurpose probe, if used for magnetic measurements in SQuID magnetometer, perhaps also in different applied electric fields, should however be verified. The copper wires and the brass body of this probe prevent in MPMS cryostat to reach temperatures lower than 70K. A similar set up for lower temperatures should be fully made (both body and wires) of steel with low magnetic moment (AISI316L).

The heart of this set up is constituted by the sensor thermoresistance and sample housing. The temperature sensor is a Cernox^{TM} bare chip characterized by a mass of 3mg with 0.135s response time.[77] The Cernox^{TM} magnetoresistance is negligibly small above 30K.[78] It is fixed with an epoxy resin on a fiberglass board equipped with gold traces. The 4 wire contact is made through thermocompression bonding directly on the bare chip (fig. 3.11 b). The thermal contact with the sample is made on the back side of the Cernox^{TM} (Fig 3.11 a) through a ther-

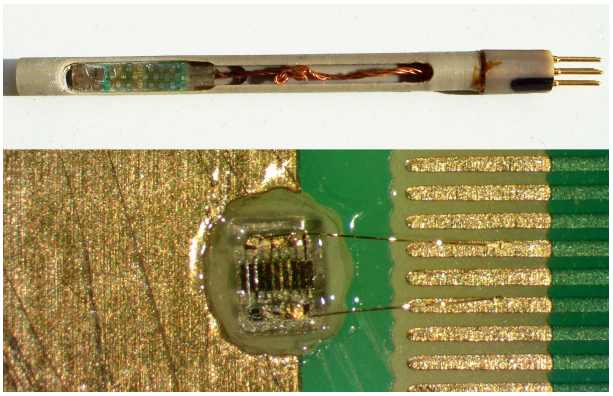

Figure 3.11: (Color online) a) ΔT_{ad} probe, b) Cernox^{TM} bare chip glued on the supporting plate.

moconductive paste (Arctic Ceramique $k = 7\mathrm{Wm}^{-1}\mathrm{K}^{-1}$). The fiberglass board is stuck in a PEEK housing (see upper part of fig. 3.11), while the sensor chip is put downwards to avoid mechanical stresses on it and on the connecting wires: any contact between the Cernox^{TM} chip and the PEEK housing is prevented. The external diameter of the sample holder is 4.5mm and the samples maximum size is 2x3x5mm. The sample is then glued in two points with GE-Varnish on the fiberglass to minimize heat losses with the probe. The resistance measurement is then performed filtering with a lock-in amplifier the voltage signal of Cernox^{TM} chip powered with an ac current of a few mA at 1kHz. The magnetic field source is a low inductive electromagnet whose sweep rate is reported in Fig. 3.12. The maximum appleid field $\mu_0 H = 1.92 \pm 0.05\mathrm{T}$ was measured with a Lakeshore 460 3-channel Hall effect gaussmeter. It can be seen from Fig. 3.12 that the magnetic field reaches 95% of its maximum value in $\sim$ 1s, while the effective field rate of this technique turns out to be $1.8\mathrm{Ts}^{-1}$.

In figure 3.13 is shown an example of a direct MCE measurement across the inverse martensitic transformation of a $Ni_{43}Co_7Mn_{30}Ga_{20}$ Heusler. The external field was in this case turned on from 0T up to 1.8T: the inverse magnetocaloric effect for such process induces a cooling of the material of $-1.25 \pm 0.15\mathrm{K}$. A detailed description of such technique will be reported after the next section.

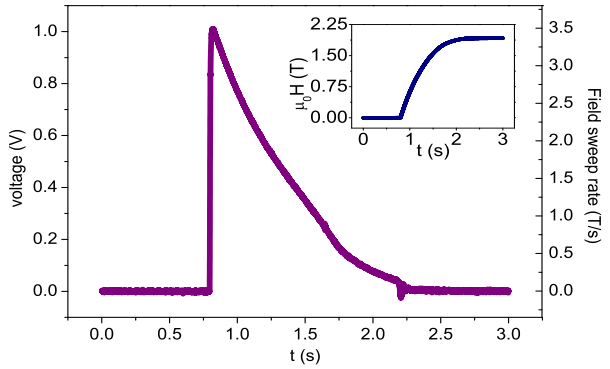

Figure 3.12: (Color online) Search coil voltage variation while the field is switched on, the right y axis scale reports the effective field sweep rate. Inset: time dependence of the effective external magnetic field in the sample region during the sweep.

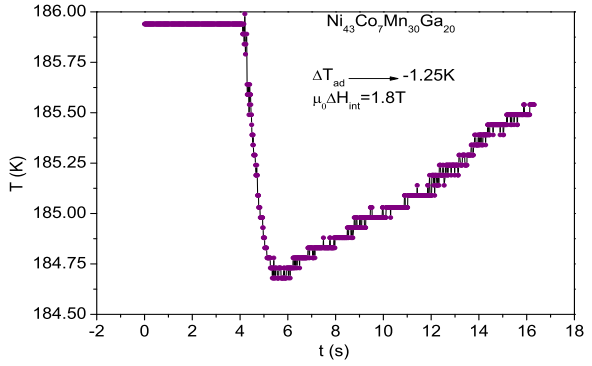

Figure 3.13: (Color online) Direct ΔT_{ad} measurement on a sample of $Ni_{43}Co_7Mn_{30}Ga_{20}$.

3.3 In-field magnetic Differential Scanning Calorimetry (DSC)

The realization of a Differential Scanning Calorimeter able to work in magnetic field was the second realized main experimental setup. As previously introduced the measurement of specific heat as a function of both temperature and magnetic field allows the calculation of the entropy phase diagram also depending on temperature and magnetic field. The power of this technique is its ability to put in relation the results of magnetic characterization and adiabatic calorimetry. DSC has offered interesting insights about the reliability of the previous two described techniques, giving informations about irreversible effects across first order processes. Moreover an analysis of the errors has pointed out which is the most reliable technique for the estimation of the two main MCE quantities (ΔT_{ad}, Δs_T). The measurement of the in-field specific heat has been also utilized to verify the possibility of deducing adiabatic temperature changes from isothermal entropy variations (see chapter 4).

The used DSC heat flow sensors are Peltier elements. The idea to exploit this technology was firstly proposed by Plackovski,[70] then other works confirmed the good reliability of thermoelectric elements as sensors for calorimetry.[71, 72, 74, 73, 75] Peltier elements are cheap devices, highly sensitive and their response is quite independent of the magnetic fields: these features favored their wide spread for the realization of in field calorimeters. Peltier DSC techniques use two identical sensors connected differentially to subtract the high background due mostly to the upper face of the sensor which is in contact with the sample. This operating mode enhances the instrument accuracy. As introduced in section 2.3.2, while the Peltier cells DSC is sweeping in temperature the heat flux between calorimeter and sample, thus flowing also through the sensor is:

$$\dot{Q} = \frac{K_{cell}}{S}\Delta V_{cell} = A\Delta V_{cell} \tag{3.1}$$

with K_{cell}, ΔV_{cell} and S being respectively the thermal conductance, the voltage drop and the Seebeck coefficient of the sensors. The calibration of the in-

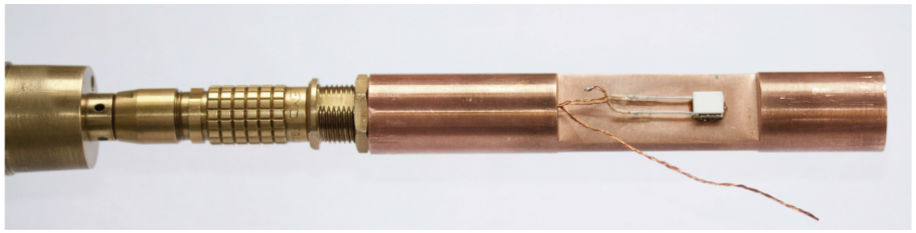

Figure 3.14: First DSC setup for CF1200 He-flow cryostat.

strument is $A(\mathrm{WV}^{-1})$. If the instrument sensitivity is known the specific heat of a sample ($c_{p-sample}$) with mass m_{sample} and depending on a $^{dT}/_{dt}$ temperature sweep becomes:

$$c_{p-sample} = \dot{Q}\left(\frac{dT}{dt}\right)^{-1} m_{sample}^{-1} = AV_{cell}\left(\frac{dT}{dt}\right)^{-1} m_{sample}^{-1} \tag{3.2}$$

The calibration of A depending on temperature can be performed in two different ways.[74] It can be measured the temperature dependent voltage drop of a material whose specific heat is well known as a function of the temperature sweep rate, then the instrument sensitivity is deduced from the previous equation. A different method involves the acquisition of the cell voltage signal by inducing a heat flow with a calibrated resistance ($\dot{Q} = RI^2$) at different temperatures.

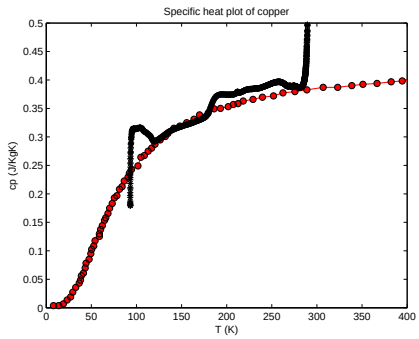

Figure 3.15: Copper specific heat curve (black) by DSC setup of figure 3.14 (no heater).
The red circles are literature data.

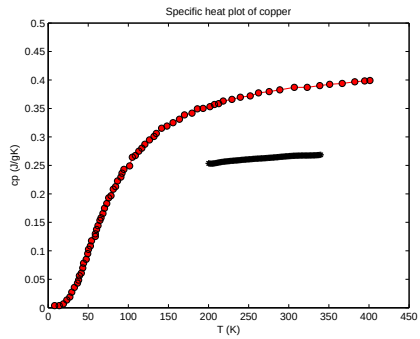

Figure 3.16: Copper specific heat curve (black) by DSC setup of figure 3.14 after adding the heater. The red circles are literature data.

In the following it will be briefly summarized the path which brought to the development of the final DSC setup. The data acquisition and temperature control of every setup has been performed exploiting a software routine based on Oxford Instruments Objectbench environment.

Figure 3.14 reports the very first attempt inspired by the work of Marcos.[71] This instrument, whose body was fully made of copper, was put inside a Oxford Instruments CF1200 He-flux cryostat able to work between 2K and 320K in magnetic fields up to 1.85T. The temperature sweep of this calorimeter, which worked in vacuum of 10^{-2}mbar, was not independently controlled. The calorimeter effective temperature followed passively the ramp of the cryostat. The effective sweep rate was then not constant. This setup was improved adding a heater on one side of the probe right alongside the Peltier cells. This allowed to extend the temperature range up to 380K and to perform linear time dependent DSC temperature profiles. Figures 3.15 and 3.16 show examples of specific heat measurements of copper in the two cases. In the very first attempts (see fig. 3.15) the DSC fits literature data just in a narrow range were its temperature sweep was almost constant. After the "upgrade" it can be noticed an improvement of the shape of the specific heat curve while its absolute value turns out to be $\sim 30\%$ lower than that expected. Since it seemed impossible to lower that discrepancy the calorimeter geometry was completely changed. The origin of the instrument malfunctioning could be the following: i) the calorimeter is not nearly-adiabatic thus the sample exchanges heat with the surroundings and not just through the sensor, and ii) the calorimeter thermal field is asymmetric. This means that slightly different experimental details (vacuum conditions in the chamber and cryostat flux of helium outside the chamber) could affect the heat flow in the calorimeter from the heater up through the supporting shaft. The lower plates of the cells (in contact with the calorimeter) would then be at different temperature every time.

The new shape was then inspired by two setups proposed in literature, in which the temperature control is performed by one more power Peltier element (a sketch in fig. 3.17).[73, 74] The new instrument (Fig. 3.19) used a 40W Peltier cell controlled by a maximum current of 4A. The temperature ramp was driven by an Oxford Instruments ITC503 temperature controller with a resolution of ± 0.01K. The ITC output voltage was then converted to current by a Kepco 50 bipolar operational power supply/amplifier. This calorimeter works in vacuum of

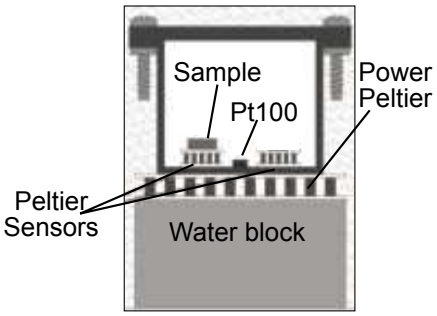

Figure 3.17: Sketch of the power Peltier controlled DSC.

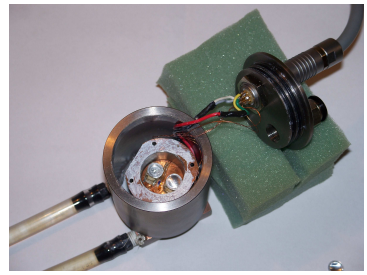

Figure 3.18: DSC top view. Outside is the vacuum chamber, at the bottom the water block.

10^{-5}mbar between 250K and 400K in magnetic fields up to 1.85T. Its external diameter is 5cm to fit the pole gap of the electromagnet. The base of the vacuum chamber is made of copper to enhance the thermal exchange with the water block. Two aluminum crucibles are put on the Peltier sensors as radiation shields. The calibration, which is repeated before every measurement, is typically performed by means of a sapphire single crystal. In figure 3.19 and 3.20 two tests are reported performed on samples of copper and across the solid-liquid phase change of gallium: the enthalpy jump integrated from fig. 3.20 results $\sim 79520 \mathrm{Jkg}^{-1}$, the difference is within 1% with respect to literature data.

The absolute error on the specific heat measured with this instrument was estimated to be within 3%. It was deduced plotting together all the measured sapphire specific heat curves (see figure 3.21). The spikes near 300K and 350K are due to imperfects (locally non linear) temperature sweeps. The curves reported in figure 3.21 are collected with two different power Peltier cells. Accurate specific heat measurements are obtained using Apiezon grease to enhance thermal contact between sample and sensors. Its contribution can be subtracted with a background measurement. A GE-varnish glue is used to fasten the sample in case of magnetocaloric characterization. Its effect is not taken into account. Due to the fact that the contribution to the heat flux of GE-varnish is constant at different magnetic fields thus it does not affect the MCE values.[51]

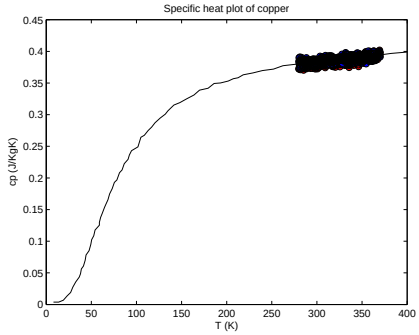

Figure 3.19: Copper specific heat data in heating and cooling by DSC setup of figure 3.19. The black line are literature data.

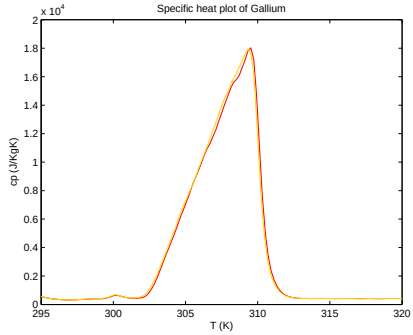

Figure 3.20: Gallium specific heat curve across its solid-liquid phase change for $\mu_0 H = 0$T (red) and 1.8T (yellow).

A detailed analysis of the errors was performed following the treatment reported in references [51, 58]. The propagation of a 3% relative uncertainty on specific heat leads to errors of about 200% on the calculated MCE: this is clearly inconsistent. However the 3% refers to the absolute value of specific heat while performing the measurement with Apiezon grease, while to fasten the sample in magnetic field a GE-varnish is used. The MCE is the magnetic field induced perturbation of the state of the system: as pointed out in ref. [51] the main source of error on the MCE is due to extrinsic effects that at the same time can slightly modify the experiment conditions then contributing to distort the action of the field.

It was verified that the oscillations in the raw specific heat curves behave as white noise and thus they do not contribute to the effective MCE error. This issue was demonstrated by smoothing the martensite $c_p(T)$ with a polynomial (as shown in figure 3.23) and then comparing the entropy curves integrated from raw and from smoothed $c_p(T)$ curves: figure 3.22 reports their relative discrepancy. It can be noticed that in few kelvin the oscillations decrease and the difference between the two curves tends to zero.

The main uncertainty in our case comes from two different effects: slightly different vacuum conditions and the progressive drying up of the GE-varnish during the measurements. To discriminate these contributions a serie of scans performed

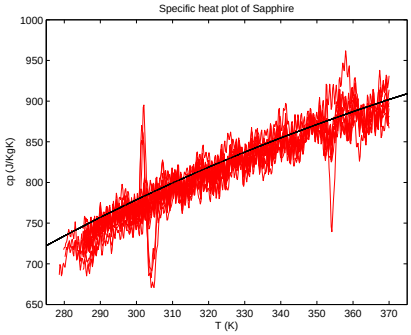

Figure 3.21: Sapphire specific heat absolute error. The red lines constitute 17 different measurements.

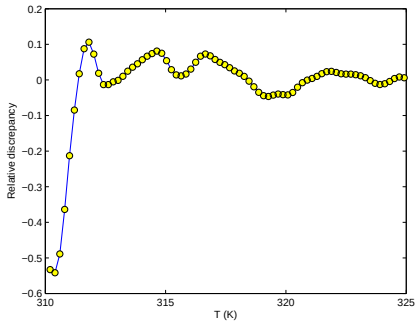

Figure 3.22: Relative difference between integration of raw c_p and smoothed c_p curves.

in sequence was compared (see fig. 3.23). The graph reports four subsequent measurements of specific heat on the same sample (in this case a $Ni_{45}Co_5Mn_{31}Ga_{19}$ alloy): both raw and smoothed data are plotted for every measurement. The magenta points correspond to the first measurements while the last scan is drawn in black. The coherent growth of the specific heat baseline is a clue that the hypothesis made before is correct. In particular, keeping on pumping for longer times, the system nearly-adiabaticity improves and more heat is exchanged through the Peltier sensors thus the signal grows.

The relative difference, not due to the action of any applied field, between the repeated c_p curves is reported in figure 3.24. The relative difference between the last curve and the first (red circles), the second (green circles) and the third one (blue circles) is shown. The relative difference between the third and the forth curves lies within 0.3%. Other experiments like this demonstrated that comparing different curves after the second one the effective error lies always within 0.6%. The instrument accuracy can be chosen depending on the effect that is to be measured. In case of low MCE materials it could be required to perform a high number of scans to reduce the relative error and then their MCE absolute error.

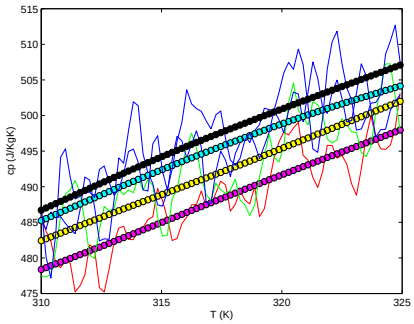

Figure 3.23: Sequence of c_p curves in the *Ni-Co-Mn-Ga* martensitic region in zero applied field. Are reported both the raw and the smoothed data. The specific heat baseline grows while repeating the measurement.

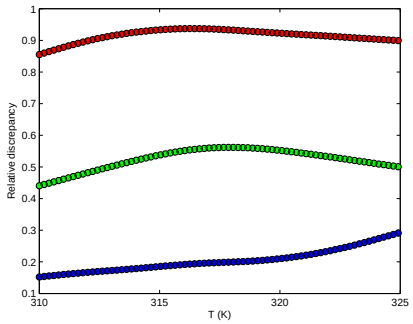

Figure 3.24: Relative difference between the last performed c_p curve (black curve of fig.3.23) and the first (red points), the second (green points) and the third one (blue points). The effective relative error lowers comparing repeated scans.

3.4 General discussion on adiabatic magnetic thermal characterization

The direct MCE measurements shown in the following are compared with the results of in-field differential scanning calorimetry described in the previous section performed on the same sample. The in-field DSC characterization for gadolinium has been performed with a sweep rate of $0.03\mathrm{Ks}^{-1}$ in (internal) magnetic fields of $\mu_0 H_f = 0\mathrm{T}$ and $\mu_0 H_f = 1.7\mathrm{T}$, while its effective relative error was reduced within 0.6%.

The magnetic fields reported in the following are all internal ones. The whole discussion on the capabilities of this experimental setup will be described showing the full ΔT_{ad} characterization of a sample of gadolinium, which is generally used as a standard material while realizing experimental setups to study the MCE.

The Cernox$^{\mathrm{TM}}$ bare chip of the in field adiabatic calorimeter is almost entirely made up of sapphire.[77] Its mass ($m_{Cx} \sim 3\mathrm{mg}$) corresponds to a room temperature heat capacity of $\sim 0.0024\mathrm{J/K}$, which is comparable to a gadolinium sample of $\sim 8\mathrm{mg}$ (it was considered $c_{pGd} \sim 300\mathrm{Jkg^{-1}K^{-1}}$). This effect is system-

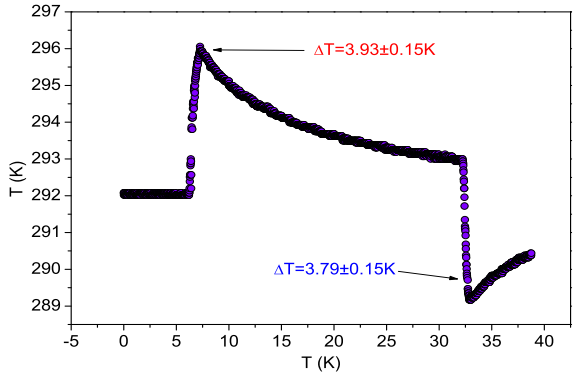

Figure 3.25: (Color online) Direct ΔT_{ad} measurement across the Gadolinium Curie temperature. It is shown both the effect due to a magnetic field increase and decrease ($\mu_0 \Delta H \sim 1.65$T).

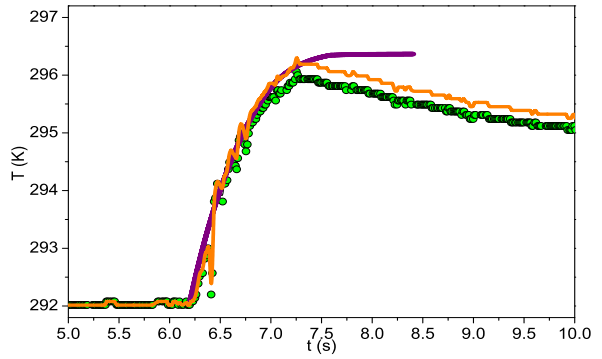

Figure 3.26: (Color online) Enlarged view of the magnetization branch of fig. 3.25. Here are superimposed on the raw data (green dots) the magnetic field sweep from inset of fig. 3.12 (violet line) normalized on the maximum expected ΔT_{ad} and the temperature profile obtained taking into account the sensor heat capacity (orange line).

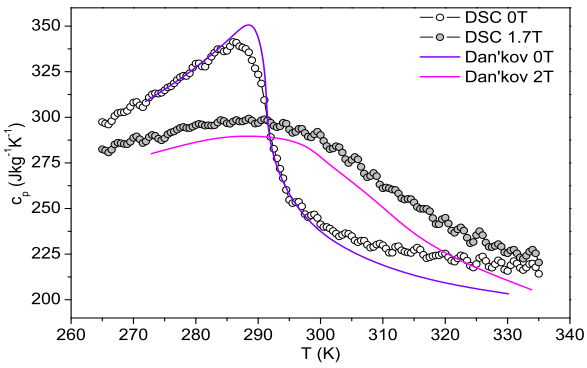

Figure 3.27: (Color online) Specific heat curves at internal fields $\mu_0 H = 0.17$T and $\mu_0 H = 1.35$T compared with data from Ref. [16]

atic so it can be taken into account if the specific heat of the measured material is known. The Gadolinium sample measured in the following is chosen large enough ($\sim$ 110mg) to almost neglect the sensor contribution. The heat capacity balance between sample and sensor can be expressed through a simple proportion that allows to estimate the entity of this effect:

$$\Delta T_{ad_{Gd}}(T) = \Delta T_{ad_{Cx}}(T) \frac{m_{Cx} c_{pCx}(T) + m_{Gd} c_{pGd}(T)}{m_{Gd} c_{pGd}(T)} \tag{3.3}$$

where $\Delta T_{ad_{Gd}}(T)$ and $\Delta T_{ad_{Cx}}(T)$ are the effective adiabatic temperature changes of the sample and of the sensor, while the Cernox$^{\text{TM}}$ specific heat is $c_{pCx}(T)$ and the Gadolinium mass is m_{Gd}. This equation allows then to correct the measured ΔT_{ad} values in case of low heat capacity systems. In order to rescale the observed ΔT_{ad} the shown proportion is applied in the adiabatic measurement branch: that is, when the magnetic field is turned on. The considered Gadolinium specific heat value $c_{pGd}(T)$ is an average between the in-field and the zero field specific heat curves which were directly measured with the in-field differential scanning calorimeter (DSC) (see figure 3.27).

The magnetocaloric adiabatic behavior of a polycrystal sample of gadolinium of $\sim$ 110mg in $\mu_0 \Delta H \sim 1.65$T is shown in fig. 3.25. In this graph the heating

and cooling regions, where the magnetic field is turned on and off are clearly detectable. The measurement error (± 0.15K) is due to the sensor electric noise and corresponds to a resistance resolution of $\pm 0.01\Omega$. Quantitatively the temperature sensor chip from 340K to 350K spans a resistance interval from 66.43Ω to 64.94Ω, and therefore this implies $\sim 1.5\Omega$ for 10K. An error of $\pm 0.01\Omega$ corresponds then to ~ 0.07K, which is approximatively our temperature uncertainty: the error on the deduced ΔT_{ad} values is then double.

The not ideal adiabatic conditions of this setup become evident observing the relaxation of the material temperature right after the peak (see fig. 3.25): a deep discussion of this will be performed in the following. In fig. 3.26 the magnetic field profile (enlarged view of Fig. 3.25) is superimposed to the temperature data without modifying the relative time scales. In this plot the vertical axis is rescaled on the maximum expected ΔT_{ad} value for the maximum applied field. This plot shows that the sensor time response is lower than the magnetic field growth time. The shape of the temperature profile depends on the magnetic field sweep rate rather than on the not perfect adiabatic conditions. Figure 3.26 also reports the temperature data corrected with Eq. 3.3: the difference between the measured peak value and the calculated one is $\sim 6\%$. In the following the reported data will include this contribution.

The magnetic field dependence of the MCE peak value is displayed in fig. 3.28. x-axis reports the effective internal field, calculated from a demagnetizing factor $N \sim 0.3$ for the present case. It has been shown that demagnetizing fields can substantially affect the MCE, thus to compare measured data with literature their estimation is fundamental.[57, 79] The inset reports the MCE peak values as function of $\mu_0^{\frac{2}{3}} H^{\frac{2}{3}}$: the slope of this curve ($A = 3.13 \pm 0.03\mathrm{K}\mu_0^{2/3}\mathrm{T}^{2/3}$) is a further marker of the material magnetocaloric properties.[79] This dependence can be deduced from a mean field approach in correspondence of Curie transition.

The temperature dependence of gadolinium ΔT_{ad} is shown in fig. 3.29. The possible influence of eddy currents induced in the sample by magnetic field was checked comparing the "heating" and "cooling" $\Delta T_{ad}(T)$ curves as suggested in Ref. [60]. This comparison did not success in verifying eddy currents effects. The utilized Gadolinium sample was polycrystalline and its purity degree was unknown: since in rare earth elements the purity degree affects their magnetic and thermal properties in particular across Curie temperature, this issue prevents

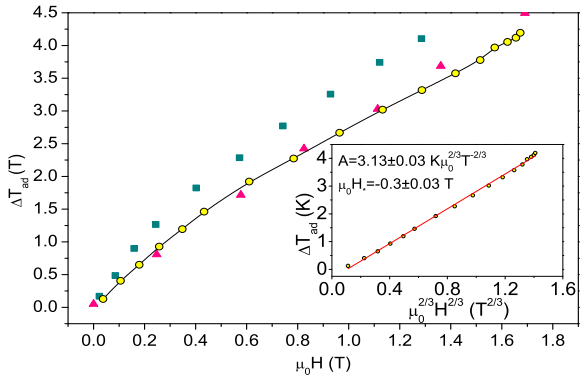

Figure 3.28: (Color online) ΔT_{ad} characterization reported vs. magnetic field in correspondence of the MCE peak value ($\sim$ 292K). Our characterization is compared with values shown in Ref. [16] (triangle symbols) and Ref. [79] (square symbols). In inset it is reported the $\mu_0^{\frac{2}{3}} H^{\frac{2}{3}}$ dependence of the ΔT_{ad}.

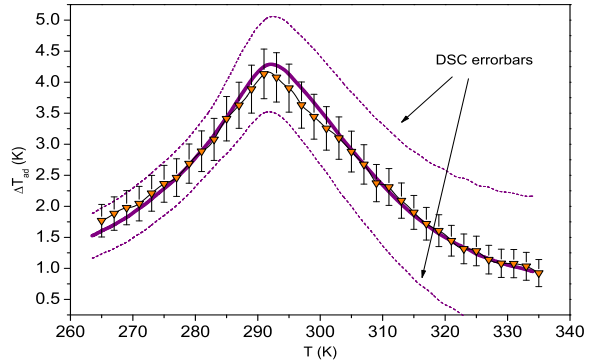

Figure 3.29: (Color online) Temperature dependence of the ΔT_{ad} directly measured in a $\mu_0 \Delta H = 1.65$T variation of the field (triangles). This measurement is compared with the in field DSC estimation performed on the same sample in a $\mu_0 \Delta H = 1.7$T applied field (purple line).

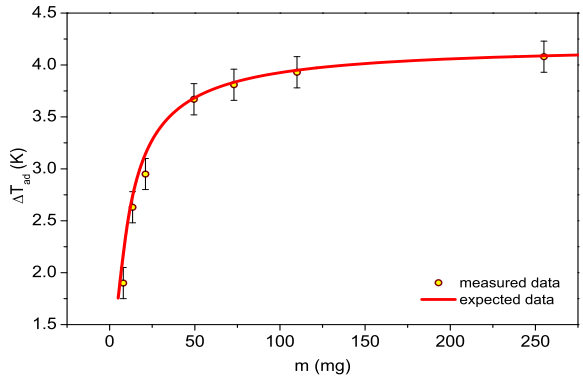

Figure 3.30: (Color online) ΔT_{ad} characterization reported vs. sample mass in correspondence of the MCE peak value ($T \sim 292$K) (circle points). The expected temperature change is relative to an internal field change of $\mu_0 \Delta H = 1.7$T and is deduced from Eq. 3.3 (red line).

a simple comparison with literature data.[16, 19] In fig. 3.29 the directly measured ΔT_{ad} values are superimposed to the MCE results obtained by a in-field DSC. The calorimetric characterization for gadolinium is performed with a sweep rate of 0.03Ks^{-1} in (internal) magnetic fields of $\mu_0 H_i \sim 0$T and $\mu_0 H_f \sim 1.7$T, while its effective relative error was reduced within 0.6%. This value is due to slightly unstable vacuum conditions which affect the specific heat baselines of the in-field and zero field temperature scans with different systematic errors.[51]. The demagnetizing field in the ΔT_{ad} measurements is estimated $\sim 0.3T$, while in the DSC analysis it is estimated $\sim 0.14T$. It can be appreciated from figure 3.29 the good agreement between the outcomes of the two techniques. Observing the MCE peaks the direct MCE probe returns $\Delta T_{ad} = 4.14 \pm 0.27$K for a magnetic field span of $\mu_0 \Delta H = 1.65$T, while from calorimetry $\Delta T_{ad} = 4.29 \pm 0.77$K is obtained for a magnetic field change of $\mu_0 \Delta H = 1.7$T. Both the errorbars include the best estimated values of the complementary technique. The uncertainty of the direct technique turns out to be much lower than that of DSC. This point is a further clue that supports the use of a purely adiabatic technique instead of isofield or isothermal ones to obtain a precise estimation of ΔT_{ad}.

If, as a working hypothesis, the sample-sensor system can be considered as adiabatic during the measurement time (within 1s from the instant when the

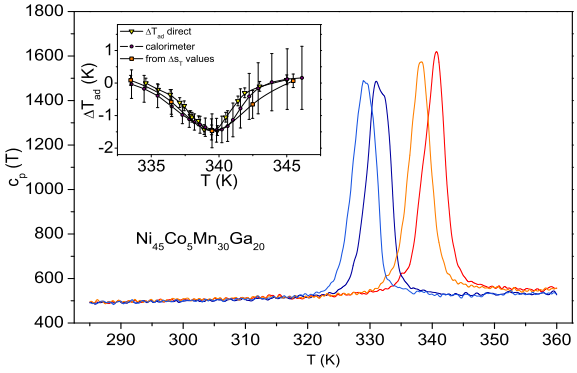

Figure 3.31: (Color online) Specific heat curves and MCE of $Ni_{45}Co_5Mn_{30}Ga_{20}$ Heusler of $\sim$ 30mg in $\mu_0\Delta H = 1.7$T. In inset is shown the matching between the expected and the directly measured adiabatic temperature change values.

magnet is turned on see fig. 3.26) a coherent dependence is expected between the measured ΔT_{ad} and the gadolinium sample mass. Equation (3.3) explains this fact taking into account the thermal balance between sample and sensor heat capacities. A ΔT_{ad} ideal line corresponding to a perfect adiabatic environment can then be traced depending on sample mass on the basis of Eq. (3.3). This analysis has been performed on the expected MCE value obtained from in-field DSC which is for every sample $\Delta T_{ad_{Gd}}(T_{max}) = 4.29 \pm 0.77$K. It was chosen as reference the calorimetric value because it should not be affected by the sample size. This analysis has been verified by directly measuring ΔT_{ad} for different sample masses. The experimental points in fig. 3.30 are then the maximum ΔT_{ad} values observed for every case. Considering the different shape of every sample the internal field spans fall within ± 0.07T. The matching between the experimental points and the expected values on the basis of Eq. (3.3) supports the hypothesis that while the magnetic field sweeps the sensor fast time response makes the system as nearly adiabatic.

This result has been verified on other samples: for example an interesting question has been to understand why on a $Ni_{45}Co_5Mn_{30}Ga_{20}$ sample of 30mg was directly measured almost the expected MCE value from DSC analysis (see inset of figure 3.31). This alloy shows a sharp martensitic transformation (section 4.1)

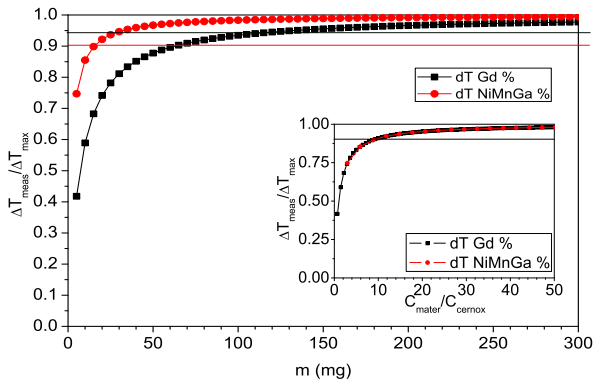

Figure 3.32: (Color online) Relative $\Delta T_{ad_{Cx}}/\Delta T_{ad_{sample}}$ for Gadolinium sample (black) and $Ni_{45}Co_5Mn_{30}Ga_{20}$ Heusler (red). The curves are calculated for the two materials assuming the setup as perfectly adiabatic during the field sweep. In inset it is reported the same curve normalized on abscissa on the sensor heat capacity. These graphs describe the sensitivity of the ΔT_{ad} probe.

characterized by a high peak of specific heat. Since the maximum MCE was observed in correspondence of this point, the sample "ideal" ΔT_{ad} curve was built up on the basis of Eq. 3.3 considering its peak specific heat. The Gadolinium and the Ni-Mn-Ga expected curves are compared in fig. 3.32 where the ΔT_{ad} values are normalized to their maximum values. It can be observed (figure 3.32) that across the first order process a ΔT_{ad} within 95% (which is a threshold that corresponds to the measurement error: ± 0.15K) of the maximum value can be measured down to a 30mg mass sample, while in the case of Gadolinium samples of mass larger than 100mg are required. This simple calculation justifies the good operation of the ΔT_{ad} probe down to small sample sizes for the MCE characterization of sharp first order transformations.

In summary the curve reported in fig. 3.30 can thus be considered as the (mass) sensitivity of the described technique in case of Gadolinium. A more general sensitivity curve is shown in fig. 3.32, here the temperature change is normalized to its maximum value and thus applies to a generic Gadolinium sample (fragments of different purity). Nevertheless the MCE of samples of lower mass can be deduced from the previously shown relation.

In figure 3.32 the instrument sensitivity curve is reported for the *Ni-Co-Mn-Ga*

Heusler alloy (red squares). In this case the full effect was measured on a sample of $\sim$ 30mg without the need of any correction (inset of fig. 3.31).

The normalized ΔT_{ad} as a function of the ratio between sample and Cernox^{TM} heat capacity is reported in the inset of fig. 3.32. This plot represents a sort of "universal" sensitivity curve, which applies to a generic sample. A similar curve has been presented in a recent work where the response of the measurement setup was tested as a function of its thermal diffusivity.[61] Though the probe presented in this work and the one of Ref. [61] behave differently, this similar result can likely be explained since different adiabatic conditions can be read as different heat capacity ratios.

CHAPTER 4

Complete Magnetocaloric characterization of first order inverse *Ni-Co-Mn-Ga* Heuslers

4.1 Magnetization vs. direct ΔT_{ad} measurements: $Ni_{45}Co_5Mn_{30}Ga_{20}$ and $Ni_{41}Co_9Mn_{32}Ga_{16}In_2$

Right after the realization of the adiabatic temperature change probe and the analysis of the magnetic measurement protocol for inverse magnetocaloric transformations, as discussed in the previous chapter, we decided to compare the results obtained by these two different characterization techniques. Two samples were chosen in the compositional phase diagram shown in section 2.2, characterized by a martensitic transformation at similar temperature but distinguished by peculiar behaviors. The most intriguing feature occurring in the phase diagram drawn in figure 2.8 is the occurrence of a paramagnetic gap for some compositions (see section 2.2). The idea was then to compare two materials representative of two different regimes: with and without the paramagnetic martensitic region before the occurrence of ferromagnetic austenite. This feature is responsible of high ΔM, ΔV and ${}^{\Delta T_M}/_{\mu_0 \Delta H}$ values at the phase change: it was shown that these properties are markers of large MCE.[23, 42, 45, 46] The most suited al-

loys to compare were then: $Ni_{45}Co_5Mn_{30}Ga_{20}$ and $Ni_{41}Co_9Mn_{32}Ga_{16}In_2$. A well defined martensitic transformation in $Ni_{45}Co_5Mn_{30}Ga_{20}$ occurs between both ferromagnetic martensite and austenite at $T_M \sim 340$K: this process exhibits a low saturation magnetization jump at the solid-solid phase change while it can be fully induced with low applied magnetic fields. Higher ΔM was reported in $Ni_{41}Co_9Mn_{32}Ga_{16}In_2$ but this system shows a temperature broadened martensitic transformation at $T_M \sim 340$K which can be totally induced only with high magnetic fields ($\mu_0 \Delta H > 5$T). This opportunity is ideal to study the effect of paramagnetic martensite on the transformation magnetothermal properties, comparing this peculiar behavior with that of a system characterized by a more common FM-FM first order process. Furthermore it was shown that these two materials are distinguished by different volume changes at the transformation:[48] ${}^{\Delta V}/_{V} \sim 0.9\%$ for $Ni_{41}Co_9Mn_{32}Ga_{16}In_2$ and ${}^{\Delta V}/_{V} \sim 0.45\%$ for $Ni_{45}Co_5Mn_{30}Ga_{20}$. The study of their MCE could be interesting also in relation with this property.

Along the discussion, just for convenience, the $Ni_{45}Co_5Mn_{30}Ga_{20}$ will be labeled *SampleA* while $Ni_{41}Co_9Mn_{32}Ga_{16}In_2$ alloy will be named *SampleB*.

Martensitic transformations are first order magneto-structural processes characterized by hysteresis. Ideal first order processes (distinguished by a step like singolarity in the material phase diagram) are described by the Clausius-Clapeyron relation: see equation 2.24 and section 2.1.1.[4, 11] Real first order processes however occur in finite temperature or magnetic field intervals being far from step-like: this means that the magnetization first order derivatives on temperature $\left(\frac{\partial M}{\partial T}\right)_H$ or magnetic field $\left(\frac{\partial M}{\mu_0 \partial H}\right)_T$ do not diverge. From the analytical point of view, the integration of isothermal or isofield curves is then allowed,[10, 14] and the use of the Maxwell relation (equation 2.10 section 2.1.1) is not forbidden. It is difficult to understand where lies the limit which discriminates the suitability of one approach instead of the other. We decided however to report both the values calculated by means of the two relations.

In order to deepen the behavior of ΔT_{ad} and the Δs_T across the martensitic first order process, a geometrical construction (Fig. 4.1) was realized. It takes into account the transformation sensitivity to the applied field (${}^{\Delta T_M}/_{\mu_0 \Delta H}$), its isothermal entropy change and the specific heat value of the martensitic phase right before the phase change ($c_{p(mart)}$) thus describing the temperature dependent entropy curves on heating with and without an applied magnetic field. The

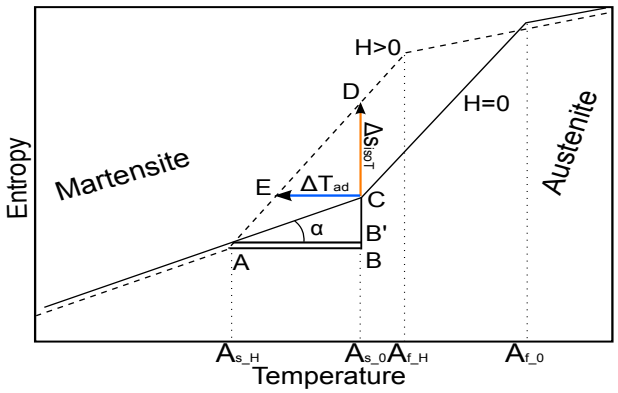

Figure 4.1: (Color online) Geometrical construction of the first order martensitic process in the s *vs.* T plane. The behavior of ΔT_{ad} peak value can be estimated from Δs_T peak values obtained from *M(H)* curves, the c_p of the martensite below the transformation region and the transformation temperature shift magnetic field induced.

study on these two materials has been purposely focused on the heating branch of the phase change process. The dummy *s(T)* curves (expressed in arbitrary units) can be constructed choosing the phase fraction as the order parameter of the process.[80] This construction makes the presented graphical model (Fig. 4.1) significant only in the transition region, where the critical temperatures marking the starting and finishing points of the transformation in the *s(T)* curves are assumed to coincide with those deduced by the magneto-thermal characterization (*M(T)* curves). This geometrical model helps to connect some features of the martensitic process, namely the ΔT_{ad} and the Δs_T peak values, with the ${}^{\Delta T_M}/_{\mu_0 \Delta H}$ and the c_p value characteristic of the martensitic phase. The diagram of Fig. 4.1 allows then to deduce a proportion between the triangles ABD and the CDE:

$$AB : \Delta T_{ad} = (\Delta s_T + CB) : \Delta s_T \tag{4.1}$$

Here, Δs_T is the entropy change peak value deduced on the basis of the Maxwell relation in a field span $\mu_0 \Delta H$=2T. AB is the temperature interval between the

transformation starting points in the two different magnetic fields: $A_s(\mu_0 H = 0\text{T}) - A_s(\mu_0 H = 2\text{T})$. This difference can be calculated from the second order derivative peaks of the *M(T)* curves corresponding to $\mu_0 H$ =0T and 2T: it should furthermore be in agreement with the transformation temperature shift induced by magnetic field: $A_s(\mu_0 H = 0\text{T}) - A_s(\mu_0 H = 2\text{T}) \approx \mu_0 \Delta H(^{\Delta T_M}/_{\mu_0 \Delta H})$. The segment CB' represents an entropy coordinate which correlates the in-field and out-of-field transformations. In particular it contributes to rescale the $^{\Delta T_M}/_{\mu_0 \Delta H}$ parameter on the specific heat value. A high specific heat of the low temperature phase (martensite in case of Heusler alloys) enhances the segment CB' and thus also for high magnetic field induced transformation shifts it depresses the ΔT_{ad} as already underlined in Ref. [81]: $CB' \sim AB \tan\alpha = (A_{s-0} - A_{s-H}) \tan\alpha$. The entropy change due to the saturation of the martensitic phase is taken into account in segment BB'.

The studied samples were prepared by arc melting and thus homogenized by annealing at $900°C$ for 72h. Magnetization measurements on *SampleA* and *SampleB* were performed respectively on masses of 12.8 ± 0.1mg and 5 ± 0.1mg, while direct adiabatic temperature changes were measured on samples of $\sim$ 120mg and $\sim$ 170mg. The ferromagnetic nature of both martensite and austenite in *SampleA* is deduced from the isofield magnetization behavior of fig. 4.2. The inset shows the magnetic susceptivity diagram between 250K and 450K: a thermal hysteresis of about 10K characterizes the martensitic transformation while the Austenitic Curie transition occurs at about 425K. In Fig. 4.3 it can be noticed the lower strength (compared to *SampleA*) of martensite magnetic interactions of *SampleB* ($Ni_{41}Co_9Mn_{32}Ga_{16}In_2$). A thermal hysteresis of $\sim$ 25K is observed across the martensite-austenite phase change (inset of 4.3). This sample shows large ΔM and $^{\Delta T_M}/_{\mu_0 \Delta H}$ values, while the martensitic transformation is broadened in temperature. The partial substitution of 2% Ga with In, while preserving the magnetic critical temperatures,[41] lowers the T_M of the parent quaternary composition $Ni_{41}Co_9Mn_{32}Ga_{18}$ from 436K to 340K on heating (from 421K to 315K on cooling).[48] Due to the increased distance between the martensitic transformation and the Curie transition, the ΔM and $^{\Delta T_M}/_{\mu_0 \Delta H}$ values (see Tab. 4.1) are further improved, when compared to the quaternary In-free composition.

The irreversible nature of the martensitic process is evident also in *M(H)* curves. The corresponding hysteresis in magnetic field has been estimated to

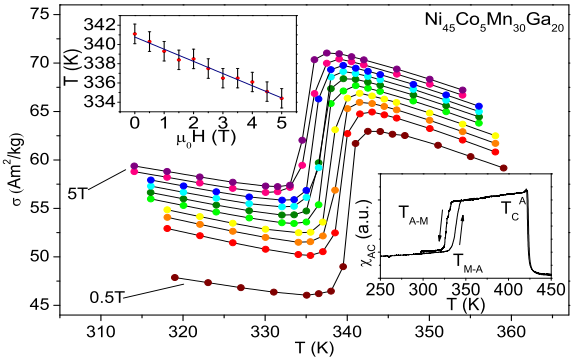

Figure 4.2: (Color online) *M(T)* isofield curves on heating of the martensitic transformation with 0.5T< $\mu_0 H$ <5T on the low ΔM alloy ($Ni_{45}Co_5Mn_{30}Ga_{20}$ - *SampleA*) (field step $\mu_0 H$=0.5T). Upper inset: T_M vs. H phase diagram deduced from isofield curves. Lower inset: a.c. susceptibility plot showing the martensitic transformation.

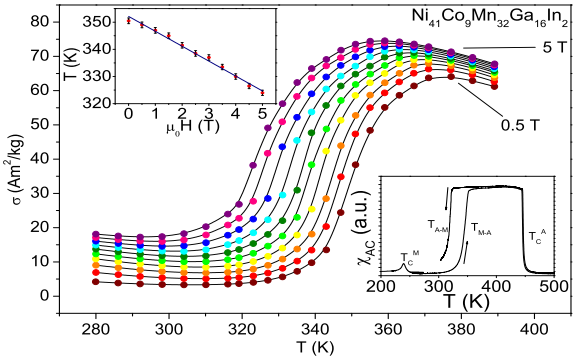

Figure 4.3: (Color online) *M(T)* isofield curves on heating of the martensitic transformation with 0.5T< $\mu_0 H$ <5T on the high ΔM alloy ($Ni_{41}Co_9Mn_{32}Ga_{16}In_2$ - *SampleB*) (field step $\mu_0 H$=0.5T). Upper inset: T_M vs. H phase diagram deduced from isofield curves. Lower inset: a.c. susceptibility plot showing the onset of the paramagnetic gap.

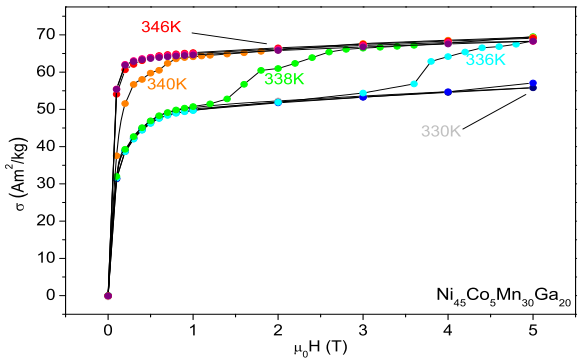

Figure 4.4: (Color online) *M(H)* isothermal curves up to $\mu_0 H = 5$T performed on the low ΔM alloy ($Ni_{45}Co_5Mn_{30}Ga_{20}$ - *SampleA*): 330K< T <346K.

be about 8T for *SampleA* and about 5T for *SampleB* (see section 3.1.1).

The isofield magnetization measurements of *SampleA* at different static magnetic fields up to μ_0H= 5T display the first order transformation around $T_M = 340K$ (Fig. 4.2): the saturation magnetization jump between the two phases reaches $\Delta M = 15 \pm 1$ Am^{2}kg^{-1}, the austenite being the higher moment phase. The same characterization for *SampleB* (Fig. 4.3) shows a broadened martensitic transformation associated to a remarkable variation of the magnetization ($\Delta M = 60 \pm 2$ Am^{2}kg^{-1}): this is due to the concurrent lowering of magnetic moments in martensite while increasing the austenitic saturation magnetization (M_s). The $^{\Delta T_M}/_{\mu_0 \Delta H}$ parameter has been extrapolated by a linear fitting of the critical temperatures in the (T_M vs. H) phase diagram (upper inset of Figs. 4.2 and 4.3), built from the isofield magnetization curves. For *SampleB* a striking value of $^{\Delta T_M}/_{\mu_0 \Delta H}$=-5.49±0.18 K/T is obtained, while for *SampleA* $^{\Delta T_M}/_{\mu_0 \Delta H}$=-1.2±0.07 K/T (Tab. 4.1). It is worth noting that the ΔM and $^{\Delta T_M}/_{\mu_0 \Delta H}$ measured for *SampleB* result to be approximately two and five times respectively the typical values reported for other studied Ni-Mn-X compositions.[41, 42, 82, 49]

M(H) isothermal curves (Figs. 4.4 and 4.5) were collected in a field span of $\mu_0 \Delta H = 5$T paying particular attention to the measurement protocol as described in section 3.1.1. In Figs. 4.6 and 4.6 $\Delta s_T(T)$ curves are reported for both

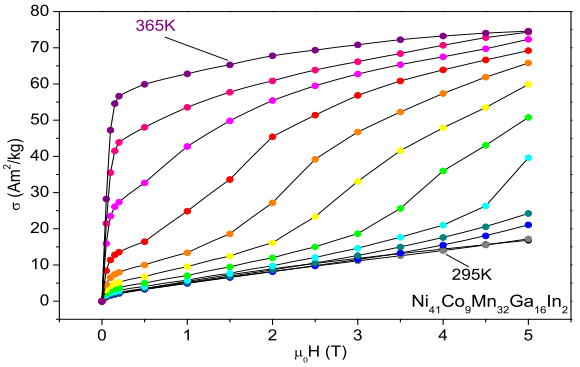

Figure 4.5: (Color online) *M(H)* isothermal curves up to $\mu_0 H = 5$T performed on the high ΔM alloy ($Ni_{41}Co_9Mn_{32}Ga_{16}In_2$ - *SampleB*): 295K$< T <$365K.

Table 4.1: Martensitic transformation features and MCE peak values on heating of *SampleA* (without paramagnetic gap and low ΔM) and *SampleB* (with paramagnetic gap and high ΔM).

	$\mu_0 \Delta H$	*SampleA*	*SampleB*
$\Delta M(\mathrm{Am^2kg^{-1}})$		15 ± 1	60 ± 2
${}^{\Delta T_M}/_{\mu_0 \Delta H}(\mathrm{K/T})$		-1.2 ± 0.07	-5.49 ± 0.18
$-\Delta s_T(\mathrm{JKg^{-1}K^{-1}})$ *Cl-Clap*		-12.5 ± 1.6	-10.9 ± 0.7
$-\Delta s_T(\mathrm{JKg^{-1}K^{-1}})$ *Maxwell*	2T	-10.6 ± 1.6	-6 ± 0.8
$-\Delta s_T(\mathrm{JKg^{-1}K^{-1}})$ *Maxwell*	5T	-13.8 ± 3.3	-9.7 ± 1.9
$\Delta T_{ad}(\mathrm{K})$	1.9T	-1.05 ± 0.15	-1.6 ± 0.15
$RCP(\mathrm{J/kg})$	2T	~ 30	~ 100
$RCP(\mathrm{J/kg})$	5T	~ 70	~ 280

samples. The data have been calculated by means of the Maxwell relation (eq. 2.10) in field spans of $\mu_0\Delta H = 2$T and $\mu_0\Delta H = 5$T, in order to compare respectively the first value with the directly measured $\Delta T_{ad}(T)$ data presented in the paper, and the latter with other $\Delta s_T(T)$ from literature. The obtained peak values are compared with the results of the Clausius - Clapeyron equation (eq. 2.24), calculated around both the field and the temperature induced transitions. The Clausius - Clapeyron equation is justified in the case of complete magnetic field induced transformation. Although for *SampleB* a $\mu_0\Delta H = 5$T field span is not sufficient to fully induce the martensitic transformation (see Fig. 4.5), it is still possible to estimate Δs_T from eq. (2.24) if we introduce the ΔM parameter from the *M(T)* isofield curves. This value can also be obtained by extrapolating the *M(H)* curves of Fig. 4.5 beyond $\mu_0\Delta H = 5$T. The ΔM values calculated both from *M(T)* and *M(H)* curves on *SampleA*, where the transformation is fully induced in a 5T field, are found to be almost coincident.

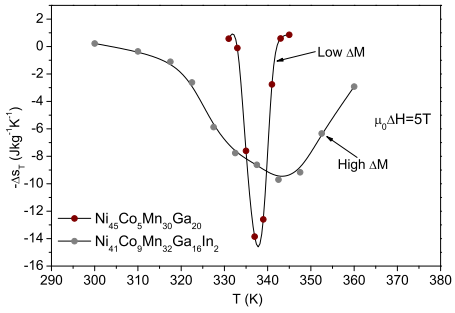

Figure 4.6: Δs_T values of the two different samples, in a $\mu_0 H = 5$T field span.

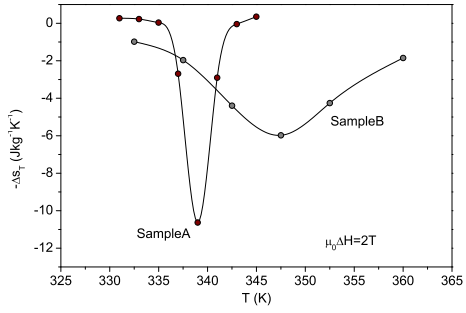

Figure 4.7: Δs_T values of the two different samples, in a $\mu_0 H = 2$T field span

In Fig.4.8 the ΔT_{ad} as a function of temperature across the first order martensitic transformation in a field span of $\mu_0 H = 1.9$T are reported for the two samples. The direct measurements (Fig. 4.9) were performed crossing the cooling martensitic transformation after every adiabatic magnetization, otherwise the high hysteresis would prevent any sensible adiabatic temperature change while cycling with such magnetic field spans. Despite the higher Δs_T peak value of *SampleA*, a remarkable 50% increase of the $|\Delta T_{ad}|$ maximum value is reported for *SampleB*, which shows the paramagnetic gap. *SampleA*, whose phase tran-

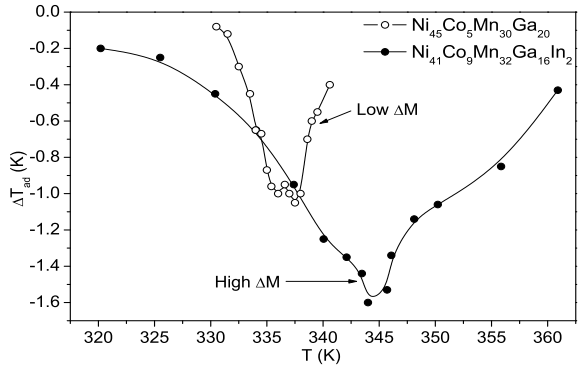

Figure 4.8: Comparison between the $\Delta T_{ad}(T)$ of the two different samples in heating, in a $\mu_0 H = 1.9$T field span. The lines are guides for the eyes. Lower inset: best $\Delta T_{ad}(T)$ value directly measured on the high ΔM alloy ($Ni_{41}Co_9Mn_{32}Ga_{16}In_2$ - *SampleB*).

sition is almost fully induced in a 2T field span, shows however lower $|\Delta T_{ad}|$ values. Fig. 4.9 shows the two ΔT_{ad} peak values of *SampleA* and *SampleB*: the high signal-to-noise ratio achieved by our setup is clearly visible, being the uncertainty of these measurements of ± 0.15K as shown in section 3.4. The ΔT_{ad} peak values of *SampleA* and *SampleB* can be compared with other data up to now found in literature around the critical temperatures (both Curie and martensitic processes) of several Ni-Mn based Heuslers (see table 2.1 in the Materials section). As for the x axis of Fig. 4.8, *SampleA*, as expected in nearly step-like first order processes[7], shows a plateau between 335K and 338K, which corresponds to the width in temperature of the martensitic transition in *M(T)* curves, calculated by considering A_s and A_f as the points where the second order derivative of the *M(T)* curves shows a minimum and a maximum. On the other hand, the widening of the martensitic transformation in *SampleB* extends the temperature range (~ 10K) where significant values of ΔT_{ad} can be exploited.

When comparing samples with similar composition displaying comparable critical temperatures, high $|\Delta T_{ad}|$ are generally expected in correspondence to large Δs_T.[81] However the ratio between the ΔT_{ad} measured in the two samples does not match the one between Δs_T calculated by isothermal magnetization measurements (the peak value of ΔT_{ad} is 50% higher for *SampleB*, while its Δs_T

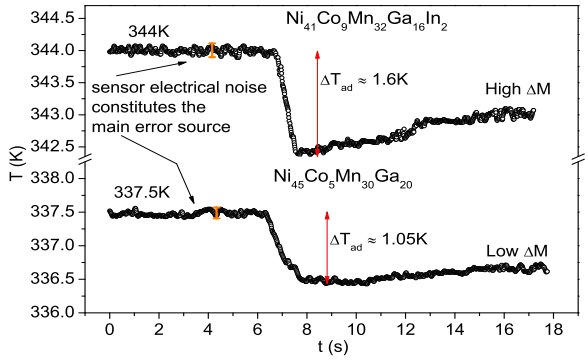

Figure 4.9: (Color online) Comparison between the two peak values of ΔT_{ad} of the two alloys directly measured. It is interesting to compare the field induced ΔT_{ad} with the sensor noise which correspond to the error reported in the paper.

peak value is lower both in 2T and 5T $\mu_0\Delta H$ field spans). It appears that the differences between the ΔT_{ad} peaks are more likely to be connected with different ΔM and $^{\Delta T_M}/_{\mu_0\Delta H}$ values; however, comparing the sensitivities to the applied field of the critical temperatures, while we have the correct indication that *SampleB* is the most promising composition,[7] the difference in the $^{\Delta T_M}/_{\mu_0\Delta H}$ values (-5.48K/T vs. -1.2K/T) is not reflected in the experimental ΔT_{ad} values (-1.6K vs. -1.05K).

In order to correlate the main properties of the martensitic transformation, we apply the graphical model reported in Fig. 4.1 to our measurements. In this qualitative sketch the slopes of the curves between $A_s(\mu_0 H = 0\text{T})$ and $A_f(\mu_0 H = 0\text{T})$ and $A_s(\mu_0 H = 2\text{T})$ and $A_f(\mu_0 H = 2\text{T})$ provide a mean evaluation (which is only qualitative) of the $^{c_{p,H}}/_T$ parameter across the martensitic transformation. The "in-field" *s(T)* curve turns out to be shifted by the applied magnetic field so that:

$A_s(\mu_0 H = 0\text{T}) - A_s(\mu_0 H = 2\text{T}) \approx A_f(\mu_0 H = 0\text{T}) - A_f(\mu_0 H = 2\text{T}) \approx \left(\frac{\Delta T_M}{\mu_0 \Delta H}\right) \mu_0 \Delta H$

where $^{\Delta T_M}/_{\mu_0\Delta H}$ is the mean value of Tab. 4.1 for a field span of 5T. The samples presented here can be compared by exploiting the proportion of eq. (4.1). This relation is a modified version of the well known: $\Delta T_{ad} = -(T/c_{p,H})\Delta s_T$.[5, 81, 64]

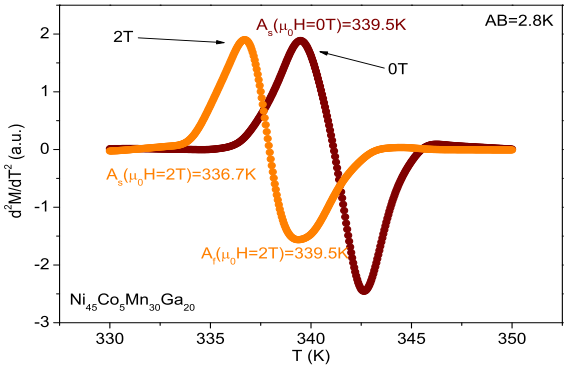

Figure 4.10: (Color online) Magnetization second order derivative on temperature for *SampleA*. $A_s(\mu_0 H = 0\text{T}) \leq A_f(\mu_0 H = 2\text{T})$

Equation (4.1) holds if the following conditions, in fields up to 2T, are realized: (i) $A_s(\mu_0 H = 0\text{T}) \leq A_f(\mu_0 H = 2\text{T})$, so that ${}^{c_{p,H}}/_{T} = \left(\frac{ds}{dT}\right)_H$ is coincident with the hypotenuse DE built on the ΔT_{ad} and Δs_T peak values (see Fig. 4.1), and corresponds to the slope of the entropy curve directly measurable from calorimetric techniques; (ii) the value of heat capacity far below the transformation is similar between the two samples (some c_p values for different *Ni-Mn* compositions are reported in Ref. [74, 83, 84]).

The estimation of the first condition for the two samples is shown in figures 4.10 and 4.11. The reported curves represent the second order derivatives of magnetization in $\mu_0 H = 0\text{T}$ and $\mu_0 H = 2\text{T}$ as a function of temperature. In both cases the martensite-austenite ending temperature of the in field curve does not fall below the martensite-austenite in-field starting thus allowing the application of the construction of figure 4.1. The segment AB is calculated as the difference between the maximum values of the reported curves.

The segment BB', for a $\mu_0 \Delta H$=2T field span, is considered $\sim 0.4 \text{Jkg}^{-1}\text{K}^{-1}$ (inset of Fig. 4.6 and Ref. [42]). The specific heat before A_s has been measured with a DSC 821 METTLER TOLEDO driven by S**TA**R^e Software calorimeter and results about 515 $\text{JKg}^{-1}\text{K}^{-1}$ for both samples, with an error of 2.5%, this measure was then confirmed also with our home made DSC technique. This result is in agreement with literature data.[74, 83, 84] From this measurement

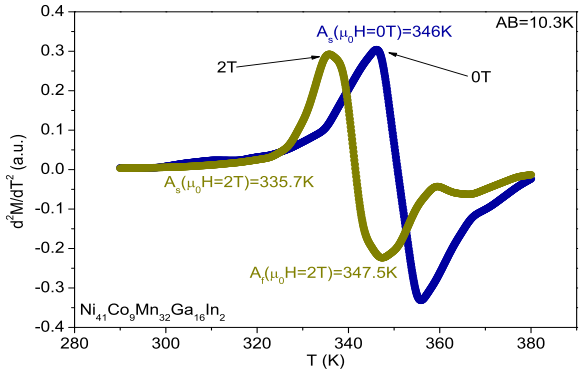

Figure 4.11: (Color online) Magnetization second order derivative on temperature for *SampleB*. $A_s(\mu_0 H = 0\text{T}) \leq A_f(\mu_0 H = 2\text{T})$

Table 4.2: Segments values of Fig. 4.1 for a field change of $\mu_0 H = 2\text{T}$.

Sample	AB (K)	CB ($\text{JKg}^{-1}\text{K}^{-1}$)	Δs_T ($\text{JKg}^{-1}\text{K}^{-1}$)	ΔT_{ad}^{calc} (K)
$Ni_{45}Co_5Mn_{30}Ga_{20}$	-2.8	4.7	10.6	-1.9
$Ni_{41}Co_9Mn_{32}Ga_{16}In_2$	-10.3	16.3	6	-2.8

$\tan\alpha$ turns out about $1.55\text{Jkg}^{-1}\text{K}^{-1}$ for both *SampleA* and *SampleB*. The values related to a field change of $\mu_0 H$=2T are listed in Tab. 4.2.

The difference between the two ΔT_{ad} values deduced from this tentative model (in $\mu_0 \Delta H$=2T) results $\sim 45\%$, while the experimentally measured values differ by $\sim 50\%$ in a $\mu_0 \Delta H$=1.9T. The simple construction presented above gives a more reliable evaluation of the difference between the ΔT_{ad} peak values when compared with the estimation of the same quantity on the basis of the $^{\Delta T_M}/_{\mu_0 \Delta H}$ values or the Δs_T peak values taken alone. An evaluation of the errors linked with the data calculated from eq. (4.1) leads to uncertainties of the order of $40\% - 50\%$ confirming the qualitative character of this construction. Even if the directly

measured ΔT_{ad} peak values are included between the error bars of the calculated ones, they still turn out to be smaller than expected. This gap has already been observed across the first order process of other magnetocaloric materials.[40, 30, 13] Its nature can be partially explained considering several aspects, such as, for instance, the imperfect adiabaticity induced by the finite magnetic field rate. We have estimated from Fig. 4.9 that this effect is responsible for a lowering up to 10% of the two directly measured values, allowing for a reduction of the theoretical and experimental spread under 40%. Therefore we believe that faster field sweep rates could slightly improve the direct measurement. Another issue involves the reactivity of the magneto-structural transformation to fast field changes. However it has been shown[40] that the martensitic transformation should be fast enough to respond to the application of the magnetic field even for sweep rates as high as 2 Ts^{-1}, as in our case.

4.2 Complete magnetothermal characterization of inverse first order processes

4.2.1 $Ni_{44.83}Co_{4.77}Mn_{32.15}Ga_{18.25}$

The origin of the gap between direct and calculated data discussed in section 4.1 has to be clarified to understand the MCE behavior. Several works[13, 40, 64, 85, 62] report large differencies between the directly measured ΔT_{ad} values, which are usually smaller, and the ΔT_{ad} values indirectly deduced from calorimetric and magnetization measurements. Many examples are present in literature of incorrect experimental evaluations that led to the observation of "ghost" Δs_T values coming in particular from *M(H)* curves[10, 50, 86] when irreversibility is not properly taken into account.[55] However the magnetic measurements shown in the previous paragraph were carried out taking care of these issues (see also section 3.1). Other important remarks were made analyzing the different contributions to the magnetic field induced Δs_T.[87] It has been shown that some systems with magnetic critical processes of mixed first and second order nature can be characterized by latent heat, which is magnetic field dependent. In such cases, if further attention is not payed, some experimental techniques could miss particular contributions to the entropy change that could be at the origin of the

observed discrepancies between entropy and temperature changes.[88]

However a reliable correlation between the Δs_T and the ΔT_{ad} peak values for first order processes is not defined. For this reason a study of both these properties (Δs_T and ΔT_{ad}) should be always performed while analyzing the magnetocaloric behavior of a material, together with a proper evaluation of the experimental errors[52, 58].

Few are in literature the works which show at the same time both temperature and magnetic field dependent specific heat, adiabatic temperature and isothermal entropy changes while characterizing first order materials.[89, 57]

Our idea was then to study the behavior of the MCE near a first order process in a model system, trying to understand the correlations between ΔT_{ad} and Δs_T. The three main properties ($c_p(T,H)$, $\Delta T_{ad}(T,\Delta H)$, $\Delta s_T(T,\Delta H)$) have been independently measured using the DSC in-field calorimeter, the direct adiabatic temperature change probe and magnetic characterization respectively. $\Delta T_{ad}(T,\Delta H)$ values have been also calculated from magnetometric $\Delta s_T(T,\Delta H)$ by means of the geometrical model discussed in section 4.1. This approach seemed a promising route to correlate the indirect $\Delta s_T(T,\Delta H)$ with the directly measured $\Delta T_{ad}(T,\Delta H)$ across first order processes: a similar idea was exploited in Ref. [36] leading to a good agreement.

It was recently remarked that studying the MCE for application purposes it would be fundamental to report just the reversible effect measured while the external magnetic field is cycled across first order transformations.[44] The present case, as it will be shown, cannot be used in a real refrigeration cycle because of its large irreversibility. This work is however focused on the correlation between the information that can be deduced from the three main techniques of investigation of the MCE across first order processes by understanding if some of these measurements can lead to over- or under-estimations of the phenomenon, carefully evaluating the error associated with every technique. For this reason just the first cycle of the heating branch of the process is analyzed.

It has to be noted that different techniques generally require a proper sample (see section 3.4) mass to optimize their specific signal to noise ratio. However, when comparing these results on materials undergoing first order transformations, the use of distinct samples, could lead to different values, due to ageing effects, thermomagnetic history and different microstructural features.[13]

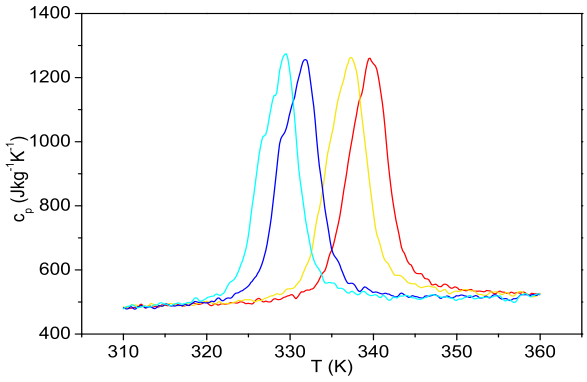

Figure 4.12: (Color online) $c_p(T, H)$ curves performed on heating (red and gold lines) and on cooling (blue and cyan lines) in $\mu_0 H = 0$T and $\mu_0 H = 1.8$T for the sample $Ni_{44.83}Co_{4.77}Mn_{32.15}Ga_{18.25}$.

Furthermore the MCE of different fragments could be influenced also by shape anisotropy. To avoid these problems the complete characterization is performed on the same cuboid sample mass of about 100mg. This alloy, which has composition $Ni_{44.83}Co_{4.77}Mn_{32.15}Ga_{18.25}$, shows a well defined first order martensitic transformation over ambient temperature.

Calorimetric isofield curves at $\mu_0 H = 0$T and $\mu_0 H = 1.8$T for the *Ni-Co-Mn-Ga* sample both in heating and cooling are shown in Fig. 4.12 . The c_p baseline near 300K is close to 500 $Jkg^{-1}K^{-1}$: this value is typical of this kind of alloys.[74, 55, 84] It is clearly detectable the characteristic martensitic thermal hysteresis of $\sim$ 8K both in-field and in zero field curves. The inverse MCE is confirmed from Fig. 4.12 by the negative shift of the transformation temperature in applied field. We have verified that at least for a thermal sweep rate of $0.04Ks^{-1}$ the kinetic correction[74] to the DSC $c_p(T, H)$ curves can be neglected. This contribution does not affect the system MCE while it could affect the width of the thermal hysteresis. Considering a Peltier cell thermal resistance of about $80KW^{-1}$, the estimated thermal hysteresis reduction is less than 10%. The entropy curves calculated from $c_p(T, H)$ are displayed in Fig. 4.13.

Isofield *M(T)* curves (Fig. 4.14) confirm the occurrence of the martensitic transformation in zero field at 340K. The shift induced by the applied field

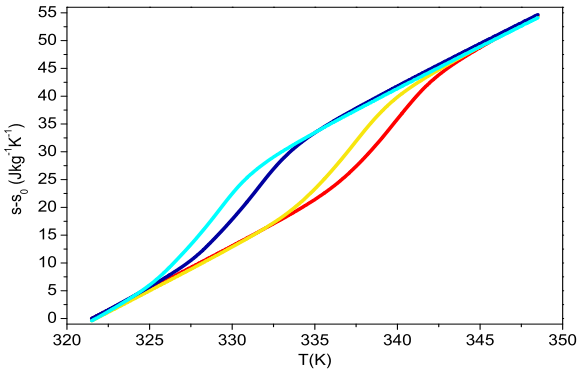

Figure 4.13: (Color online) $s(T,H) - s_0$ curves performed on heating (red and gold lines) and on cooling (blue and cyan lines) in $\mu_0 H = 0$T and $\mu_0 H = 1.8$T for the sample $Ni_{44.83}Co_{4.77}Mn_{32.15}Ga_{18.25}$..

$\Delta T_{M-A} = -2.4 \pm 0.4$K in $\mu_0 \Delta H = 1.8$T is in agreement with the calorimetric measurements of Fig. 4.12. Moreover from the same curves $\Delta M = 16 \pm 1 \mathrm{Am^2 kg^{-1}}$ can be deduced together with an estimation of the Clausius - Clapeyron $\Delta s_T \sim 11.5 \mathrm{Jkg^{-1}K^{-1}}$ relative to the fully induced process. Both martensite and austenite in this sample are ferromagnetic phases leading to a relatively smaller ΔM jump across the first order process with respect to other compositions (see Fig. 2.8 in section 2.2).[47, 48] Isothermal *M(H)* magnetization measurements (Fig. 4.15) show a continuous behavior, and thus their integration to obtain the magnetic field induced Δs_T is analytically allowed[10, 14]. *M(H)* curves, in order to avoid artifact values while calculating the Δs_T, also in this case have been measured taking care to cross the cooling branch of the martensitic transformation after every field sweep.

The isothermal entropy change obtained from $c_p(T,H)$ and *M(H)* curves is reported in Fig. 4.16. The calorimetric Δs_T is deduced subtracting the entropy curve at $\mu_0 H = 0$T from the one at $\mu_0 H = 1.8$T (inset of Fig. 4.12) following Eq. (4.2):

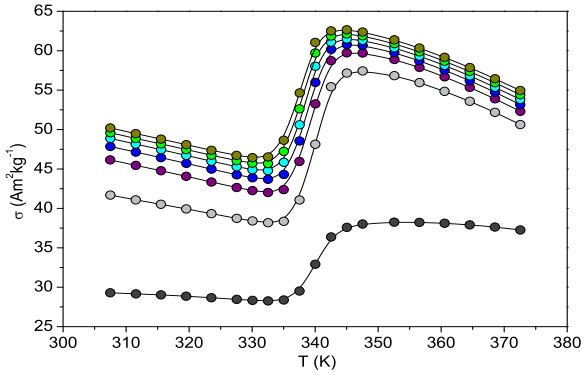

Figure 4.14: (Color online) Isofield magnetization measurements at $\mu_0 H = 0.1, 0.3, 0.6, 0.9, 1.2, 1.5, 1.8$T.

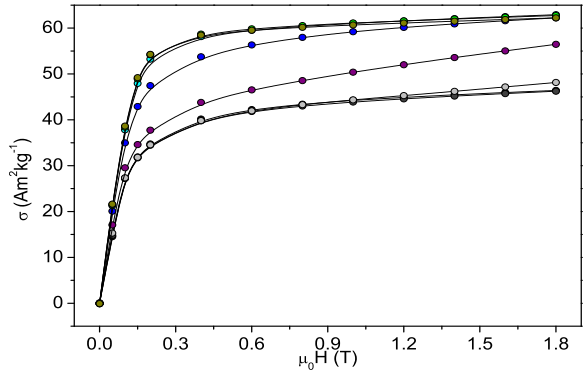

Figure 4.15: (Color online) Isothermal magnetization measurements. The *M(H)* curves were taken at intervals of 3K from 320K to 350K.

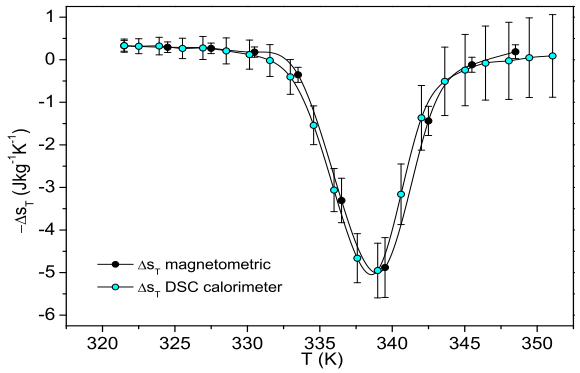

Figure 4.16: Δs_T on heating obtained from calorimetric and magnetometric measurements using the Maxwell relation.

$$\Delta s_T(T, \mu_0 \Delta H) = \Delta s_T(T_i, \mu_0 \Delta H) + \int_{T_i}^{T} \frac{c_p(T, H_2) - c_p(T, H_1)}{T} dT \tag{4.2}$$

where $\Delta H = H_2 - H_1$ and T_i is the reference starting temperature, in the region far below the transformation. $\Delta s_T(T_i, \mu_0 \Delta H) = -0.33 \pm 0.15 \mathrm{Jkg^{-1}K^{-1}}$ is a correction, corresponding to a slight vertical shift of the in-field entropy curve at $T_i = 321.5$K, which is required[74] since the integration starting temperature is above 0K. This $\Delta s_T(T_i, \mu_0 \Delta H)$, obtained from Maxwell elaboration of isothermal *M(H)* curves, is a value reported also for other compositions[74, 42] in a field span of $\mu_0 \Delta H \sim 2$T and it is the magnetic contribution due to the saturation of martensite. This correction, as it was explained along with the description of the experimental setup in section 3.3, is less than $\sim 7\%$ of the peak value. As was explained along with the description of the setup in section 3.3 the effective error on the MCE deduced by DSC calorimetry has been verified to be due to slightly different vacuum conditions between the in-field and the zero field $c_p(T, H)$ curves. This error contribution turns out to be about 0.6% leading in this case to an uncertainty of $\sim 13\%$ for the Δs_T peak value (see Fig. 4.16). Both the in-field and zero field entropy curves are thus affected by an effective relative error of the order of 0.6%, while for the in-field curve an additional constant

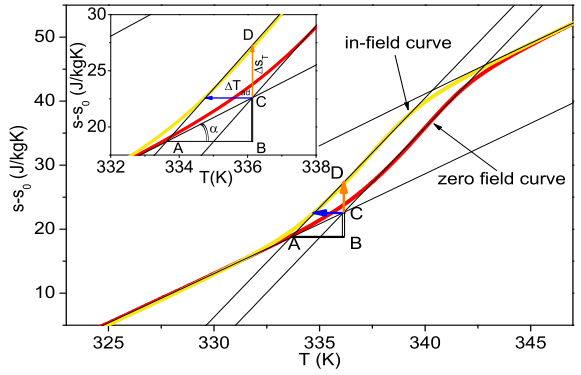

Figure 4.17: (Color online) Real heating calorimetric *s(T,H)* curves across the transformation. The geometrical construction which correlates the different properties of the first order process has been superimposed on them. Inset: enlarged view.

error of $\pm 0.15 \mathrm{Jkg^{-1}K^{-1}}$ has been considered. This term is the uncertainty of the Δs_T of the martensitic phase. These assumptions have been then applied to the standard method of Ref. [51] in order to calculate the final error.

The calorimetric Δs_T curve (Fig. 4.16) reaches a maximum value of $4.95 \pm 0.64 \mathrm{Jkg^{-1}K^{-1}}$ at ~ 339K. Its shape matches the corresponding curve deduced from Maxwell relation while the peak values are in good agreement within their uncertainty. The Δs_T error-bar of the data calculated from *M(H)* curves results $\sim 15\%$.

In figure 4.17 the geometrical construction presented in the previous paragraph that correlates direct and indirect measurements has been superimposed on the calorimetric heating curves. It can be seen that the model matches the real situation since $A_{s-H_1} < A_{f-H_2}$, where A_{s-H_1} (austenite start in $\mu_0 H_1 = 0.1T$) and A_{f-H_2} (austenite finish in $\mu_0 H_2 = 1.8T$) are taken as the second order derivative peaks of the isofield *M(T)* curves (Fig. 4.15). In this case $\tan\alpha \sim \frac{c_p}{T} = 1.5 \pm 0.1 \mathrm{Jkg^{-1}K^{-2}}$ is considered, while $AB = A_{s-H_2} - A_{s-H_1} = 2.5 \pm 0.4$K. The estimation of the adiabatic temperature change comes then from the relation 4.1 (see Fig. 4.17)

In figure 4.18 the different adiabatic temperature change curves are compared: directly measured ones, calculated from magnetometric Δs_T values and obtained

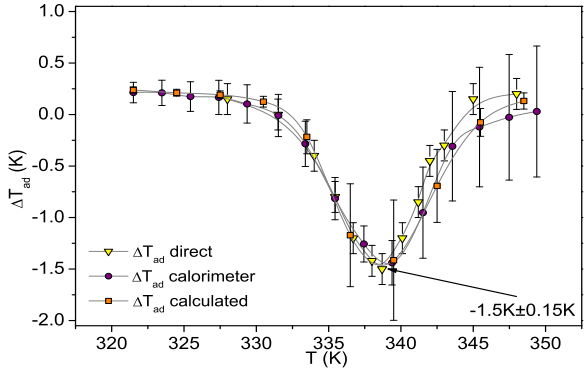

Figure 4.18: (Color online) Cross characterization of ΔT_{ad}. Directly measured (yellow triangles), obtained from c_p data (violet circles) and calculated from Δs_T values (orange squares).

from calorimetric data. The matching between the results of different techniques is evident both from the peak values and from the shape of the curves. The three measurements converge to $\Delta T_{ad} = -1.45 \pm 0.05$K (Fig. 4.18). The calorimetric ΔT_{ad} and its error have been calculated following the treatment of Ref. [51]. The corresponding error-bars after the transition appear consistent as a consequence of the error propagation on Eq. (4.2). This behavior is in good agreement with some results already reported in literature[51]. The errors on the direct ΔT_{ad} measurement are the same all over the curve since they depend on the resistance resolution of the sensor, which is constant. The peak value calculated by means of the model of Fig. 4.17 is affected by a larger error since it follows from multiple elaboration of *M(H)* data.

The complete MCE characterization offered by the DSC, the adiabatic calorimeter and the magnetic characterization could be crucial to uncover the role played by other quantities up to now not taken into account on the thermomagnetic properties of critical processes: one of these is the transformation width.

Figure 4.19 shows how this parameter could be in relation with the magnetocaloric potentials: Δs_T and ΔT_{ad}. A second proportion is depicted in fig. 4.19:

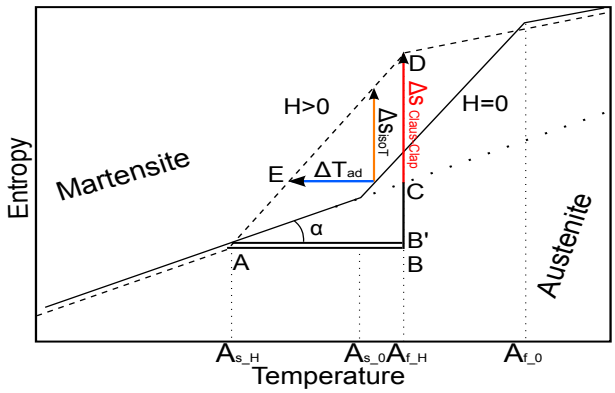

Figure 4.19: (Color online) Geometrical construction of the first order martensitic process in the s *vs.* T plane. The behavior of ΔT_{ad} peak value can be estimated from Δs_T peak values obtained from *M(H)* curves, the c_p of the martensite below the transformation region and transformation width.

$$AB : \Delta T_{ad} = (\Delta s_{T(C-C)} + CB) : \Delta s_T \tag{4.3}$$

where AB is the in-field transformation width, $\Delta s_{T(C-C)}$ is the isothermal entropy jump corresponding to the fully magnetic field induced transformation: it could be estimated from the Clausius Clapeyron equation, and:

$$CB = AB \tan\alpha = AB \frac{C_{p-mart}}{T}$$

This idea is probably consistent since the transformation width with is not just a "geometrical parameter" of the material phase diagram but is a quantity which depends on the nature of the two phases: as an example it could be correlated to the volume change across the process. In particular the transformation width influences the elastic properties which are strictly correlated with the magnetocaloric properties. The determination of the transformation width is however not straightforward. A deep investigation on this should be performed. In the present case the width of the transformation is considered as the distance between the second order derivative peaks of magnetization on temperature.

4.2.2 Other compositions

The MCE characterization presented in the previous section was performed also on other available alloys, showing the martensitic transformation in the working temperature range of the three experimental techniques (280K$<T_M<$390K). In particular it was intriguing to measure the specific heat behavior of *SampleA* ($Ni_{45}Co_5Mn_{30}Ga_{20}$) and *SampleB* ($Ni_{41}Co_9Mn_{32}Ga_{16}In_2$) presented in section 4.1.

$Ni_{45}Co_5Mn_{30}Ga_{20}$

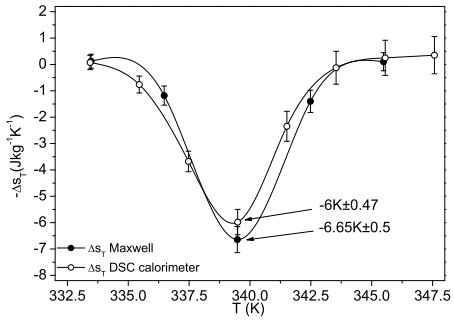

Figure 4.20: Isothermal entropy changes of a $\sim$ 30mg $Ni_{45}Co_5Mn_{30}Ga_{20}$

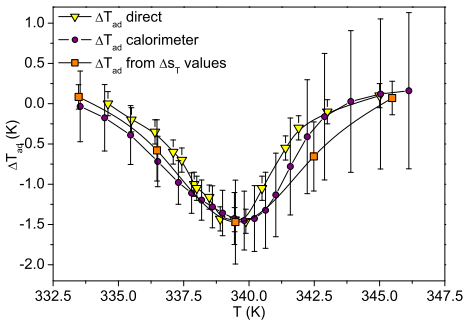

Figure 4.21: Adiabatic temperature changes of a $\sim$ 30mg $Ni_{45}Co_5Mn_{30}Ga_{20}$

The high mass sample ($\sim$ 100mg) used for the ΔT_{ad} characterization broke right after the measurements then it become unusable with the DSC. Another fragment ($\sim$ 30mg) taken from the same batch was fully studied. The temperature dependencies of Δs_T and ΔT_{ad} values are shown in figures 4.20 and 4.21. The reported values match within the respective errors for both quantities. Comparing however the data of section 4.1 with the present one it can be noticed a clear mismatch between the results obtained from the different fragments. Magnetic measurements were performed on one of the remaining pieces of the original high mass sample. The results are shown in fig. 4.23 and 4.22 reporting the M(T) curves and the relative Δs_T, which turns out to be much lower than the values measured on the smaller fragment ($\sim$ 10mg) of section 4.1. This result was expected because of two reasons. First of all it was shown that just 30mg in case

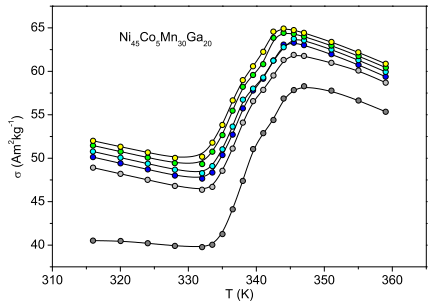

Figure 4.22: Magnetization isofield curves across the heating martensitic transformation of the half remaining part of the sample used in section 4.1 for the ΔT_{ad}.

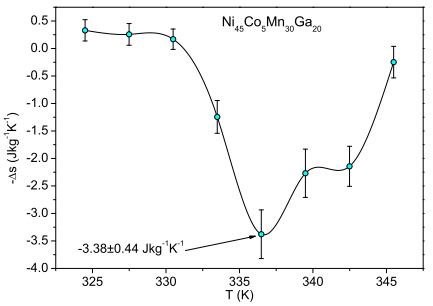

Figure 4.23: Isothermal entropy change curve for a magnetic field span of $\mu_0 \Delta H = 2T$ corresponding to the martensitic transformation of fig. 4.22.

of $Ni_{45}Co_5Mn_{30}Ga_{20}$ composition are sufficient to measure its ideal ΔT_{ad}, thus the origin of the mismatches reported in section 4.1 was not due to inaccuracy of the adiabatic calorimeter. Secondly from figures 4.20 and 4.21 is was clear that the simple model used to calculate ΔT_{ad} from Δs_T well describes the behavior of this martensitic process. Since the mismatches between the expected and the measured ΔT_{ad} values are not to be ascribed to measurement malfunctioning or particular inaccuracies of the described geometrical model, probably the MCE of the two samples behaves differently. This implies that the results (ΔT_{ad}) predicted in section 4.1 for the two small fragments (12mg and 5mg) would be interesting to be directly verified.

$Ni_{41}Co_9Mn_{32}Ga_{16}In_2$

DSC characterization was performed also on *SampleB* ($Ni_{41}Co_9Mn_{32}Ga_{16}In_2$) of section 4.1. In this case the $\sim$ 170mg sample used for the direct measurement was analyzed together with another fragment of $\sim$ 26mg. In order to study the magnetization of the higher mass system, unusual measurement parameters were adopted to avoid the saturation of the pick up coils of the SQuID magnetometer due to large signals (austenite net magnetization saturation value for this sample is $\sim 13 Am^2kg^{-1}$). As observed in the case of $Ni_{45}Co_5Mn_{30}Ga_{20}$ alloy the Δs_T

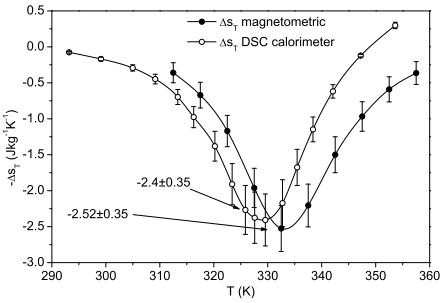

Figure 4.24: Isothermal entropy changes of a $\sim$ 170mg $Ni_{41}Co_9Mn_{32}Ga_{16}In_2$ sample

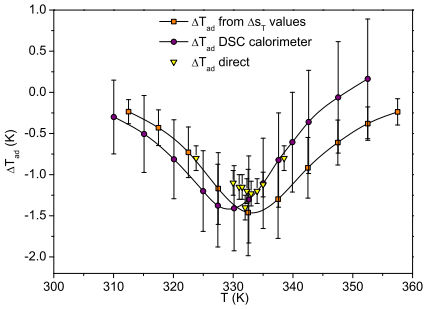

Figure 4.25: Adiabatic temperature changes of a $\sim$ 170mg $Ni_{41}Co_9Mn_{32}Ga_{16}In_2$ sample

of the high mass system was much lower than that reported for the 5mg sample (section 4.1). The ΔT_{ad} calculated and deduced from DSC calorimetry is in this case very similar to that directly measured. However ageing contributed to shift the martensitic transformation 10K lower than that reported in section 4.1 and also the MCE seemed to contract leading to lower values. This behavior opens however new question on the presence of "relaxation" effects in some martensitic alloys. As introduced in section 2.2.2, these processes should be characterized by a not diffusive nature. The data here reported however testify an opposite phenomenology. A possible explanation of the presence of time dependent effects in first order processes could be linked to the higher complexity of the sample structure. It would be interesting to deepen whether the high number of atomic substitutions could be responsible of an alteration of the original properties of the martensitic structure.

Another fragment of the original batch, with mass of $\sim$ 26mg intermediate between those of samples shown in section 4.1, was also characterized. The Δs_T of this sample falls between the values reported for the other two examples of same stoichiometry (see Tab. 4.3). As far as the ΔT_{ad} is concerned both magnetic measurements and DSC calorimetry data predict values which are in agreement one with the other but at the same time higher than those directly measured by means of the adiabatic probe. In the latter case the too low sample mass, not sufficient to measure a temperature variation within the error threshold, is the cause. Furthermore for these two samples the reliability of the proposed model

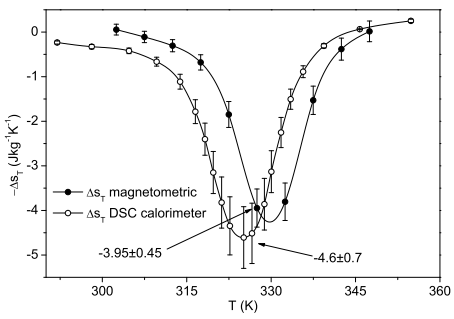

Figure 4.26: Isothermal entropy changes of a $\sim$ 26mg $Ni_{41}Co_9Mn_{32}Ga_{16}In_2$ fragment

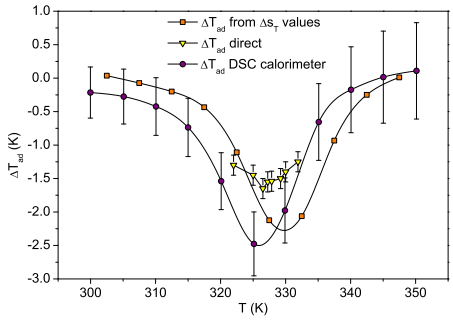

Figure 4.27: Adiabatic temperature changes of a $\sim$ 26mg $Ni_{41}Co_9Mn_{32}Ga_{16}In_2$ fragment

is weaker since one of the two geometrical constraints which discriminate its applicability is unsatisfied: $A_s(\mu_0 H = 0\mathrm{T}) \geq A_f(\mu_0 H = 2\mathrm{T})$.

$Ni_{45}Co_5Mn_{31}Ga_{19}$

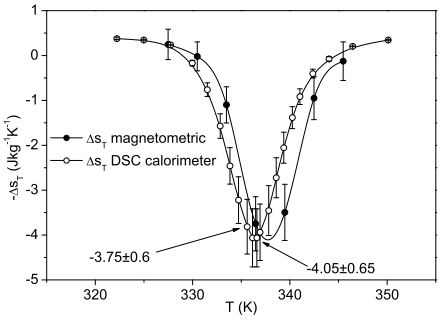

Figure 4.28: Isothermal entropy changes of a $\sim$ 20mg $Ni_{45}Co_5Mn_{31}Ga_{19}$

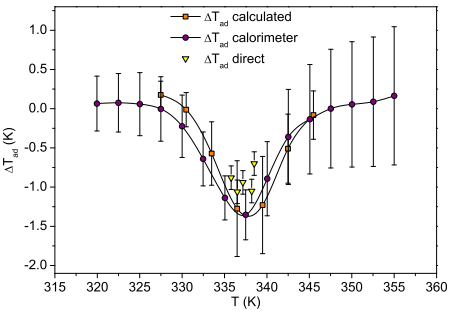

Figure 4.29: Adiabatic temperature changes of a $\sim$ 20mg $Ni_{45}Co_5Mn_{31}Ga_{19}$

The MCE also for different $Ni_{45}Co_5Mn_{31}Ga_{19}$ fragments was analyzed. Figures 4.28 and 4.29 show the entropy and temperature variations obtained for this system. In this case a good agreement within the errors is found between the three techniques. Furthermore the values reported for this fragment turn out to

be similar with the ones reported in section 4.2. As shown in table 4.3 also the MCE obtained from M(H) curves of a 9mg sample is near to the ones estimated for the other two fragments. This could be the fingerprint of a better homogeneity in this case. In table 4.3 are summarized all the MCE values measured for the three compositions studied in this section.

Table 4.3: MCE measured with the three experimental techniques on three different compositions and sample masses.

	Isothermal entropy change ($Jkg^{-1}K^{-1}$)		Adiabatic temperature change (K)		
$Ni_{45}Co_5Mn_{31}Ga_{19}$	Maxwell elab	DSC	Adiabatic cal	DSC	Model proposed
9mg	3.9 ± 1				
21mg	3.75 ± 0.6	4.05 ± 0.65	-1.1 ± 0.15	-1.33 ± 0.28	-1.27 ± 0.75
100mg	4.9 ± 0.7	4.95 ± 0.64	-1.43 ± 0.15	-1.44 ± 0.32	-1.41 ± 0.64
$Ni_{45}Co_5Mn_{30}Ga_{20}$	Maxwell elab	DSC	Adiabatic cal	DSC	Model proposed
12mg	10.6 ± 1.6				
31mg	6.65 ± 0.5	6 ± 0.47	-1.46 ± 0.15	-1.45 ± 0.37	-1.47 ± 0.52
100mg	3.38 ± 0.44		-1.05 ± 0.15		-1.18 ± 0.57
$Ni_{41}Co_9Mn_{32}Ga_{16}In_2$	Maxwell elab	DSC	Adiabatic cal	DSC	Model proposed
5mg	6 ± 0.8				
25mg	3.95 ± 0.45	4.6 ± 0.7	-1.65 ± 0.15	-2.47 ± 0.47	-2.12 ± 1
170mg	2.52 ± 0.35	2.4 ± 0.35	-1.4 ± 0.15	-1.41 ± 0.51	-1.46 ± 0.52

CHAPTER 5

Magnetocaloric effect in nearly operative conditions: simulation of real magnetothermal cycles

Some recent works have focused the impact of hysteresis on the magnetocaloric properties of first order processes.[44, 90, 91] The investigation of irreversible effects is basic since for application purposes (refrigerators, air conditioning units, heat pumps) the largest and reversible MCE is needed. Testing in nearly operative conditions the system magnetothermal properties could help to handle some applicative issues. Some of such questions are about the material thermal transport, its mechanical properties and the transformation kinetics while the magnetic field is applied and removed at high frequencies.[92]

The action of subsequent magnetothermal cycles across magneto-structural and magneto-elastic processes can sometimes weaken the system inducing fatigue on the lattice.[93, 94] The occurrence of such effects could be investigated measuring the material MCE while the magnetic field is cycled in nearly operative conditions. It would be expected that the observation of time dependent MCE variations could be a fingerprint of fatigue. A sudden or a progressive change of MCE could discriminate different magnetomechanical behaviors. Further studies on the nature of fatigue could contribute to deepen the knowledge on the studied materials.

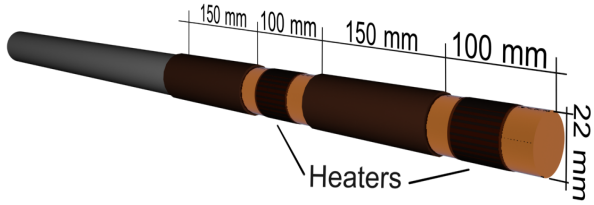

Figure 5.1: (Color online) Drawing of the cryostat insert. This attachment allows to control T hot and T cold in and out of the magnet for the simulation of thermomagnetic cycles

The analysis of the effect of the external magnetic field on the system could also allow to understand how the material thermal transport properties affect the maximum speed at which the MCE can be cycled. This perspective is important in particular considering that such materials will have to work at high frequencies (10^1 - 10^2Hz) to approach the working power of actual devices.[95, 96] Similar analyses could also be insightful while studying first order processes characterized by transformation time constants comparable with the field pulses. In these cases it would be expected a coherent dependence of the measured MCE on the magnetic field variation rate.[40]

Moreover such experiments, as already reported,[44, 90, 91] clarify the impact of hysteresis on the MCE. This is immediate by comparing the effect induced by the very first magnetic field action and the subsequent ones.

For these purposes a pneumatic cylinder was used to insert and extract the sample in and out the magnetic field: it spans about 25cm in 0.15s. The used cryostat is a continuous flow Oxford Instruments CF1200 while the magnetic field source was an electromagnet whose maximum magnetic field is ~ 1.85T. The idea was to continuously measure the temperature of the sample while it is pushed inside and pulled outside the magnetic field. The performed thermomagnetic cycle is then constituted by two adiabatic and two isofield branches thus simulating the operation of a Brayton cycle (see fig. 5.2) with two stages at different magnetic field and temperature. To accurately control the temperature in the "zero field" region a suitable cryostat insert has been designed and realized (Fig. 5.1). The attachment shown in figure is a tube made up of two copper regions (one between the poles and the other outside) thermally insulated one from the other through

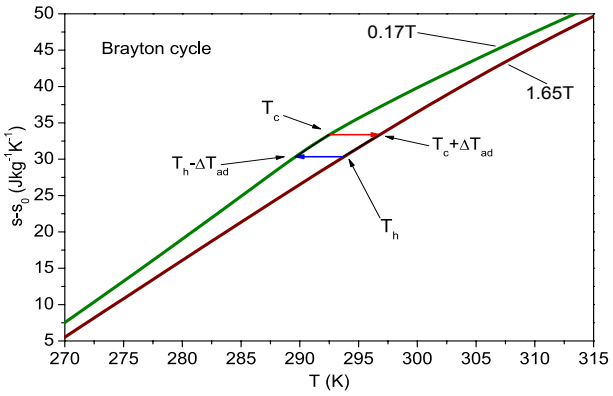

Figure 5.2: (Color online) Brayton cycle constructed on the in-field DSC entropy curves.

a Tufnol^R part (Fig. 5.1). The temperature of the two copper regions where the sample is extracted and inserted is controlled through two Omega Kapton Insulated Flexible Heaters able to power up to $\sim$ 20W.[97] The heat exchange medium between sample and the external reservoir is helium gas. In this setup the temperature of the heat and cold reservoirs are not monitored because the aim is to test small fragments to extract informations about their response to periodic magnetization and demagnetization stresses and thus this instrument is not a magnetic refrigeration tester.

Figure 5.2 shows the entropy s(T,H) diagram for $\mu_0 H_i = 0.17T$ and $\mu_0 H_i = 1.65T$ (which are the two internal magnetic fields between will be performed the ΔT_{ad} cycles). A preliminary calorimetric characterization can be convenient since it allows to trace the magnetothermal cycle directly on the entropy-temperature phase diagram. This could help to better visualize the path followed by the system during the measurement. In this case a simple Brayton cycle is drawn between the in-field and the out-of-field states.

Figure 5.3 reports four different examples of magnetothermal cycles performed on a Gadolinium sample of $\sim$ 110mg near its Curie temperature. T_{cold} and T_{hot} points were changed from one measurement to the other. It can be firstly noticed for every case the repeatability of the effect on subsequent branches, as it was expected across the Curie transition of Gadolinium: the absence of hysteresis is confirmed since MCE differences between the first branch and the subsequent

ones are not detectable. The magnetic field sweep in this case is faster (~ 0.15s) than for the "single" ΔT_{ad} measurement described in section 3.2 and 3.4. The maximum measured $\Delta T_{ad} \sim 3.5$K is then compared to the value deduced from the DSC measurement in the same applied fields. In this case the two techniques match exactly. The value of 3.2K reported at 289.5K (figure 5.3 c) is on the other hand about 0.2K lower than the DSC estimation. This is mainly due to the worst adiabatic conditions of the latter experiment which was purposely performed to check the maximum attainable frequency. The cycle frequency was increased up to 0.33Hz to approach as far as possible operative conditions of real prototypes.[98]

In this setup the cycles frequency can be increased moving away T_{hot} from T_{cold}: in particular, in this case, the "in-field" region is lower in temperature than the zero field one. The system heats up when it is put in the magnetic field but it suddenly starts to cool down. As soon as its temperature equals the "virtual" T_{hot} the sample is extracted outside the field. This experimental conditions are functional just to observe the material behavior while it is stressed in a nearly operative way.

In figure 5.3 d) the temperature of the out of field region was purposely changed while performing the measurement in order to show how the thermal relaxation of the isofield branches can be varied. This feature allows then to adequately control the cycle frequency depending on every particular characterization requirement.

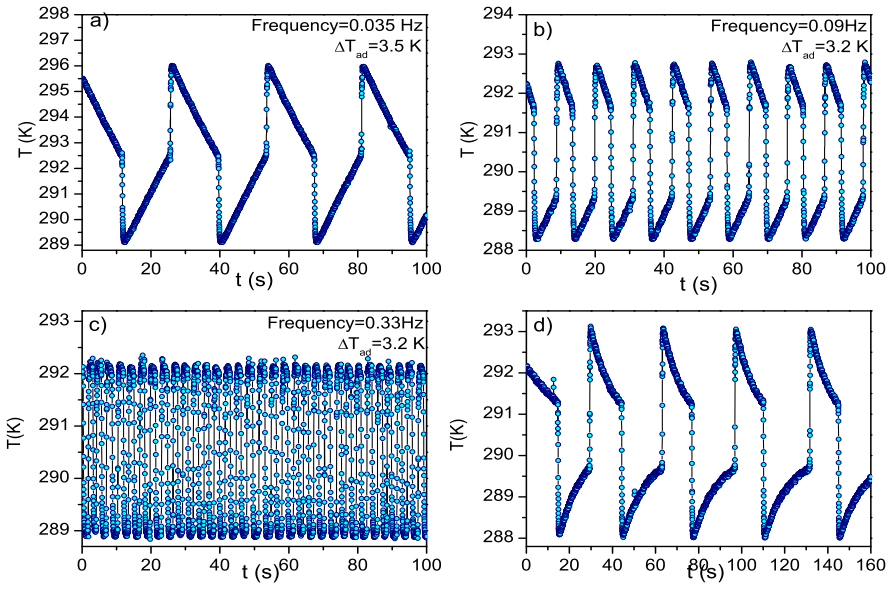

Figure 5.3: (Color online) Brayton cycles monitored through ΔT_{ad} measurements at different frequencies. Figures a), b) and c) report the Gadolinium magnetocaloric behavior for different "hot" and "cold" temperatures of the cycle. Figure d) shows how can be varied the cycle frequency as function of the temperature of the regions: in this example the temperature of the "cold region" is lowering to reduce system anadiabaticity.

CHAPTER 6

Conclusions and Outlooks

In this thesis the magnetocaloric effect of first order martensitic transformations has been discussed comparing the results of the three main techniques of characterization: magnetometry, adiabatic magnetic calorimetry and in-field differential scanning calorimetry. Two in-field calorimeters were purposely developed for this aim.

The first goal of this work has been the realization of the in field DSC which allowed to directly correlate the isothermal entropy change, measured as often reported in literature through magnetic characterization, with the adiabatic temperature variations in correspondence of first order magnetic phase transitions. This, together with a detailed analysis of the errors, allowed to verify the reliability of the different experimental protocols while studying first order processes. By separately measuring $\Delta s_T(T, \Delta H), \Delta T_{ad}(T, \Delta H)$ and $c_p(T, H)$ on the same sample it was verified the matching between the MCE values estimated with the different techniques. Different ageing effects, microstructural defects, thermomagnetic histories and demagnetizing fields of different fragments, also if taken from the same batch, could be responsible of differences between the MCE values obtained by the three methods and not included in the measurement errors. The converging results confirm the suitability of Maxwell elaboration of isothermal

M(H) curves also in the case of first order processes, in agreement with the point of view of some already published works.[69, 50, 14] Furthermore this deep characterization offered some clues about the kinetics of the martensitic transformation. The concurrent application of techniques characterized by different time scales (from $\sim 10^{-3}$T/s to ~ 2T/s) to the same process has lead to very similar results. This could support the hypothesis that in these systems the fast field sweep rates applied while performing the direct measurement should not compete with the kinetics of the martensitic transformation.

The second goal has been the realization of the adiabatic temperature change probe which allows to directly detect the samples temperature change induced by a variable magnetic field. The capabilities of this instrument were discussed testing its sensitivity as a function of the measured sample mass and comparing the direct ΔT_{ad} values with the estimation of the same quantity performed by means of the in-field DSC.

The third goal of this thesis was the study of a coherent magnetometric measurement protocol together with the realization of a simple geometrical construction to correlate across first order processes Δs_T and ΔT_{ad} values.

The realized experimental setups together with the model provided the appropriate conditions to undertake the study of Co substituted *Ni-Mn* compounds. The concurrent characterization of both Δs_T and ΔT_{ad} allowed the performed deep analysis of the thermomagnetic behavior Ni-Mn-Co-Ga based Heuslers.

A pneumatic linear actuator was implemented to insert and extract the adiabatic temperature change probe inside and outside the magnetic field. This implementation together with a cryostat insert purposely built to control the system temperature also in the region outside the magnet were realized to stress the materials through cycled magnetization and demagnetization actions. The simultaneous measurement of the sample temperature could be insightful to study the material MCE under nearly operative conditions. Fatigue effects on the materials structure could then be directly analyzed depending on different variables such as the cycling frequency, time, magnetic field. Some promising systems show high MCE across transitions with first-to-second order transitions.[12, 99, 51, 9, 100] The study of fatigue effects in these materials could contribute to deepen the knowledge of such processes, while contributing to develop new systems.

It would be interesting to compare the mechanical properties of materials

showing purely first order transformations with others characterized by processes showing mixed first-to-second order features. This analysis would contribute to a better comprehension of the phenomenology of such processes across their critical points. The interplay between thermal conductivity and materials MCE could constitute another interesting issue to be investigated.

List of publications

G. Porcari, F. Cugini, S. Fabbrici, C. Pernechele, F. Albertini, M. Buzzi, M. Mangia, and M. Solzi, *"Convergence of direct and indirect methods in the magnetocaloric study of first order transformations: the case of Ni-Co-Mn-Ga Heusler alloys"* Phys. Rev. B 86, 104432 (2012).

G. Porcari, S. Fabbrici, C. Pernechele, F. Albertini, M. Buzzi, A. Paoluzi, J. Kamarad, Z. Arnold, and M. Solzi, *"Reverse magnetostrucural transformation and adiabatic temperature change in* Co *and* In *substituted* Ni-Mn-Ga *alloys"* Phys. Rev. B 85, 024414 (2012).

S. Fabbrici, J. Kamarad, Z. Arnold, F. Casoli, A. Paoluzi, F. Bolzoni, R. Cabassi, M. Solzi, G. Porcari, C. Pernechele, and F. Albertini, *"From direct to inverse giant magnetocaloric effect in Co-doped NiMnGa multifunctional alloys"* Acta Mater. 59, 412 (2011).

F. Albertini, S. Fabbrici, A. Paoluzi, J. Kamarad, Z. Arnold, L. Righi, M. Solzi, G. Porcari, C. Pernechele, D. Serrate, and P. Algarabel, *"Reverse Magnetostructural Transitions by Co and In Doping NiMnGa Alloys: Structural, Magnetic, and Magnetoelastic Properties"* Mater. Sci. Forum 684, 151 (2011).

G. Porcari, M. Buzzi, F. Cugini, R. Pellicelli, C. Pernechele and M. Solzi, *"Adiabatic temperature change probe and direct simulation of high frequency magnetothermal cycles"*, in preparation.

Bibliography

[1] E. Warburg. Magnetische Untersuchungen. *Ann. Phys. (Leipzig)*, 249:141, (1881).

[2] P. Debye. Einige Bemerkungen zur Magnetisierung bei tiefer Temperatur. *Ann. Phys. (Leipzig)*, 386:1154, (1926).

[3] W. F. Giauque. A thermodynamic treatment of certain magnetic effects. A proposed method of producing temperatures considerably below 1° absolute. *J. Am. Chem. Soc.*, 49:1864, (1927).

[4] H. B. Callen. *Thermodynamics and an introduction to Thermostatistics.* Wiley, New York, 1985.

[5] A. M. Tishin and Y. I. Spichkin. *The Magnetocaloric Effect and its Applications.* Institute of Physics, Bristol, 2003.

[6] A. Kitanovski and P. Egolf. Thermodynamics of magnetic refrigeration. *Int. J. Refrig.*, 29:3, (2006).

[7] V. K. Pecharsky and K. A. Gschneidner Jr. and A. O. Pecharsky and A. M. Tishin. Thermodynamics of the magnetocaloric effect. *Phys. Rev. B*, 64:144406, (2001).

[8] http://old.iupac.org/publications/analytical_compendium/Cha01sec38.pdf.

[9] E. Brück. *Magnetocaloric refrigeration at ambient Temperature.* Handbook of Magnetic Materials, vol. 17, ch. 4, Buschow, K. H. J., Ed. (Elsevier, Amsterdam), 2007.

[10] L. Caron and Z. Q. Ou and T. T. Nguyen and D. T. Cam Thanh and O. Tegus and E. Brück. On the determination of the magnetic entropy change in materials with first-order transitions. *J. Magn. Magn. Mater.*, 321:3559, (2009).

[11] A. Giguere and M. Foldeaki and B. Ravi Gopal and R. Chahine and T. K. Bose and A. Frydman and J. A. Barclay. Direct Measurement of the "Giant" Adiabatic Temperature Change in $Gd_5Si_2Ge_2$. *Phys. Rev. Lett.*, 83:2262, (1999).

[12] O. Gutfleisch and M. A. Willard and E. Brück and C. H. Chen and S. G. Sankar and J. P. Liu. Magnetic Materials and Devices for the 21st Century: Stronger, Lighter, and More Energy Efficient. *Adv. Mater.*, 23:821, (2011).

[13] K. A. Gschneidner Jr. and V. K. Pecharsky and A. O. Tsokol. Recent developments in magnetocaloric materials. *Rep. Prog. Phys.*, 68:1479, (2005).

[14] K. A. Gschneidner Jr. and V. K. Pecharsky and E. Brück and H. G. M. Duijn and E. M. Levin. Comment on "Direct Measurement of the 'Giant' Adiabatic Temperature Change in $Gd_5Si_2Ge_2$". *Phys. Rev. Lett.*, 86:4190, (1999).

[15] N. H. Dung and L. Zhang and Z. Q. Ou and E. Brück. From first-order magneto-elastic to magneto-structural transition in $(Mn,Fe)_{1.95}P_{0.50}Si_{0.50}$ compounds. *Appl. Phys. Lett.*, 99:092511, (2011).

[16] S. Yu. Dan'kov and A. M. Tishin and V. K. Pecharsky and K. A. Gschneidner Jr. Magnetic phase transitions and the magnetothermal properties of gadolinium. *Phys. Rev. B*, 57:3478, (1998).

[17] A. Smith and C. R. H. Bahl and R. Bjørk and K. Engelbrecht and K. K. Nielsen and N. Pryds. Materials Challenges for High Performance Magnetocaloric Refrigeration Devices. *Adv. Energy Mater.*, 2:1288, (2012).

[18] V. I. Zverev and A. M. Tishin and M. D. Kuz'min. The maximum possible magnetocaloric ΔT effect. *J. Appl. Phys.*, 107:043907, (2010).

[19] V. K. Pecharsky and K. A. Gschneidner Jr. Comparison of the Magnetocaloric Effect derived from heat capacity, direct, and magnetization measurements. *Adv. Cryog. Eng.*, 42:423, (1996).

[20] A. N. Vasil'ev and V. D. Buchel'nikov and T. Takagi and V. V. Khovaylo and E. I. Estrin. Shape memory ferromagnets. *Usp. Fiz. Nauk.*, 153:577, (2003).

[21] L. Kaufman and M. Cohen. Thermodynamics and kinetics of martensitic transformations. *Prog. Met. Phys.*, 7:165, (1958).

[22] F. Albertini and L. Pareti and A. Paoluzi and L. Morellon and P.A. Algarabel and M.R. Ibarra and L. Righi. Composition and temperature dependence of the magnetocrystalline anisotropy in $Ni_{2+x}Mn_{1+y}Ga_{1+z}$ (x+y+z = 0) Heusler alloys. *Appl. Phys. Lett.*, 81:4032, (2002).

[23] R. Kainuma and Y. Imano and W. Ito and Y. Sutou and H. Morito and S. Okamoto and O. Kitakami and K. Oikawa and A. Fujita and T. Kanomata and K. Ishida. Magnetic-field-induced shape recovery by reverse phase transformation. *Nature*, 439:957, (2006).

[24] K. Ullakko J. K. Huang C. Kantner R. C. O'Handley and V.V. Kokorin. Large magnetic-field-induced strains in Ni2MnGa single crystals. *Appl. Phys. Lett.*, 69:1966, (1996).

[25] A. Sozinov and A. A. Likhachev and N. Lanska and K. Ullakko. Giant magnetic-field-induced strain in NiMnGa seven-layered martensitic phase. *Appl. Phys. Lett.*, 80:1746, (2002).

[26] M. Kohl and B. Krevet and T. Grund and J. Barth and D. Auernhammer and F. Khelfaoui. Engineering Aspects of Shape Memory Film Actuators and Sensors. *Adv. Sci. Tech.*, 59:119, (2008).

[27] L. Pareti and M. Solzi and F. Albertini and A. Paoluzi. Giant entropy change at the co-occurrence of structural and magnetic transitions in the Ni Mn Ga Heusler alloy. *Eur. Phys. J. B*, 32:303, (2003).

[28] T. Krenke and E. Duman and M. Acet and E. F. Wassermann and X. Moya and L. Mañosa and A. Planes. Inverse magnetocaloric effect in ferromagnetic Ni-Mn-Sn alloys. *Nature Mater.*, 4:450, (2005).

[29] F. Albertini and A. Paoluzi and L. Pareti and M. Solzi and L. Righi and E. Villa and S. Besseghini and F. Passaretti. Phase transitions and magnetic entropy change in Mn-rich Ni_2MnGa alloys. *J. Appl. Phys.*, 100:023908, (2006).

[30] A. Planes and L. Mañosa and M. Acet. Magnetocaloric effect and its relation to shape-memory properties in ferromagnetic Heusler alloys. *J. Phys.: Condens. Matter*, 21:233201, (2009).

[31] L. Righi and F. Albertini and A. Paoluzi and S. Fabbrici and E. Villa and G. Calestani and S. Besseghini. Incommensurate and Commensurate Structural Modulation in Martensitic Phases of FSMA. *Mat. Sci. Forum*, 635:33, (2010).

[32] L. Righi and F. Albertini and E. Villa and A. Paoluzi and G. Calestani and V. Chernenko and S. Besseghini and C. Ritter and F. Passaretti. Crystal structure of 7M modulated Ni-Mn-Ga martensitic phase. *Acta Mater.*, 56:4529, (2008).

[33] L. Righi and F. Albertini and L. Pareti and A. Paoluzi and G. Calestani. Commensurate and incommensurate "5M" modulated crystal structures in Ni-Mn-Ga martensitic phases. *Acta Mater.*, 55:5237, (2007).

[34] http://www.youtube.com/watch?v=fsBHF_j2FJ4.

[35] http://www.youtube.com/watch?v=5mZgNQLGqDc.

[36] J. Liu and T. Gottschall and K. P. Skokov and J. D. Moore and O. Gutfleisch. Giant magnetocaloric effect driven by structural transitions. *Nature Mater.*, 11:620, (2012).

[37] C. P. Sasso and M. Pasquale and L. Giudici and S. Besseghini and E. Villa and L. H. Lewis and T. A. Lograsso and D. L. Schlagel. Magnetostructural transitions and adiabatic temperature variation in polycrystal and single-crystal Ni2MnGa alloys. *J. Appl Phys.*, 99:08K905, (2006).

[38] M. Pasquale and C. P. Sasso and L. Giudici and T. Lograsso and D. Schlagel. Field-driven structural phase transition and sign-switching magnetocaloric effect in Ni-Mn-Sn. *Appl. Phys. Lett.*, 91:131904, (2007).

[39] V. D. Buchelnikov and V. V. Sokolovskiy and S. V. Taskaev and V. V. Khovaylo and A. A. Aliev and L. N. Khanov and A. B. Batdalov and P. Entel and H. Miki and T. Takagi. Monte Carlo simulations of the magnetocaloric effect in magnetic Ni-Mn-X (X = Ga, In) Heusler alloys. *J. Phys. D: Appl. Phys.*, 44:064012, (2011).

[40] V. V. Khovaylo and K. P. Skokov and Y. S. Koshkid'ko and V. V. Koledov and V. G. Shavrov and V. D. Buchelnikov and S. V. Taskaev and H. Miki and T. Takagi and A. N. Vasiliev. Adiabatic temperature change at first-order magnetic phase transitions: Ni 2.19 Mn 0.81 Ga as a case study. *Phys. Rev. B*, 78:060403, (2008).

[41] S. Aksoy and T. Krenke and M. Acet and E. F. Wassermann and X. Moya and L. Manosa and A. Planes. Tailoring magnetic and magnetocaloric properties of martensitic transitions in ferromagnetic Heusler alloys. *Appl. Phys. Lett.*, 91:241916, (2007).

[42] V. V. Khovaylo and K. P. Skokov and O. Gutfleisch and H. Miki and T. Takagi and T. Kanomata and V. V. Koledov and V. G. Shavrov and G. Wang and E. Palacios and J. Bartolom'e and R. Burriel. Peculiarities of the magnetocaloric properties in Ni-Mn-Sn ferromagnetic shape memory alloys. *Phys. Rev. B*, 81:214406, (2010).

[43] A. P. Kazakov and V. N. Prudnikov and A. B. Granovsky and A. P. Zhukov and J. Gonzalez and I. Dubenko and A. K. Pathak and S. Stadler and N. Ali. Direct measurements of field-induced adiabatic temperature changes near compound phase transitions in Ni-Mn-In based Heusler alloys. *Appl. Phys. Lett.*, 98:131911, (2011).

[44] K. P. Skokov and V. V. Khovaylo and K.-H. Müller and J. D. Moore and J. Liu and O. Gutfleisch. Magnetocaloric materials with first-order phase transition: thermal and magnetic hysteresis in $LaFe_{11.8}Si_{1.2}$ and $Ni_{2.21}Mn_{0.77}Ga_{1.02}$. *J. Appl Phys.*, 111:07A910, (2012).

[45] S. Y. Yu and Z. X. Cao and L. Ma and G. D. Liu and J. L. Chen and G. H. Wu and B. Zhang and X. X. Zhang. Realization of magnetic field-induced reversible martensitic transformation in NiCoMnGa alloys. *Appl. Phys. Lett.*, 91:102507, (2007).

[46] S. Fabbrici and F. Albertini and A. Paoluzi and F. Bolzoni and R. Cabassi and M. Solzi and L. Righi and G. Calestani. Reverse magnetostructural transformation in Co-doped NiMnGa multifunctional alloys. *Appl. Phys. Lett.*, 95:022508, (2009).

[47] S. Fabbrici and J. Kamarad and Z. Arnold and F. Casoli and A. Paoluzi and F. Bolzoni and R. Cabassi and M. Solzi and G. Porcari and C. Pernechele and F. Albertini. From direct to inverse giant magnetocaloric effect in Co-doped NiMnGa multifunctional alloys. *Acta Mater.*, 59:412, (2011).

[48] F. Albertini and S. Fabbrici and A. Paoluzi and J. Kamarad and Z. Arnold and L. Righi and M. Solzi and G. Porcari and C. Pernechele and D. Serrate and P. Algarabel. Reverse Magnetostructural Transitions by Co and In Doping NiMnGa Alloys: Structural, Magnetic, and Magnetoelastic Properties. *Mater. Sci. Forum*, 684:151, 2011.

[49] F. Albertini and M. Solzi and A. Paoluzi and L. Righi. Magnetocaloric properties and magnetic anisotropy by tailoring phase transitions in NiMnGa alloys. *Mater. Sci. Forum*, 583:169, (2008).

[50] A. M. G. Carvalho and A. A. Coelho and P. J. von Ranke and C. S. Alves. The isothermal variation of the entropy (ΔS_T) may be miscalculated from magnetization isotherms in some cases: MnAs and $Gd_5Ge_2Si_2$ compounds as examples. *J. Alloy Compd.*, 509:3452, (2011).

[51] V. K. Pecharsky and K. A. Gschneidner Jr. Magnetocaloric effect from indirect measurements: Magnetization and heat capacity. *J. Appl. Phys.*, 86:565, (2000).

[52] N. A. de Oliveira and P. J. von Ranke. Magnetocaloric effect around a magnetic phase transition. *Phys. Rev. B*, 77:214439, (2008).

[53] J. S. Amaral and V. S. Amaral. On estimating the magnetocaloric effect from magnetization measurements. *J. Magn. Magn. Mater.*, 322:1552, (2010).

[54] W. Cui and W. Liu and Z. Zhang. The origin of large overestimation of the magnetic entropy changes calculated directly by Maxwell relation. *Appl. Phys. Lett.*, 96:222509, (2010).

[55] V. Basso and C. P. Sasso and K. P. Skokov and O. Gutfleisch and V. V. Khovaylo. Hysteresis and magnetocaloric effect at the magnetostructural phase transition of Ni-Mn-Ga and Ni-Mn-Co-Sn Heusler alloys. *Phys. Rev. B*, 85:014430, (2012).

[56] Felix Casanova and Xavier Batlle and Amilcar Labarta and Jordi Marcos and Lluis Manosa and Antoni Planes. Entropy change and magnetocaloric effect in $Gd_5(Si_xGe_{1-x})_4$. *Phys. Rev. B*, 66:100401(R), (2002).

[57] J. D. Moore and K. P. Skokov and J. Liu and O. Gutfleisch. Procedure for numerical integration of the magnetocaloric effect. *J. Appl. Phys.*, 112:063920, (2012).

[58] V. K. Pecharsky and K. A. Gschneidner, Jr. Heat capacity near first order phase transitions and the magnetocaloric effect: An analysis of the errors, and a case study of $Gd_5(Si_2Ge_2)$ and Dy. *J. Appl. Phys.*, 86:6315, (1999).

[59] S. Yu. Dan'kov and A. M. Tishin and V. K. Pecharsky and K. A. Gschneidner Jr. Experimental device for studying the magnetocaloric effect in pulse magnetic fields. *Rev. Sci. Instrum.*, 68:2432, (1997).

[60] B. R. Gopal and R. Chahine and T. K. Bose. A sample translatory type insert for automated magnetocaloric effect measurements. *Rev. Sci. Instrum.*, 68:1822, (1997).

[61] J. Kamarád and J. Kaštil and Z. Arnold. Practical system for the direct measurement of magneto-caloric effect by micro-thermocouples. *Rev. Sci. Instrum.*, 83:083902, (2012).

[62] S. Fujieda and Y. Hasegawa and A. Fujita and K. Fukamichi. Direct measurement of magnetocaloric effects in itinerant-electron metamagnets $La(Fe_xSi_{1-x})_{13}$ compounds and their hydrides. *J. Magn. Magn. Mater.*, 272:2365, (2004).

[63] S. M. Benford and V. G. Brown. T-S diagram for gadolinium near the Curie temperature. *J. Appl. Phys.*, 52:2110, (1981).

[64] X. Moya and L. Manosa and A. Planes and S. Aksoy and M. Acet and E. F. Wassermann and T. Krenke. Cooling and heating by adiabatic magnetization in the $Ni_{50}Mn_{34}In_{16}$ magnetic shape-memory alloy. *Phys. Rev. B*, 75:184412, (2007).

[65] F. Canepa and S. Cirafici and M. Napoletano and C. Ciccarelli and C. Belfortini. Direct measurement of the magnetocaloric effect of microstructured Gd eutectic compounds using a new fast automatic device. *Solid State Commun.*, 133:241, (2005).

[66] G. V. Brown. Magnetic heat pumping near room temperature. *J. Appl. Phys.*, 47:3673, (1976).

[67] B. R. Gopal and R. Chahine and M. Foldeaki and T. K. Bose. Noncontact thermoacoustic method to measure the magnetocaloric effect. *Rev. Sci. Instrum.*, 66:232, (1995).

[68] D. V. Christensen and R. Bjørk and K. K. Nielsen and C. R. H. Bahl and A. Smith and S. Clausen. Spatially resolved measurements of the magnetocaloric effect and the local magnetic field using thermography. *J. Appl. Phys.*, 108:063913, (2010).

[69] L. Mañosa and A. Planes and X. Moya. Comment on "The Magnetocaloric Effect of $LaFe_{11.6}Si_{1.4}$, $La_{0.8}Nd_{0.2}Fe_{11.5}Si_{1.5}$, and $Ni_{43}Mn_{46}Sn_{11}$ Compounds in the Vicinity of the First-Order Phase Transition". *Adv. Mater.*, 21:3725, (2009).

[70] T. Plackowski and Y. Wang and A. Junod. Specific heat and magnetocaloric effect measurements using commercial heat-flow sensors. *Rev. Sci. Instrum.*, 73:2755, (2002).

[71] J. Marcos and F. Casanova and X. Batlle and A. Labarta and A. Planes and L. Manosa. A high-sensitivity differential scanning calorimeter with magnetic field for magnetostructural transitions. *Rev. Sci. Instrum.*, 74:4768, (2003).

[72] A. A. Minakov and S. B. Roy and Y. V. Bugoslavsky and L. F. Cohen. Thin-film alternating current nanocalorimeter for low temperatures and high magnetic fields. *Rev. Sci. Instrum.*, 76:043906, (2005).

[73] S. Jeppesen and S. Linderoth and N. Pryds and L. Theil Kuhn and J. Buch Jensen. Indirect measurement of the magnetocaloric effect using a novel differential scanning calorimeter with magnetic field. *Rev. Sci. Instrum.*, 79:083901, (2008).

[74] V. Basso and C. P. Sasso and M. Kupferling. A Peltier cells differential calorimeter with kinetic correction for the measurement of $c_p(H,T)$ and $s(H,T)$ of magnetocaloric materials. *Rev. Sci. Instrum.*, 81:113904, (2010).

[75] V. Basso and M. Kupferling and C. P. Sasso and L. Giudici. A Peltier cell calorimeter for the direct measurement of the isothermal entropy change in magnetic materials. *Rev. Sci. Instrum.*, 79:063907, (2008).

[76] B. A. Assaf and T. Cardinal and P.Wei and F. Katmis and J. S. Moodera. Modified electrical transport probe design for standard magnetometer. *Rev. Sci. Instrum.*, 83:033904, (2012).

[77] http://www.lakeshore.com/Documents/LSTC Cernox l.pdf.

[78] B. L. Brandt and D. W. Liu and L. G. Rubin. Low temperature thermometry in high magnetic fields. VII. Cernox$^{\mathrm{TM}}$ sensors to 32 T. *Rev. Sci. Instrum.*, 70:104, (1999).

[79] M. D. Kuz'min and K. P. Skokov and D. Yu. Karpenkov and J. D. Moore and M. Richter and O. Gutfleisch. Magnetic field dependence of the maximum adiabatic temperature change. *Appl. Phys. Lett.*, 99:012501, (2011).

[80] V. Basso and C. P. Sasso and M. LoBue. Thermodynamic aspects of first-order phase transformations with hysteresis in magnetic materials. *J. Magn. Magn. Mater.*, 316:262, (2007).

[81] V. K. Pecharsky and K. A. Gschneidner Jr. Some common misconceptions concerning magnetic refrigerant materials. *J. Appl. Phys.*, 90:4614, (2001).

[82] V. V. Khovailo and V. Novosad and T. Takagi and D. A. Filippov and R. Z. Levitin and A. N. Vasil'ev. Magnetic properties and magnetostructural phase transitions in $Ni_{2+x}Mn_{1-x}$ Ga shape memory alloys. *Phys. Rev. B*, 70:174413, (2004).

[83] C. P. Sasso and M. Kupferling and L. Giudici and V. Basso and M. Pasquale. Direct measurements of the entropy change and its history dependence in Ni-Mn-Ga alloys. *J. Appl. Phys.*, 103:07B306, (2008).

[84] E. Cesari and V.A. Chernenko and J. Font and J. Muntasell. ac technique applied to cp measurements in Ni-Mn-Ga alloys. *Thermochim. Acta*, 433:153, (2005).

[85] V. K. Sharma and M. K. Chattopadhyay and R. Kumar and T. Ganguli and P. Tiwari and S. B. Roy. Magnetocaloric effect in Heusler alloys $Ni_{50}Mn_{34}In_{16}$ and $Ni_{50}Mn_{34}Sn_{16}$. *J. Phys. Cond. Matt.*, 19:496207, (2007).

[86] S. Das and J. S. Amaral and V. S. Amaral. Handling mixed-state magnetization data for magnetocaloric studies a solution to achieve realistic entropy behaviour. *J. Phys. D: Appl. Phys.*, 43:152002, (2010).

[87] K. Morrison and J. Lyubina and J. D. Moore and A. D. Caplin and K. G. Sandeman and O. Gutfleisch and L. F. Cohen. Contributions to the entropy change in melt-spun $LaFe_{11.6}Si_{1.4}$. *J. Phys. D: Appl. Phys.*, 43:132001, (2010).

[88] K. Morrison and M. Bratko and J. Turcaud and A. Berenov and A. D. Caplin and L. F. Cohen. A calorimetric method to detect a weak or distributed latent heat contribution at first order magnetic transitions. *Rev. Sci. Instrum.*, 83:033901, (2012).

[89] K. Morrison and K. G. Sandeman and L. F. Cohen and C. P. Sasso and V. Basso and A. Barcza and M. Katter and J. D. Moore and K. P. Skokov and O. Gutfleisch. Evaluation of the reliability of the measurement of key magnetocaloric properties: A round robin study of La(Fe,Si,Mn)H_δ conducted by the SSEEC consortium of European laboratories. *Int. J. Refrig.*, 35:1528, (2012).

[90] Ö. Çakır and M. Acet,. Reversibility in the inverse magnetocaloric effect in Mn_3GaC studied by direct adiabatic temperature-change measurements. *Appl. Phys. Lett.*, 100:202404, (2012).

[91] I. Titov and M. Acet and M. Farle and D. Gonzalez-Alonso and L. Manosa and A. Planes and T. Krenke. Hysteresis effects in the inverse magnetocaloric effect in martensitic Ni-Mn-In and Ni-Mn-Sn. *J. Appl. Phys.*, 112:073914, (2012).

[92] J. Lyubina. Recent advances in the microstructure design of materials for near room temperature magnetic cooling (invited). *J. Appl. Phys.*, 109:07A902, (2011).

[93] R. A. Booth and S. A. Majetich. The magnetocaloric effect in thermally cycled polycrystalline Ni-Mn-Ga. *J. Appl. Phys.*, 111:07A933, (2012).

[94] J. Lyubina and U. Hannemann and M. P. Ryan and L. F. Cohen. Electrolytic Hydriding of $LaFe_{13-x}Si_x$ Alloys for Energy Efficient Magnetic Cooling. *Adv. Mater.*, 24:2042, (2012).

[95] A. Kitanovski and P. Egolf. Innovative ideas for future research on magnetocaloric technologies. *Int. J. Refrig.*, 33:449, (2010).

[96] M. D. Kuz'min. Factors limiting the operation frequency of magnetic refrigerators. *Appl. Phys. Lett.*, 90:251916, (2007).

[97] http://www.omega.com/Heaters/pdf/KHR_KHLV_KH.pdf.

[98] A. Kitanovski and P. Egolf and A. Poredos. Rotary magnetic chillers with permanent magnets. *Int. J. Refrig.*, 35:1055, (2012).

[99] K. G. Sandeman. Magnetocaloric materials: The search for new systems. *Scr. Mater.*, 67:566, (2012).

[100] K. Morrison and J. Lyubina and J. D. Moore and K. G. Sandeman and O. Gutfleisch and L.F. Cohen and A. D. Caplin. Magnetic refrigeration: phase transitions, itinerant magnetism and spin fluctuations. *Philos. Mag.*, 92:292, (2012).